Summer 7-31-2023

STUDY OF RADIATION EFFECTS IN GAN-BASED DEVICES

Han Gao
gaoh@smu.edu

Recommended Citation
Gao, Han, "STUDY OF RADIATION EFFECTS IN GAN-BASED DEVICES" (2023). *Electrical Engineering Theses and Dissertations*. 64.
https://scholar.smu.edu/engineering_electrical_etds/64

STUDY OF RADIATION EFFECTS IN GAN-BASED DEVICES

Approved by:

Dr. Ronald Rohrer
Electrical and Computer Engineering
Southern Methodist University
Dissertation Committee Chairperson

Dr. Bruce Gnade
Electrical and Computer Engineering
University of Texas at Dallas

Dr. Robert Baumann
Electrical and Computer Engineering
University of Texas at Dallas

Dr. Theodore Moise
Electrical and Computer Engineering
University of Texas at Dallas

Dr. Prasanna Rangarajan
Electrical and Computer Engineering
Southern Methodist University

Dr. Kevin Brenner
Electrical and Computer Engineering
Southern Methodist University

Dr. Dinesh Rajan
Electrical and Computer Engineering
Southern Methodist University

STUDY OF RADIATION EFFECTS IN GAN-BASED DEVICES

A Dissertation Presented to the Graduate Faculty of the

Lyle School of Engineering

Southern Methodist University

in

Partial Fulfillment of the Requirements

for the degree of

Doctor of Philosophy

with a

Major in Electrical Engineering

by

Han Gao

M.S., Electrical Engineering, Southern Methodist University
B.S., Electrical Engineering, South China University of Technology

July 31, 2023

Gao, Han M.S., Electrical Engineering, Southern Methodist University, 2018
B.S., Electrical Engineering, South China University of Technology, 2016

Study of Radiation Effects in GaN-based Devices

Advisor: Dr. Bruce Gnade and Dr. Robert Baumann

Doctor of Philosophy conferred July 31, 2023

Dissertation completed July 31, 2023

Radiation tolerance of wide-bandgap Gallium Nitride (GaN) high-electron-mobility transistors (HEMT) has been studied, including X-ray-induced TID effects, heavy-ion-induced single event effects, and neutron-induced single event effects. Threshold voltage shift is observed in X-ray irradiation experiments, which recovers over time, indicating no permanent damage formed inside the device. Heavy-ion radiation effects in GaN HEMTs have been studied as a function of bias voltage, ion LET, radiation flux, and total fluence. A statistically significant amount of heavy-ion-induced gate dielectric degradation was observed, which consisted of hard breakdown and soft breakdown. Specific critical injection level experiments were designed and carried out to explore the gate dielectric degradation mechanism further. Transient device simulations determined ion-induced peak transient electric field and duration for a variety of ion LET, ion injection locations, and applied drain voltages. Results demonstrate that the peak transient electric fields exceed the breakdown strength of the gate dielectric, leading to dielectric defect generation and breakdown.

GaN power device lifetime degradation caused by neutron irradiation is reported. Hundreds of devices were stressed in the off-state with various drain voltages from 75 V to 400 V while irradiated with a high intensity neutron beam. Observing a statistically significant number of neutron-induced destructive single-event-effects (DSEEs) enabled an accurate extrapolation of terrestrial field failure rates. Nuclear event and electronic simulations were performed to model the effect of terrestrial neutron secondary ion-induced gate dielectric breakdown. Combined with the TCAD simulation results, we believe that heavy-ion-induced

SEGR and neutron-induced SEGR share common physics mechanisms behind the failures. Overall, experimental data and simulation results provide evidence supporting the idea that both radiation-induced SBD and HBD are associated with defect-related conduction paths formed across the dielectric, in response to radiation-induced charge injection. A percolation theory-based dielectric degradation model is proposed, which explains the dielectric breakdown behaviors observed in heavy-ion irradiation experiments.

TABLE OF CONTENTS

CHAPTER

LIST OF FIGURES

Figure Page

LIST OF TABLES

Table Page

ACKNOWLEDGMENTS

First, I would like to express my deepest appreciation to my advisors, Dr. Bruce Gnade and Dr. Robert Baumann for their valuable advice and profound belief in my work. During my Ph.D. study, Dr. Gnade and Dr. Baumann have been giving me unwavering support and guidance with patience that cannot be underestimated. Their rigorous scientific attitudes and enthusiasm for research have helped me overcome many difficulties along this journey and will continue to illuminate my direction in the future.

I would like to extend my sincere thank to Dr. Ronald Rohrer, Dr. Theodore Moise, and Dr. Kevin Brenner, who offered me constructive advice and unparalleled support in my research journey. I am also grateful to the rest of my doctoral committee: Dr. Dinesh Rajan and Dr. Prasanna Rangarajan. I would like to thank them for their helpful advice and insightful discussions to enhance the quality of my dissertation greatly. More importantly, my doctoral committee members have shown me how extraordinary researchers think and solve problems.

I cannot leave SMU without mentioning Dr. Tao Zheng, who has constantly provided practical contributions and ingenious discussions. I also had the great pleasure of working with my colleagues, Reza Farsad Asadi, Rohin Thampilali Narayan, and Danyal Ahsanullah, who have provided relentless help in different ways. I am extremely grateful to my colleague and my girlfriend Menglin Wang, who always supported and encouraged me.

Above all, I'm deeply indebted to my parents. Their belief in me has kept my spirits and motivation high during this process.

Chapter 1

Introduction

1.1 Power Semiconductor Devices

Today the semiconductor business exceeds $500 B with about 10% of the revenue derived from power semiconductor devices and smart power integrated circuits [1]. As the crucial components of all power electronic systems, power semiconductor devices have been widely used in various applications including consumer, medical, industrial, and transportation [1]. Power devices enable the efficient processing of electrical energy, including the whole generation-storage-distribution cycle [2]. According to some estimates, at least 50% of the electricity consumed worldwide is controlled by power devices and more than 60% of all the electricity utilized in the United States flows through one or multiple power devices [1], [3]. Thus, the performance of power devices significantly impacts the economy, as they determine the cost, size, and efficiency of the power systems. Since the 1950s, power semiconductor devices started to replace vacuum tubes and have become the dominant technology in power devices, which has been known as the second electronic revolution [1].

One common way to classify applications of power semiconductor devices is in terms of system power rating and operating frequency [1]. Typically system power rating is inversely proportional to system operating frequency. For example, high-power systems like high-voltage power distribution and electric trains require the control of megawatts of power, while operating at relatively low frequencies (below 1000 Hz) [1]. On the contrary, applications like cellular communication and microwave oven usually require ultra-high operation frequencies (above 10^8 Hz) and relatively low power ratings. Notice that, electric cars, which have become one of the most attractive applications of power semiconductor devices, need medium power ratings and operating frequencies. Overall, there is currently no single power semiconductor device type that fits all applications.

Further, power semiconductor devices can be divided into two different types:

1. Bipolar power devices, whose operations are involved with both majority and minority carriers during on-state current flow. When switching the device from on-state to off-state, minority carriers will be removed by either electron-hole pair recombination or gate drive current, which introduces significant power loss and reduced power management efficiency [1]. The commonly used bipolar power devices are PN-junction-based devices like the thyristor and insulated gate bipolar transistor (IGBT).

2. Unipolar power devices' on-state current flow only involves majority carriers. The commonly used unipolar power devices are field effect transistors including the metal oxide semiconductor field effect transistor (MOSFET), junction field effect transistor (JFET), and high electron mobility transistor (HEMT).

1.2 Wide Bandgap Power Semiconductor Devices

Silicon is the dominant base material for current power semiconductor devices. Both unipolar and bipolar power devices have been successfully developed from silicon to serve a very broad range of applications [1]. However, with the rapid development of power systems, Si technology has exhibited several crucial limitations regarding blocking voltage capability, operation temperature, and switching frequency [2]. As mentioned in [2], the maximum operating voltage of a Si IGBT is around 6.5 kV, with a limited switching performance and the maximum operating temperature for Si-based power devices is $\leq$ 200 °C. Therefore, wide bandgap material-based power semiconductor devices have become more and more attractive because of their ability to operate at high voltages, high temperatures, and high switching frequencies, while providing very low on-resistance, and enabling more efficient power conversion [4].

Currently, the most widely used wide bandgap materials are silicon carbide (SiC) and gallium nitride (GaN), which exhibit the best trade-off among blocking voltage, operating temperature, switching frequency, and commercial availability [2]. The fundamental properties of silicon, silicon carbide, and gallium nitride are summarized and compared in Table 1.1 [5]. It is worth noting that the band gap energies of GaN and SiC are almost

Table 1.1: Material properties of Si, GaN and 4H-SiC [5].

Parameters	Silicon	GaN	4H-SiC
Bandgap	1.12 eV	3.39 eV	3.26 eV
Critical Field E_{crit}	0.23 MV/cm	3.3 MV/cm	2.2 MV/cm
Electron Mobility μ_n	1400 cm^2/V·s	1500 cm^2/V·s	950 cm^2/V·s
Relative Permittivity ϵ_r	11.8	9	9.7
Thermal Conductivity	1.5 W/cm·K	1.3 W/cm·K	3.8 W/cm·K

3 times larger than silicon, which results in a much lower intrinsic carrier concentration at any given temperature, as well as much smaller impact ionization coefficients at any given electric field [1].

To have a better understanding of material properties' effect on power devices' performance, we will describe the three most important characteristics [5]:

1. Bandgap, which is closely related to the chemical bond strength between the atoms inside the material lattice. The stronger chemical bonds in the wider-bandgap materials make it harder for electrons to jump from site to site, leading to lower intrinsic leakage currents and operation at higher temperatures.

2. Critical field, which is the minimum electric field strength to initiate impact ionization. Impact ionization refers to the generation of electron-hole pairs (ehps) due to energy acquired from the external electric field inside semiconductor materials, which is the main cause of avalanche breakdown. The breakdown voltage V_{BD} can be expressed by the following equation [5]:

$$V_{BD} = \frac{w_{drift} \cdot E_{crit}}{2} \tag{1.1}$$

where w_{drift} is the drift region width. The drift region is a thick epitaxial layer with a relatively low doping concentration N_{dope} (either N type or P type) to support higher operation voltages for power devices. The carriers in the drift region will be depleted away when the electric field reaches E_{crit}. N_{dope} can be calculated using Poisson's equation [5]:

$$q \cdot N_{dope} = \frac{\epsilon_0 \cdot \epsilon_r \cdot E_{crit}}{w_{drift}} \tag{1.2}$$

where q is the electron charge (1.6×10^{-19} C), ϵ_0 is the vacuum permittivity and ϵ_r is the relative permittivity of the material. Based on equation (1.1), in the case of GaN and SiC, the drift region can be 10 times smaller than silicon for the same breakdown voltage, which has a significant influence on the overall device size. Further, referring to equation (1.2), N_{dope} for both GaN and SiC can be 100 times greater than that in silicon (w_{drift} is 10 times smaller). Together, the number of carriers N_{dope} in the drift region can be 100 times greater but have one-tenth the distance to travel (much shorter drift region), which is the basis for the outstanding performance of GaN and SiC-based power devices in power conversion compared with Si-based devices.

3. On resistance (R_{on}), which can be calculated theoretically using the following equation (unipolar power devices) [5]:

$$R_{on} = \frac{w_{drift}}{q \cdot \mu_{carrier} \cdot N_{dope}} \tag{1.3}$$

where $\mu_{carrier}$ is the majority carrier mobility. Combining equations (1.1), (1.2), and (1.3) together, we get the following relationship between V_{BD} and R_{on} [5]:

$$R_{on} = \frac{4 \cdot V_{BD}^2}{\mu_{carrier} \cdot \epsilon_0 \cdot \epsilon_r \cdot E_{crit}^3} \tag{1.4}$$

This equation can be plotted as shown in Fig. 1.1, assuming an N-type semiconductor. Notice that Fig. 1.1 shows the theoretical material limit with ideal device structures, while in reality, there are many difficulties that need to be overcome.

1.3 Gallium Nitride High Electron Mobility Transistors

As discussed in the last section, the two primary wide-bandgap materials that have recently been widely commercialized are silicon-carbide (SiC) and gallium-nitride (GaN). SiC

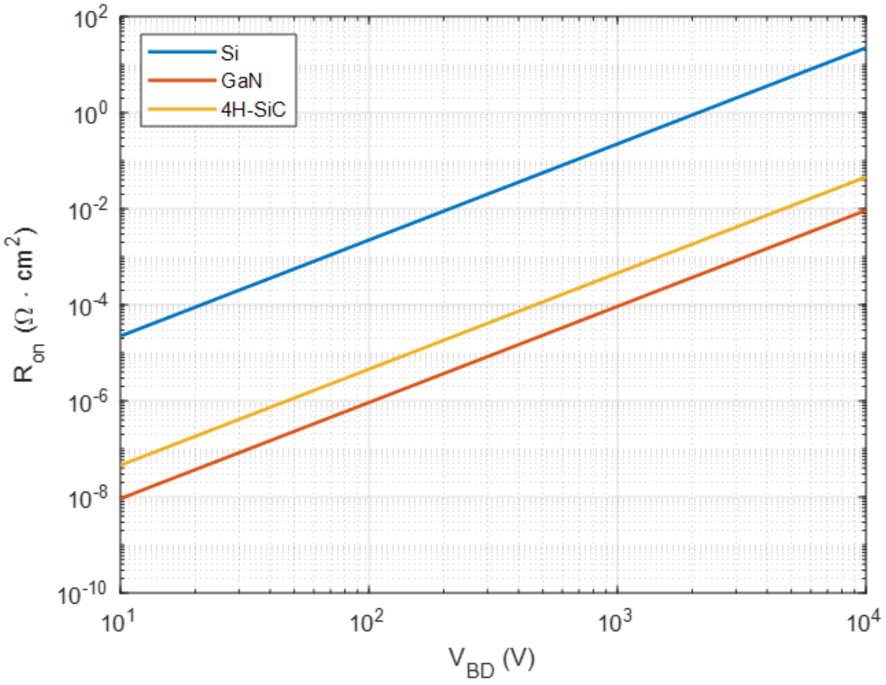

Figure 1.1: Theoretical on-resistance (R_{on}) vs. breakdown voltage (V_{BD}) for Si, GaN, and SiC-based power devices. Compared with Si, SiC and GaN are ideal base materials for high-voltage power devices. Note that, this plot is for an ideal structure.

can typically sustain higher operating voltages than GaN, but GaN has lower power consumption, lower switching loss, and higher electron mobility [5]. Among the wide-bandgap power devices, AlGaN/GaN high electron mobility transistors (HEMTs) have the potential to provide high reliability in harsh environments thanks to their outstanding robustness and efficiency [6]. In this project, radiation effects on GaN high electron mobility transistors (HEMT), including enhancement mode (E-mode) and depletion mode (D-mode) are the main research topic. In this section, a short review of the GaN HEMT working principle will be given.

Just like all the other HEMTs, a GaN HEMT relies on a two-dimensional electron gas (2DEG). Piezoelectricity in GaN is predominantly caused by the displacement of charged elements in the crystal lattice [5]. The tensile strain caused by the growth of AlGaN on GaN results in a piezoelectric polarization that forms the 2DEG channel at the interface between

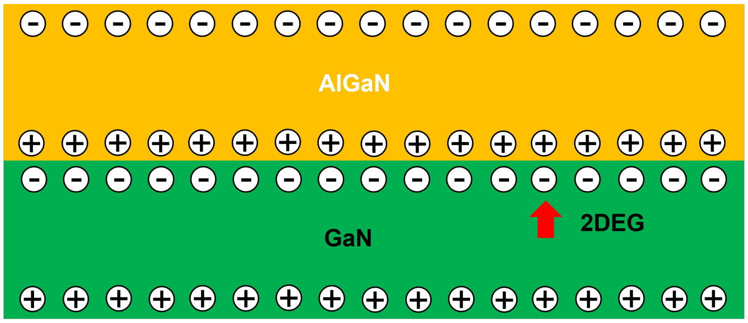

Figure 1.2: Simplified cross section of a GaN/AlGaN heterojunction. The formation of a 2DEG due to the strain-induced polarization (piezoelectric effect) is shown.

two layers [4]. Fig. 1.2 shows an illustration of the 2DEG formed at the AlGaN/GaN interface, which can efficiently conduct electrons horizontally with an electric field applied. The superior conductivity of the 2DEG is partially due to the electrons being confined to a thin layer at the interface. This confinement reduces surface scattering, which increases the electron mobility in the 2DEG from 1000 $\mathrm{cm}^2/\mathrm{V}\cdot\mathrm{s}$ in unstrained GaN to 1500-2000 $\mathrm{cm}^2/\mathrm{V}\cdot\mathrm{s}$ in the 2DEG [5], which leads to the superior performance of GaN HEMTs.

The basic depletion-mode GaN HEMT structures are shown in Fig. 1.3 and Fig. 1.4. Drain and source metal contacts penetrate the AlGaN layer and form Ohmic contacts with the 2DEG. Depletion mode refers to the fact that electrons in the 2DEG can only be depleted away by applying a negative gate voltage relative to both drain and source voltages.

However, D-mode devices are inconvenient for power conversion applications, as a negative gate bias must be applied to keep devices under the off-state [5]. Without a negative bias, a short circuit will form and result in catastrophic damage. Thus, an enhancement-mode device is more attractive, which requires a positive gate bias to turn on the 2DEG channel. Four E-mode GaN HEMT structures have been proposed and are widely discussed in the literature, which are recessed gate structure, implanted gate structure, pGaN gate structure, and cascode hybrid structure [5].

1. The recessed gate E-mode structure is created by decreasing the AlGaN layer thickness as shown in Fig. 1.5 [5]. By thinning the AlGaN layer, the built-in potential V_{piezo}

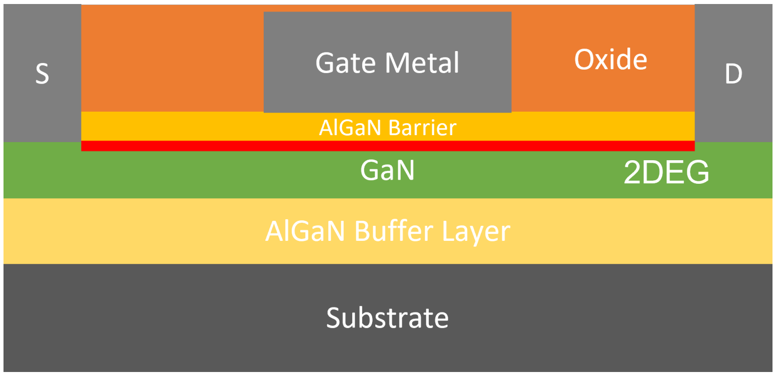

Figure 1.3: Basic structure of a D-Mode GaN HEMT with Schottky gate. The red line marks the 2DEG along the AlGaN/GaN interface. The schematic of the cross-section is simplified.

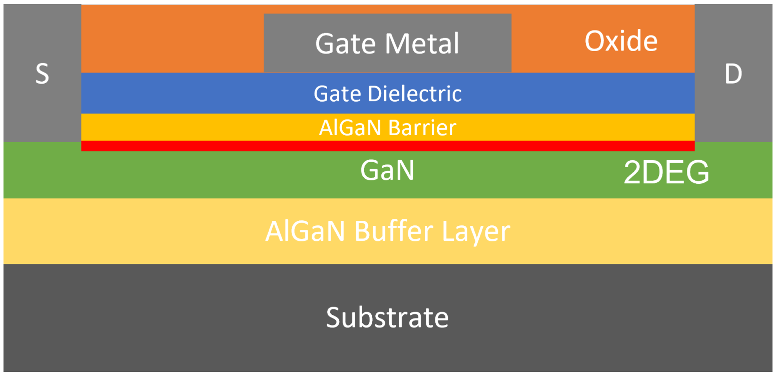

Figure 1.4: Basic structure of the D-Mode GaN HEMT with a gate dielectric. The red line marks the 2DEG along the AlGaN/GaN interface. The schematic of the cross-section is simplified.

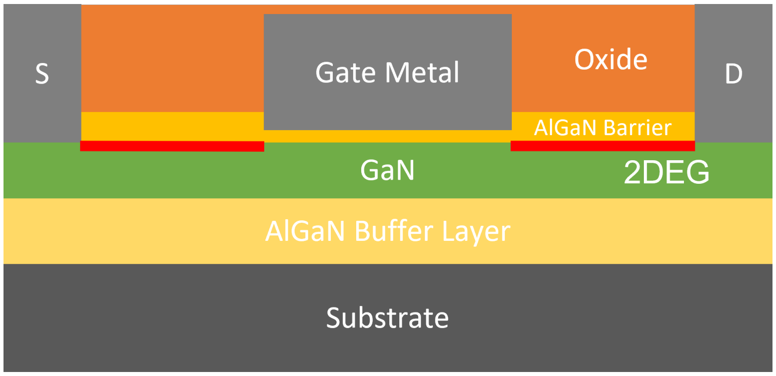

Figure 1.5: Recessed gate E-mode GaN HEMT structure with a Schottky gate contact, which can be fabricated by etching away part of the AlGaN layer under the gate. The red line marks the 2DEG along the AlGaN/GaN interface, which has been partially depleted. The schematic of the cross-section is simplified.

generated by the piezoelectric effect is reduced proportionally [5]. When V_{piezo} is less than the built-in potential of the Schottky gate, the 2DEG will be depleted with no gate bias [5].

2. The implanted gate E-mode structure is created by implanting fluorine atoms inside the AlGaN layer as shown in Fig. 1.6 [5]. Implanted fluorine atoms act as trapped negative charges in the AlGaN layer, which is able to deplete the underneath 2DEG channel.

3. The pGaN gate E-mode structure is created by depositing a layer of p-type GaN (positively charged) between the gate metal and the AlGaN layer as shown in Fig. 1.7 [5]. The p-type GaN layer forms a pn junction with the AlGaN and GaN layers beneath it [7]. The depletion region of the pn junction extends over the 2DEG channel with a proper p-type doping level, which leads to a partially depleted 2DEG channel under zero gate bias [7].

4. Cascode hybrid E-mode structure is an alternative way to build a single-chip E-mode GaN HEMT [5]. An E-mode silicon MOSFET is connected in series with a D-mode GaN HEMT as shown in Fig. 1.8 [5]. Without a positive gate bias, current is unable to flow between the drain and source contacts.

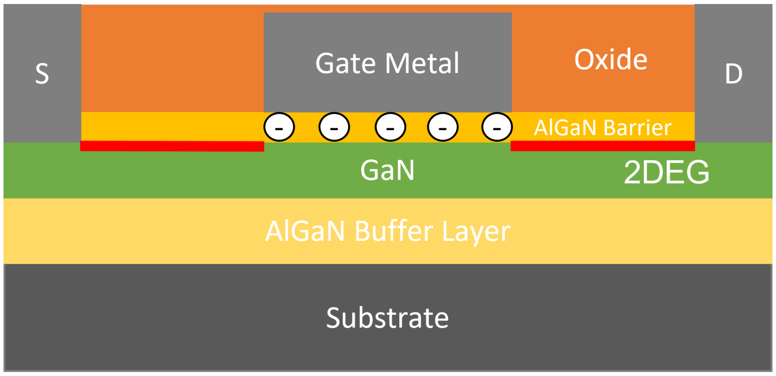

Figure 1.6: Implanted gate E-mode GaN HEMT structure with a Schottky gate contact. The white circles inside the AlGaN layer represent the implanted fluorine atoms. The red line marks the 2DEG along the AlGaN/GaN interface, which has been partially depleted. The schematic of the cross-section is simplified.

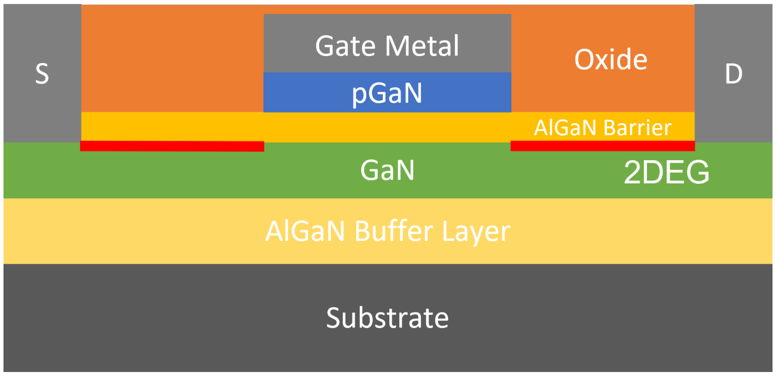

Figure 1.7: pGaN gate E-mode GaN HEMT structure with a Schottky gate contact. The formed pn junction will partially deplete the 2DEG channel. The red line marks the 2DEG along the AlGaN/GaN interface. The schematic of the cross-section is simplified.

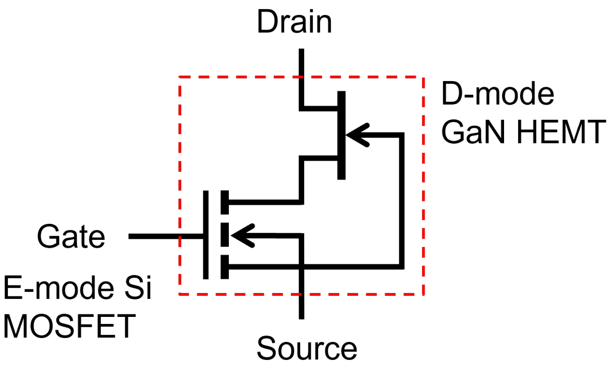

Figure 1.8: Cascode hybrid E-mode structure, which consists of a D-mode GaN HEMT and an E-mode Si MOSFET. Red dashed rectangle marks the single-chip cascode hybrid E-mode GaN HEMT.

1.4 Space and Terrestrial Radiation Environments

In this section, a brief overview of the space and terrestrial radiation environments will be presented. More detailed information on the radiation environments can be found in [8–11].

The space radiation environment consists of various sources of radiation, which can be categorized into three parts: [12]

1. Solar particle events (SPE) refer to high flux, high energy particles from solar events. The levels of SPEs are modulated by the 11-year solar cycle [12]. SPEs include high-energy protons, electrons, alpha particles, and other heavy ions. A typical SPE usually lasts hours to days [13].

2. Galactic cosmic rays (GCR) are low flux, continuously present, and slowly varying ultra high energy transient particles of all the elements [12]. Hydrogen and alpha particles are the main particle types [13]. Solar activities also have a significant effect on galactic cosmic rays.

3. Van Allen belts are belt-like structures consisting of particles trapped by the earth's magnetic field. Protons and electrons from solar events and galactic cosmic ray interactions are the main particle types. The trapped particle levels and locations are closely related to particle energy, altitude, inclination, and the activity level of the sun and are highly dynamic [12]. Fig. 1.9 shows a cutaway model of the Van Ellen belt with different satellite orbits [14]. For protons with energy above 30 MeV, the flux peaks at approximately 2500 km altitude [12]. Electrons are trapped in two regions, the inner belt, and the outer belt. For electrons with energy above 2 MeV, the flux peaks at approximately 2500 km altitude for the inner belt and 20000 km altitude for the outer belt [12].

Table 1.2 shows the maximum energy of different particles in the space radiation environment [12]. These high-energy particles can easily penetrate shielding material and introduce destructive effects in semiconductor devices.

When cosmic rays and solar particles enter the earth's atmosphere, they interact with the nuclei of atoms in the upper atmosphere, which will create a cascade of secondary particles

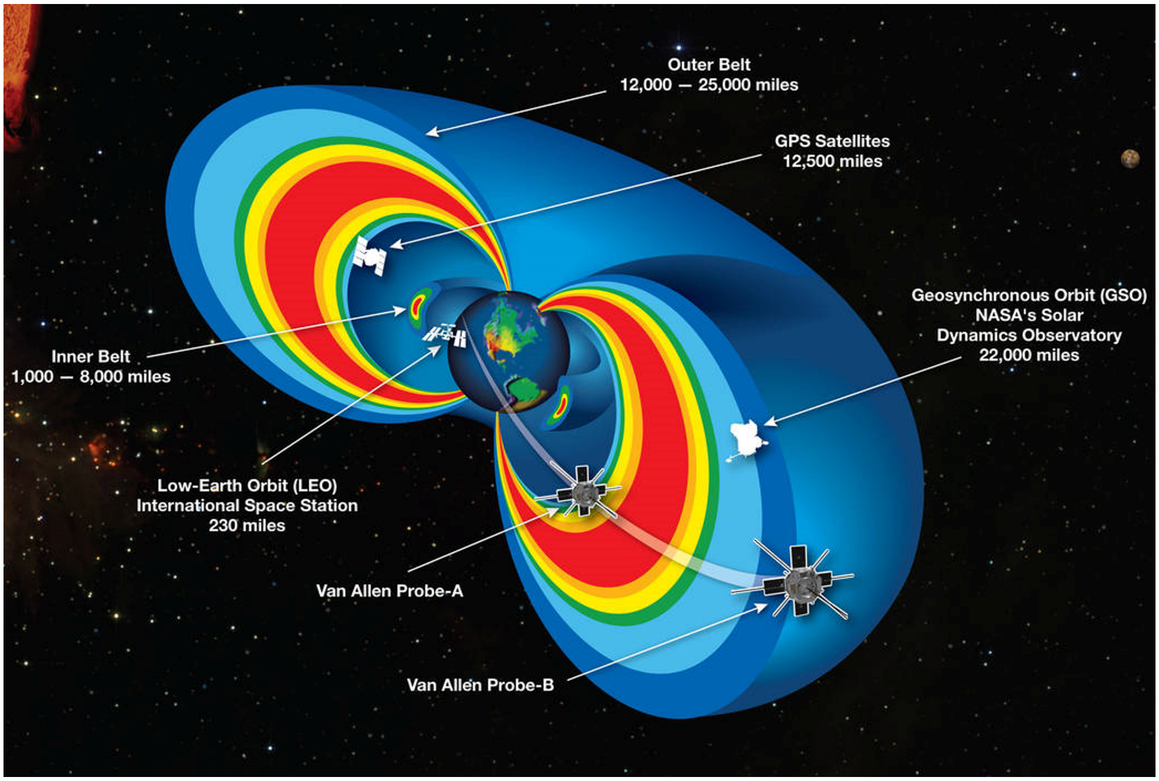

Figure 1.9: A cutaway model of the Van Ellen belt with different satellite orbits. Low-earth orbit (LEO) is below 2000 km and geosynchronous equatorial orbit (GEO) is at 35870 km. Picture from NASA open access database [14].

Table 1.2: Maximum Energy of Particles in Space Environment [12].

Particle Type	Maximum Energy
Van Ellen Belt Trapped Electron	10 MeV
Van Ellen Belt Trapped Proton	100 MeV
SPE Proton	GeV
SPE Heavy Ion	GeV
GCR Particle	TeV

as shown in Fig. 1.10. These secondary particles consist of photons, muons, pions, electrons, protons, neutrons, and heavy ions, which form the terrestrial radiation environment (terrestrial cosmic rays) [12]. Most secondary particles have very short lifetimes or lose energy rapidly before reaching the earth [9]. Terrestrial cosmic rays reach their peak density at about 10 to 25 km altitude, which covers the cruising altitudes of most commercial airplane flights [9]. The neutron is the most important secondary particle in terms of radiation effects on semiconductor devices in the atmosphere [12]. There is a general agreement that more than 95% of terrestrial cosmic rays at sea level are neutrons [9]. The energy spectrum of terrestrial neutrons is shown in Fig. 1.11. Blue dots are the actual data points measured in New York City outdoors with mid-level solar activity, which has been used as a reference neutron spectrum [15]. The red solid line is the analytic model which has been fit to the reference spectrum data points, which is given by the following equation [15]:

$$\frac{d\dot{\Phi}_0(E)}{dE} = 1.006 \times 10^{-6} \cdot e^{-0.35(ln(E))^2 + 2.1451 ln(E)} + 1.011 \times 10^{-3} \cdot e^{-0.4106(ln(E))^2 - 0.667 ln(E)} \quad (1.5)$$

where $\frac{d\dot{\Phi}_0(E)}{dE}$ is the differential neutron flux and E is the neutron energy. Overall, for neutron energy above 10 MeV the total flux of the measured reference spectrum is 12.9 $cm^{-2}h^{-1}$ (equivalent 13 $cm^{-2}h^{-1}$) [15]. A detailed reference neutron spectrum is presented in [15]. It has been experimentally validated that terrestrial neutrons can induce destructive effects in various power semiconductor devices like high-voltage diodes, thyristors, power MOSFETs and insulated-gate bipolar transistors (IGBTs) [16–18], and limit their reliable performance in terrestrial power applications. Therefore, understanding the dominant mechanisms of radiation effects on semiconductor devices is a key factor for improving system reliability at higher bias voltages in aerospace and other high reliability applications.

1.5 Radiation-Induced Failures in Semiconductor Devices

1.5.1 Radiation Interactions with Semiconductor Materials

Radiation has a significant impact on semiconductor device performance. Energetic particles interact with semiconductor materials in the following ways, which will introduce different radiation effects.

1. Direct ionizing processes refer to the phenomena where charged particles like electrons, alpha particles, and heavy ions interact with the orbital electrons of the traversed material, generating a high density of electron-hole pairs (ehp) along their tracks. Each energetic particle interacts with a large volume of atoms and generates a fairly high density of electron-hole pairs. The ehps along the particle injection track may form a conductive funnel-like plasma filament, as shown in Fig. 1.12.

2. Indirect ionizing processes are induced by elastic or inelastic interactions. Elastic interactions refer to the interaction between atoms in which the total energy of the system is conserved, without kinetic energy loss. When the energy transferred from the incoming particle is above the binding energy of the target material, a charged recoiling nucleus will be generated during elastic interactions, which itself will induce ionization and create electron-hole pairs through the same physical process. Inelastic interactions refer to a scattering process in which the kinetic energy of the incident particle is not conserved. Typically, the incident particle is absorbed by the target nucleus and results in the direct liberation of charged secondary particles through processes including fission, spallation reactions, and chemical reactions.

3. A non-ionizing process consists of impurity production and atom displacement. Impurity production is related to nuclear interactions, which have a significant effect on the electrical and optical properties of the semiconductor material. Atom displacement refers to the process that an incoming particle collides with the semiconductor mate-

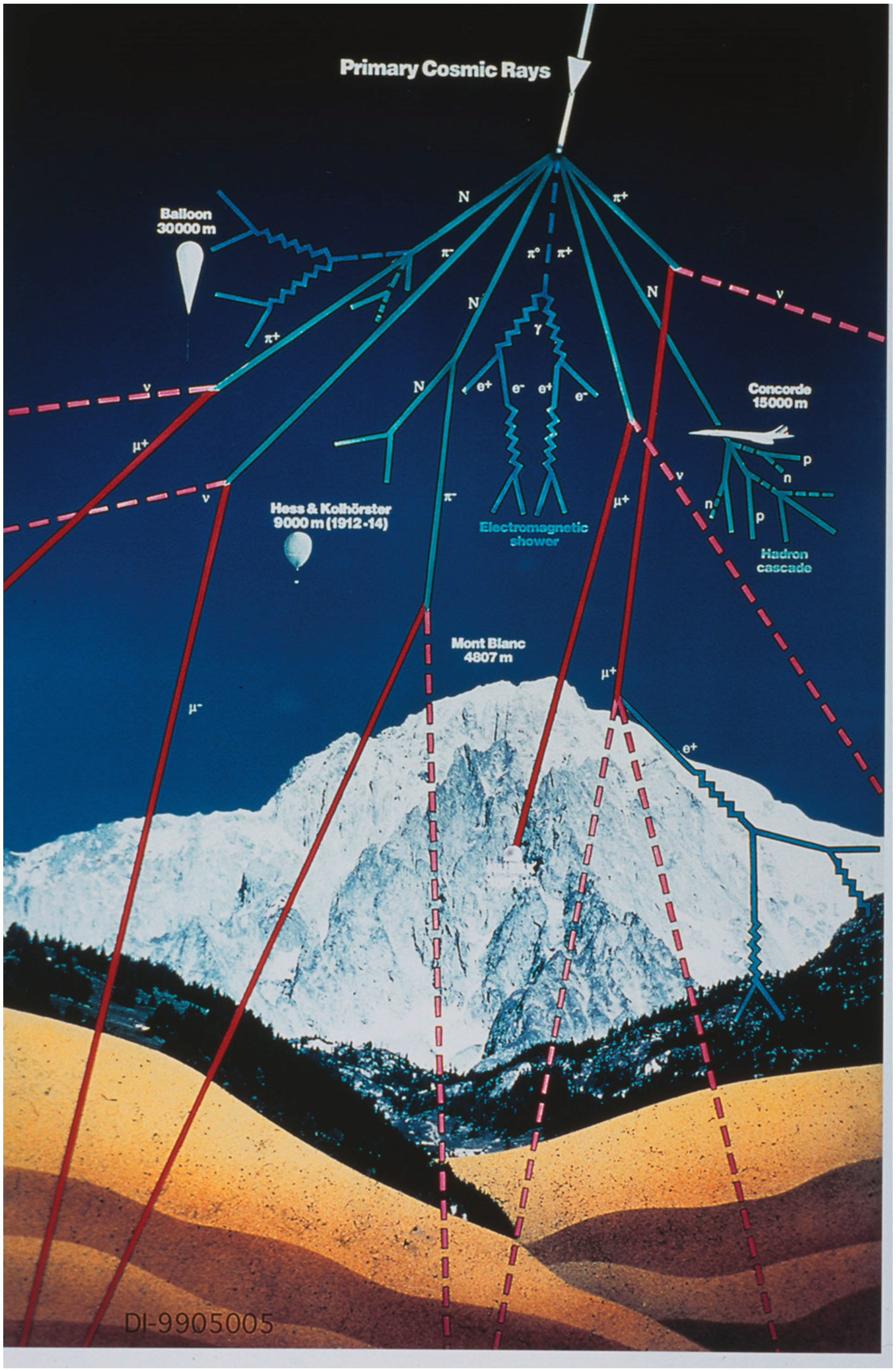

Figure 1.10: Primary cosmic rays enter the top of the atmosphere and create a shower of secondary particles, including protons, neutrons, muons, etc. Most secondary particles have very short lifetimes, which will decay spontaneously or lose energy and reach thermal energy before reaching earth [9]. Picture from CERN open access database [19].

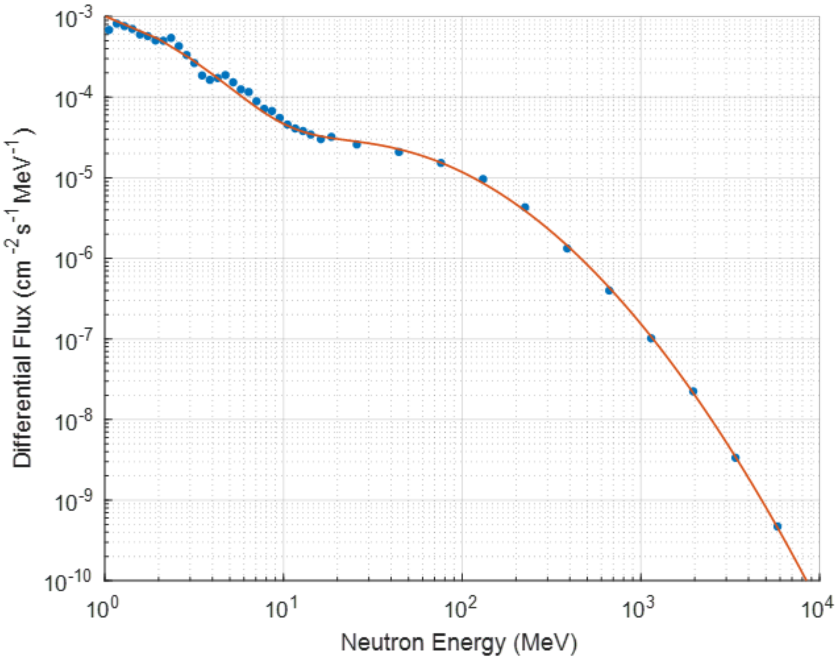

Figure 1.11: Cosmic-ray-induced neutron differential flux vs. neutron energy at New York City outdoors (sea level) with mid-level solar activity. Blue dots are the reference neutron spectrum determined by actual measurements [15]. The red solid line is an analytic model fit to the reference spectrum [15].

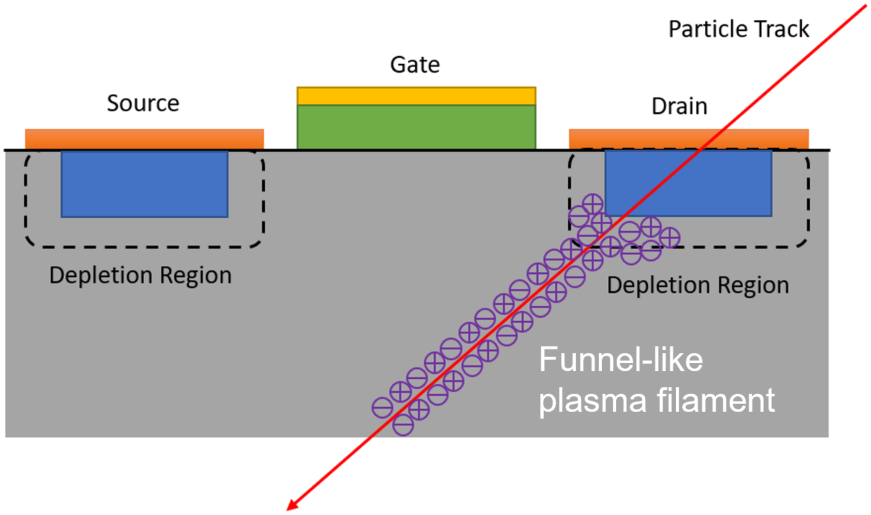

Figure 1.12: An example of a direct ionizing process in a MOSFET structure. The red arrow represents the incident particle injection track. Electron-hole pairs generated along the injection track form a funnel-like plasma filament.

rial atom, causing the atom to be knocked out of its original position. Displacement atoms may leave lattice vacancies and stay in interstitial positions, which will impact the electrical and mechanical properties of the semiconductor material.

Energetic particle interactions with the material can be separated into electronic and nuclear stopping powers, as shown in the following equation [20]:

$$\frac{dE}{dx}|_{total} = \frac{dE}{dx}|_{elec} + \frac{dE}{dx}|_{nucl} \tag{1.6}$$

where electronic stopping power represents the mean energy loss per unit length due to interactions with target electrons and is given by equation (1.7) [20]:

$$\begin{aligned} -\frac{dE}{dx}|_{elec} &= NZS_e \\ &= \frac{1}{4\pi\epsilon_0}\frac{Z_1^2 e^4}{m_e v^2} N Z_2 L_e \\ &= 3.705 \times 10^{-4} \frac{Z_1^2 Z_2}{A_2 \beta} L_e \end{aligned} \tag{1.7}$$

where Z_1 and Z_2 are the atomic numbers of the injected particle and the traversed material. A_2 is the mass number of the material atoms. N is the atomic density of the target material. v is the velocity of the injected particle. S_e is the electronic stopping cross-section (energy× area) [20]. e is the electron charge and m_e is the electron rest mass [20]. ϵ_0 is the vacuum permittivity. L_e is the theory dependent dimensionless stopping number for electronic stopping [20]. β equals v/c, where c is the speed of light in vacuum. The unit of electronic stopping power is MeV·cm^2/mg [20]. Electronic stopping power represents the average energy loss of the energetic ionizing particle per unit distance in the target material. Linear energy transfer (LET) is the metric for the average ionizing energy deposited per unit length by the injected particle, which in most cases has no difference with electronic stopping power by definition [20]. Note that, heavy-ion radiations are typically characterized in terms of the corresponding LET [20].

$$LET = \frac{dE}{dx}|_{elec} \tag{1.8}$$

The effective energy deposited by injected ions within the target material also depends on the injection angle [20]. Thus, the effective LET for angled strikes is given by the following equation [20].

$$LET_{eff} = \frac{LET_0}{cos(\theta)} \tag{1.9}$$

Similar to the electronic stopping power, the nuclear stopping power is defined by equation (1.10) [20].

$$-\frac{dE}{dx}|_{nucl} = \frac{1}{4\pi\epsilon_0}\frac{Z_1^2 e^4}{M_2 v^2} N Z_2 L_n \tag{1.10}$$

where M_2 is the mass of the traversed material nucleus and L_n is the stopping number of nuclear stopping power [20]. Equation (1.11) shows the comparison between nuclear stopping power and electronic stopping power.

$$\frac{-\frac{dE}{dx}|_{nucl}}{-\frac{dE}{dx}|_{elec}} = \frac{m_e}{M_2} Z_2 \frac{L_n}{L_e} \tag{1.11}$$

At the beginning of the injection track, electronic stopping power is the main energy loss process. When the particle velocity decreases to a relatively low value (near the end of the injection track), nuclear stopping power becomes significant [20].

There are three common radiation-induced effects in semiconductor devices including total ionizing dose (TID) effect, single event effects (SEE), and displacement damage. A brief review of each radiation-induced effect will be presented in the following sections.

1.5.2 Total Ionizing Dose Effect

As discussed before, energetic charged particles can ionize the material they are traversing, generating significant amounts of electron-hole pairs along their injection track. The excess charge is separated by intrinsic and applied electric fields. In dielectrics and insulators, the electrons are usually removed due to their higher mobility, leaving holes within the dielectric material. Ionizing radiation-induced charge accumulation in dielectric or insulator layers will change the electrical properties of the semiconductor device and lead to device performance degradation, which includes threshold voltage shift, increased leakage current, reduced gain, and increased noise.

Typically MOS transistors and bipolar transistors are vulnerable to TID effects [21]. The radiation-induced charge buildup inside the oxide leads to device degradation, which is illustrated in Fig. 1.13. Fig. 1.13 is the band diagram of a p-substrate MOS capacitor with a positive gate bias. Right after electron-hole pairs are generated, most of the electrons will drift toward the gate within picoseconds or less. Note that, some of the electron-hole pairs will recombine before electrons leave the oxide, and the rest of the electron-hole pairs are known as the electron-hole yield or charge yield [21]. With an increasing electric field across the oxide, electrons are transported out more efficiently, which will increase the number of holes left after electrons have been removed (charge yield). The holes escaping from initial recombination will drift toward the SiO_2/Si interface by hopping through the localized energy states inside the oxide [21]. A fraction of the holes will be trapped before reaching the SiO_2/Si interface and form long-lived positive trapped charges called oxide traps or bulk traps, which will cause a reduction in threshold voltage for N-type MOS and an increase in threshold voltage in P-type MOS transistors [22]. Further, as holes move through the oxide or are trapped near the interface, hydrogen ions (protons) may be released, which can also drift to the SiO_2/Si interface through the hopping mechanism and contribute to the formation of interface traps [21]. These traps are localized states with energy levels in the Si band-gap, whose occupancy is determined by the Fermi level [22]. Interface traps are mainly positively charged for p-type MOS transistors and negatively charged for n-type MOS transistors at threshold [21].

In addition to radiation-induced trapped charge buildup inside the gate oxide, other oxides including field oxide, silicon-on-insulator (SOI) buried oxide, and other dielectric materials (for example silicon nitride Si_3N_4) may also experience similar effects, which will also cause device degradation and circuit failure [21]. When certain amounts of positive trapped charges are generated in the gate oxide, the channel interface can be inverted, leading to an increased off-state leakage current. Positive charge buildup in field oxide and SOI buried oxide can also induce similar effects by generating parasitic leakage paths in the transistor [21]. Significant amounts of interface traps will decrease carrier mobility and shift the threshold voltage of MOS transistors, which will have an impact on the drive current of

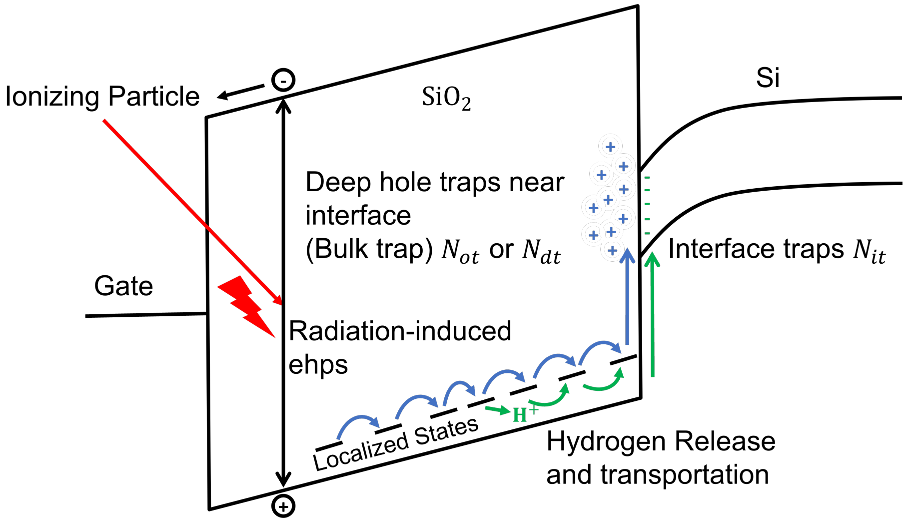

Figure 1.13: Band diagram of a MOS capacitor (p-type Si body) with a positive gate bias. Radiation-induced charge generation is the main cause of TID effects. Picture adapted from [21].

transistors and timing parameters of an integrated circuit (IC) [21].

1.5.3 Single Event Effects

Single event effects (SEE) are radiation effects induced by the injection of a single energetic particle (heavy ion, electron, proton, etc) through semiconductor devices. Energetic particles generate electron-hole pairs along the injection track through direct ionizing and indirect ionizing processes forming a dense ehp column known as an ion track [23]. The diameter of the ion track typically ranges from 10s to 100s of nm depending on the incident particle energy [23]. For SEEs, energetic particles are typically characterized in terms of LET [20]. SEEs can be divided into destructive SEEs and non-destructive SEEs. Common single event effects and their acronyms and brief definitions are listed below [23]:

1. Single event upset (SEU). SEU is a bit flip in a semiconductor memory or logic device caused by a single particle striking a sensitive area.

2. Multiple bit upset(MBU). MBU refers to radiation-induced multiple bits flip in a single cell.

3. Multiple cells upset(MCU). MCU is the bit flip in multiple cells induced by a single incident particle.

4. Single event transient(SET). A transient current or voltage spike is produced inside semiconductor devices.

5. Analog single event transient(ASET). SET happens in an analog device or the analog portion of a mixed signal device.

6. Digital single event transient (DSET). SET happens in a digital device or the digital portion of a mixed signal device.

7. Single event multiple transient (SEMT). Multiple current or voltage transients are generated by a single incident particle in SEMT.

8. Single event latchup (SEL). An anomalous low resistivity current path is formed in a semiconductor device induced by the passage of an incident particle through sensitive regions of the device. SEL may result in the permanent loss of device functionality.

9. Single event functional interrupt (SEFI). A short time period of local functionality interruption is induced, which will further affect the long-term reliability.

10. Single event burnout (SEB). SEB is a localized high-current state which is initiated by the turning on of parasitic conduction paths/devices in the semiconductor device. SEB is one of the main destructive SEEs happening in power semiconductor devices.

11. Single event gate rupture (SEGR). SEGR refers to the formation of a radiation-induced conduction path through the gate dielectric/oxide. SEGR is one of the most common SEEs in MOS transistors.

12. Single event hard error (SEHE). A single irradiation event, which delivers enough total dose or displacement damage to generate an irreversible change in device operation. SEHE is typically associated with permanent damage to one or more components of a device.

Among the various SEEs in semiconductor devices, there are two dominant processes: 1) the generation and collection of electron-hole pairs, and 2) activation of parasitic devices and circuits [23].

1. Generation and collection of electron-hole pairs. The electron-hole pairs generated by the incident particle passage inside the device are partially collected via the well-known carrier transfer processes, drift and diffusion [23]. The carrier collection process will result in a potential deformation, also known as "field funneling", which plays an important role in SEE mechanisms and rate prediction [23]. An illustration of the radiation-induced potential deformation in a reverse-biased PN junction is shown in Fig. 1.14. As discussed before, dense electron-hole pairs are generated along the particle injection track. The radiation-induced electrons and holes respond to the external electric field E_{ex} and move in opposite directions [23]. The separation of ehps leads to a gradually increasing internal electric field E_{in}, which will finally cancel the original external electric field E_{ex}. This screening (neutralization) effect causes a deformation of the potential contour [23]. The equipotential line stretches into the bottom side along the injection track. Potential deformation acts like a funnel, which increases the number of collected carriers at the terminal [23]. Further, the potential deformation is usually associated with high electric field regions at the end of the injection track, which is closely related to destructive SEEs like SEB [23].

2. Activation of parasitic devices and circuits. SEE mechanisms and rate predictions are closely related to parasitic devices and circuits [23]. The cross section of a standard vertical power CMOS device is shown in Fig. 1.15, which consists of two parasitic NPN BJTs. The n$^+$ source region acts as the emitter of the BJT, while the p-body acts as the base. The n-epitaxial layer and layers below it act as the collector. These parasitic BJTs cannot turn on under normal operation. However, the dense ehps generated by an incident particle may result in base current and trigger the parasitic BJTs, resulting in enhanced charge collection [23]. A significant amount of charges will be injected via the parasitic BJTs, which is a greatly magnifying of the actual ion-created charges. This charge collection amplification process induced electric field transient is one of

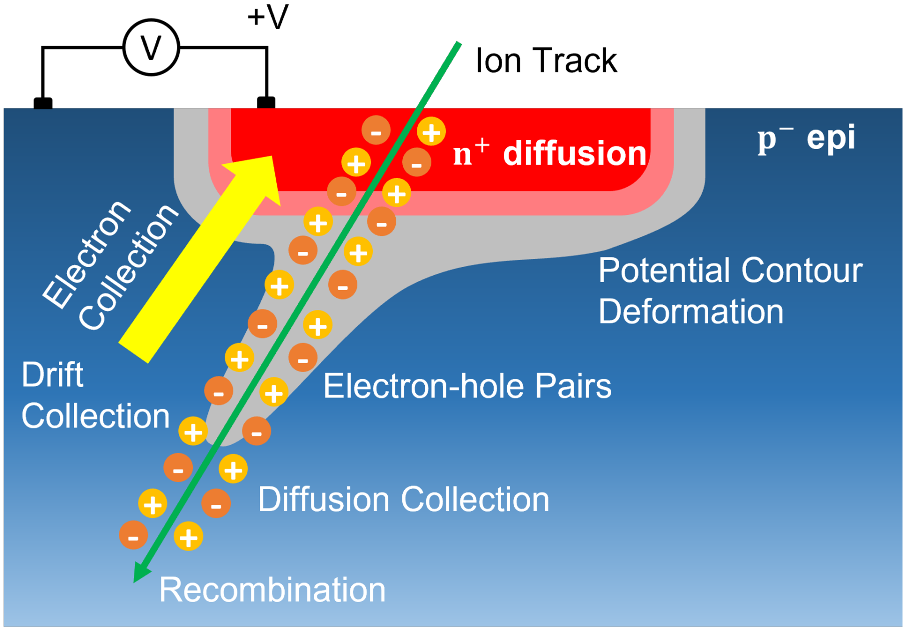

Figure 1.14: An illustration of potential deformation inside a reverse biased PN junction, which is generated by an incident particle. Dense ehps along the injection track are separated due to the external electric field, which results in the internal electric field. The balancing between the external and internal electric fields leads to potential deformation, which is marked by the gray outline.

the main causes of various SEEs, including SEGR in Si-based devices. Moreover, these parasitic devices can form feed-back circuits, which may lead to permanent damage to systems. To prevent destructive SEEs like SEB, SEGR, and SEL, parasitic devices and circuits must be carefully identified and studied.

To further understand SEEs mechanisms, several typical SEEs including SEU (non-destructive), SEB (destructive), and SEGR (destructive) will be discussed in detail.

1. SEU basic mechanism. In spite of circuit topology, the basic operation principle of digital storage elements is to control and hold a certain amount of charge (Q_s) on one or more capacitors (circuit nodes), as shown in Fig. 1.16 (left) [23]. The injected energetic particle generates a large amount of electron-hole pairs (Q_{dep}), which are partially collected by the capacitor. The collected charge Q_{col} affects the charge state of the capacitor and ultimately changes the logic state [23]. The criterion for SEU is

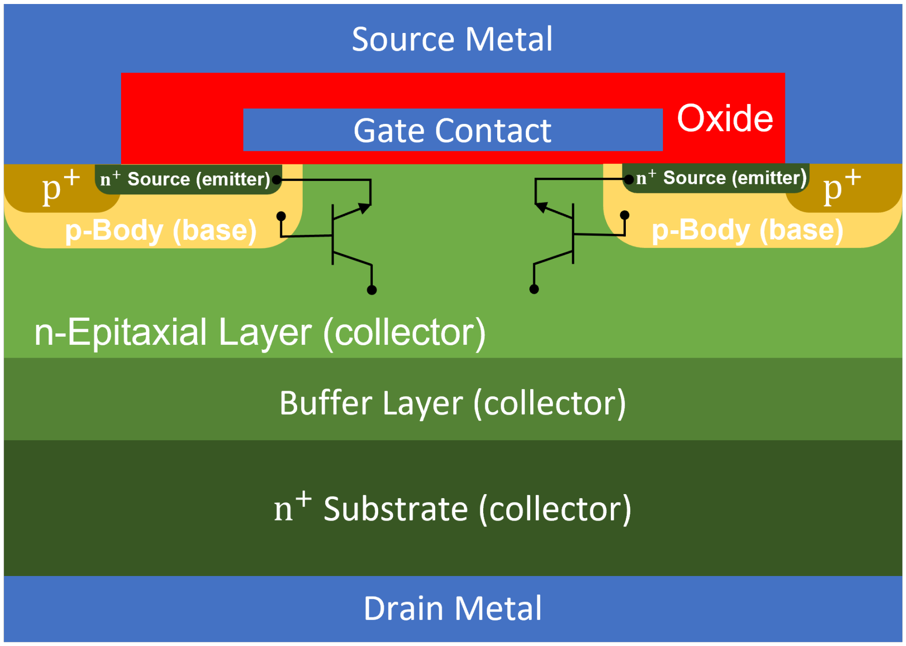

Figure 1.15: Cross section of a vertical power MOSFET with parasitic BJTs. n^+ source acts as the emitter, p-body acts as the base, and the n-epitaxial layer acts as the collector. Picture adapted from [24].

whether Q_{col} can exceed a certain amount of charge to switch the logic value [23]. The minimum amount of charge to switch the logic state is known as critical charge Q_c.

2. SEB basic mechanism. SEB is the result of the formation of variable resistance paths between source and drain, which are typically short-circuited and cause a sudden increase in drain current [23]. As shown in Fig. 1.15, when a certain amount of radiation-induced holes are collected by the p-body, the parasitic BJT will turn on and cause an injection of electrons into the n-epitaxial layer. Further, injected electrons may create ehps through the impact ionization process, while moving toward the drain contact [23]. Holes induced by impact ionization move toward the p-body (base region) and a feedback loop is established, which ultimately leads to device catastrophic failure [23].

3. SEGR basic mechanism. SEGR is a destructive rupture of the gate insulator of power semiconductor devices with a gate oxide/dielectric. Radiation-induced charge accumu-

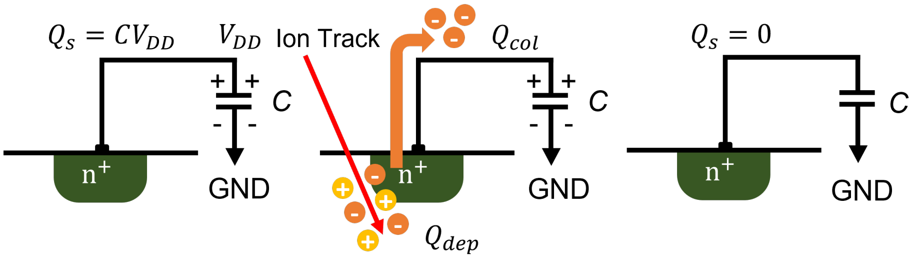

Figure 1.16: The amount of charge Q_s stored on a capacitor is used to maintain the logic value (left). The capacitor collects electrons generated by the injected particle (middle). The collected charge Q_{col} changes the capacitor charge state, resulting in a different logic state (right). Picture adapted from [23].

lation at the dielectric/semiconductor interface is the basic mechanism of SEGR, which is also known as the charge sheet model [23]. An example of the charge sheet model is shown in Fig. 1.17. Radiation-induced electrons will be swept away in a short time period, while radiation-induced holes will be collected and buildup underneath the gate insulator (gate biased under negative voltage). The accumulated sheet of holes results in the electric field increasing across the gate dielectric and power dissipation due to instantaneous current flow, which may lead to dielectric degradation [23]. Additionally, the effects of carrier injection into the gate dielectric have also been proven to have a significant impact on SEGR [23].

1.5.4 Displacement Damage

Theoretical and experimental studies on radiation-induced displacement damage in irradiated materials dates back to the 1940s [25]. Two mechanisms are associated with displacement damage: 1) defect generation, and 2) defect reordering, which have been widely accepted.

1. Defect generation. The energetic particle loses energy inside the target material in two different ways, the production of electron-hole pairs and displaced atoms. Vacancies and interstitials are the initial primary lattice defects induced by displacement damage, where a vacancy is the absence of an atom from its normal lattice location and an

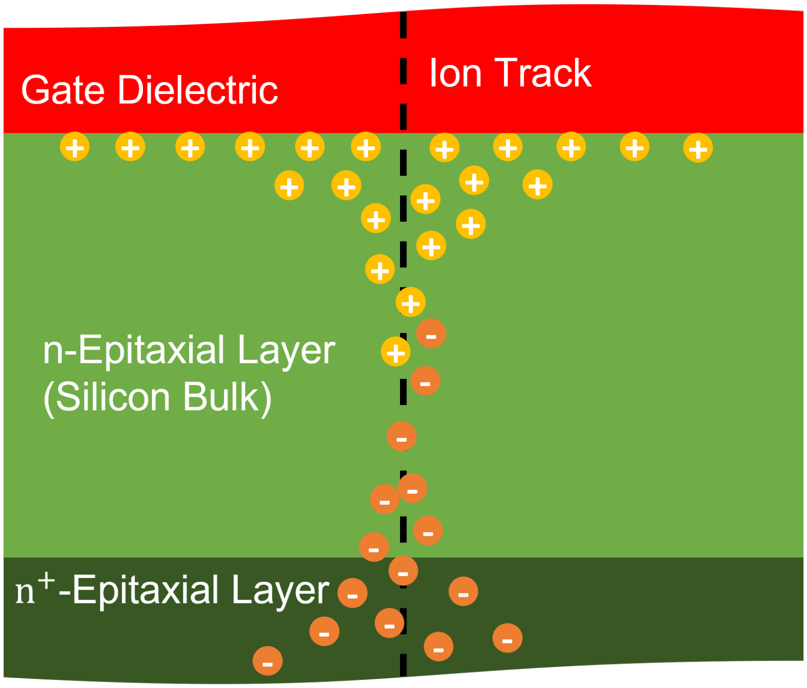

Figure 1.17: Radiation-induced hole accumulation at the dielectric/semiconductor interface. Gate is biased under negative voltage. The black dashed line represents the particle injection track. Picture adapted from [23].

interstitial refers to an atom moving into an empty space or interstice in the material lattice [25]. Typically, an incoming particle that creates displacement damage will induce a vacancy and an interstitial at the same time. The combination of a vacancy and an adjacent interstitial is known as a close pair or a Frenkel pair [25]. Two adjacent vacancies form another defect type, which is known as a divacancy [25]. When vacancies and interstitials are adjacent to impurity atoms, additional defects will form, referred to as defect-impurity complexes [25].

Point defects, or isolated defects, refer to radiation-induced defects, which are relatively far apart from each other. On the other hand, when radiation-induced defects are relatively close to each other, a local region disorder called a defect cluster or a disordered region will form. Overall, incident energetic particles produce a mixture of point and clustered defects inside the target material [25].

2. Defect reordering. Defect reordering is also known as annealing, typically implying a reduction in the amount of damage and corresponding effectiveness (forward annealing). However, defect reordering may also result in more effective defects, which will induce further degradation inside the devices. This process is known as reverse annealing [25]. Radiation-induced defects will reorder to form more stable configurations, once they are generated inside the material [25]. For example, radiation-induced vacancies in silicon are unstable and have relatively high mobility at room temperature. Point defects in silicon tend to move through the lattice and form more complex defects like divacancies and vacancy-impurity complexes, which have a significant impact on semiconductor device properties [25]. Note that, defect reordering has a temperature dependence (temperature annealing) and an existing excess carrier concentration dependence (injection annealing) [25].

In general, radiation-induced displacement damage effectiveness depends on various parameters, including particle type, particle LET, temperature, time after radiation, material properties, etc [25]. The radiation-induced defects are associated with new energy states generated inside the semiconductor material bandgap, which have a significant impact on the material's electrical and optical behaviors. A brief overview of displacement damage effects on the electrical properties of semiconductor devices will be presented.

The first effect is the thermal generation of electron-hole pairs through a level near midgap [25]. This process starts with the thermal excitation of a valance band electron to the defect states near midgap and the electron is subsequently excited to the conduction band, resulting in a free electron-hole pair. Note that only the defect states near midgap energy of the material play an important role in ehps generation. Additionally, emission processes dominate over capture processes at a defect state only when the free carrier concentrations are significantly smaller than their thermal equilibrium values [25]. Therefore, thermal generation of electron-hole pairs through defect states near midgap has a significant impact in device depletion regions, which is the mechanism for leakage current increasing in silicon devices [25].

The second effect is the recombination of electron-hole pairs, in which the defect state captures a free carrier of one sign (electron or hole) and captures another carrier with the opposite sign [25]. The recombination rate is closely related to defect state density, carrier concentration, the electron and hole capture cross sections, and the energy level position of the defect state [25]. Radiation-induced recombination centers lead to carrier lifetime reduction, which is responsible for radiation-induced gain degradation in BJTs [25].

The third effect is the temporary trapping of carriers at a typically shallow level, in which a carrier is captured by a radiation-induced defect state and is later emitted to its band without recombination [25]. Trapped carriers can either be majority carriers or minority carriers depending on the defect state energy level.

The fourth effect is the compensation of dopants (acceptors or donors) by radiation-induced energy states [25]. For example, in p-type material deep-lying radiation-induced donor-like traps compensate part of the free holes available from the acceptor level, which leads to a reduction of the equilibrium majority-carrier concentration [25].

The fifth effect is defect-assisted tunneling through a potential barrier, which is also known as trap-assisted tunneling [25]. The defect-assisted tunneling will cause abnormal leakage current in semiconductor devices, for example, leakage through the gate dielectric.

The sixth effect is the carrier mobility reduction, which is due to radiation-induced defect states acting as scattering centers [25]. The carrier mobility decreases with increasing defect density inside the target material.

The seventh effect is type conversion due to displacement-damage-induced carrier removal [25]. For example, in n-type bulk germanium, radiation-induced acceptor states lead to increased resistivity, which eventually causes the conversion to p-type material [25]. Silicon-based devices are typically insensitive to this effect.

The eighth effect of displacement-damage-induced defect states is enhanced effectiveness for thermal generation of carriers, which will occur at high electric field regions [25]. This effect can reduce the potential barrier for thermal generation (Poole-Frenkel effect).

In general, displacement-damage-induced defect states are associated with multiple effects, including carrier generation, carrier recombination, charge trapping, compensation, carrier tunneling, scattering, type conversion, and field enhancement of carrier generation effectiveness [25]. The effects of a certain energy state depend on various parameters, such as carrier concentration, operating temperature, and the physical location of the defect inside the device. Moreover, highly ordered materials like single-crystal silicon are more sensitive to displacement damage as their properties are closely related to their high-order structures. For polycrystalline or amorphous materials, no significant effects will be observed until substantial displacement damage is accumulated. Theoretically, materials like GaN, which consist of a large number of intrinsic defects, should be relatively insensitive to displacement damage.

1.6 Gate Dielectric Breakdown Mechanisms

SEGR is a dielectric failure induced by an ion that generates a transient voltage (or electric field) that exceeds the dielectric strength of the insulator [26]. Previous research has shown that electrical stress-induced dielectric breakdown, also known as time-dependent gate dielectric (oxide) breakdown (TDDB), and radiation-induced dielectric breakdown processes (SEGR) are analogous in many respects [27].

Under low stress, often small increases are observed in gate current indicative of partial or soft breakdown (SBD). The electrical stress-induced dielectric breakdown usually progresses in a stair-step fashion, with subsequent SBD events further increasing the leakage over time (voltage stress). Ultimately the accumulation of multiple SBD events in a localized area will lead to a high conduction state typified by a large gate current. This is referred to as a hard breakdown (HBD). Note that under high voltage stress a gate dielectric may simply suffer an HBD event with no observed SBDs. Analogously, radiation-induced dielectric breakdowns are observed over time (ion fluence). For clarity, we refer to these types of events as radiation-induced SBD and HBD. Both mechanisms are related to a localized failure and can be detected as a significant increase of the leakage current through the dielectric [28]. SBD is usually referred to as an abnormal increase in gate leakage current and HBD is a catastrophic failure (short across the dielectric). Both breakdown processes have been widely studied and are commonly agreed to be triggered by effects associated with electron-hole pair generation [29], [30]. More specifically, carrier transport and energetic particle interactions in the thin-film dielectric lead to increasing both bulk and interface defect densities in the dielectric. Radiation-induced SBD and HBD will occur when the defect density in the dielectric reaches a critical level. A number of dielectric breakdown models involving hot carriers have been proposed and widely discussed in the literature, which can be categorized into three different types: 1) defect-generation model, 2) carrier-conduction driven model like $\sqrt{E}$ models, and 3) fluency-induced defect generation models such as the anode-hole injection (AHI) model, and anode hydrogen-release (AHR) model [31], [32]. In this section, a brief overview of the present understanding and experimental observations of electrical stress-induced dielectric breakdown focusing on breakdown statistics and degradation models will be provided.

Dielectric breakdown is a stochastic process that necessitates a statistical description [32]. The Weibull distribution, which belongs to the family of extreme-value distributions, has been proven to be the most accurate representation of the random nature of dielectric breakdown in the form of the cumulative density function (CDF), given by the following equation [32]:

$$F(t) = 1 - e^{-(\frac{t}{T_{63}})^{\beta}} \tag{1.12}$$

where F is the failure rate, t is the statistical variable, T_{63} is the scale factor at 63.2%, and $beta$ is the shape factor, also known as the Weibull slope [32]. Equation (1.12) is commonly given as:

$$\begin{aligned} W(t) &= ln(-ln(1 - F(t))) \\ &= \beta ln(t) - \beta ln(T_{63}) \end{aligned} \tag{1.13}$$

The Weibull distribution is known to be compatible with the weakest-link property of dielectric breakdown [32], which represents the most fundamental characteristics of dielectric breakdown, and the corresponding mathematical equation for any two areas A_1 and A_2 is given by:

$$W_2(t) = W_1(t) + ln(\frac{A_2}{A_1}) \tag{1.14}$$

which is also known as Poisson area scaling. Therefore, the scale factor T_{63} and the area $A^{\frac{1}{\beta}}$ are inversely proportional, which has been widely observed among different dielectric materials [32].

The percolation model can predict a decrease in the shape factor β with a reduction in dielectric thickness t_{diel}, which is an important advancement in the field of dielectric breakdown. The concept that dielectric breakdown will be triggered when the critical defect density N_{BD} is reached has been widely accepted. The percolation model provides insight into the connections between the critical defect density N_{BD} and dielectric thickness t_{diel}. The original percolation model relates dielectric breakdown to the defect filament formation inside the dielectric [32].

There are four dielectric breakdown time (T_{BD}) acceleration models used to fit experimental data, which have been widely accepted and discussed in the literature, including the exponential law of field/voltage dependence [32]:

$$\begin{aligned} T_{BD} &= T_{BD0}e^{-\gamma_V V} \\ T_{BD} &= T_{BD0}e^{-\gamma_E E} \end{aligned} \tag{1.15}$$

the exponential law of reciprocal field/voltage dependence [32]:

$$\begin{aligned} T_{BD} &= T_{BD0}e^{\frac{G_V}{V}} \\ T_{BD} &= T_{BD0}e^{\frac{G_E}{E}} \end{aligned} \tag{1.16}$$

the $\sqrt{E}$ model [32]:

$$\begin{aligned} T_{BD} &= T_{BD0}e^{-\eta_V \sqrt{V}} \\ T_{BD} &= T_{BD0}e^{-\eta_E \sqrt{E}} \end{aligned} \tag{1.17}$$

and the power law voltage/field dependence [32]:

$$\begin{aligned} T_{BD} &= ZV^{-m} \\ T_{BD} &= ZE^{-m} \end{aligned} \tag{1.18}$$

where γ_V, γ_E, η_V, η_E, G_V, G_E, and m are the voltage or field acceleration factors of the four models [32]. T_{BD0} and Z are the prefactors. However, how to appropriately choose the acceleration model has a significant impact on the final projection results, which has been intensively debated for decades [32].

Besides voltage/electric field, dielectric breakdown is also closely related to temperature. In other words, dielectric breakdown is a temperature-activated process [32]. Generally, with increasing temperature, voltage, or electric field acceleration factors are found to decrease [32].

A universal framework of dielectric breakdown models, which characterizes multiple factors that impact the breakdown process including carrier injection fluence, and defect generation rate, can be derived as (based on first-order defect generation efficiency) [32]:

$$T_{BD} = \frac{q t_{dielN_{BD}(A_{diel,t_{diel}})}}{J(V,T,t_{diel})\xi(V,T,t_{diel})} \tag{1.19}$$

where q is the electron charge. $J(V,T,t_{diel})$ is the carrier conduction current through the dielectric by quantum mechanical tunneling or defect-assisted tunneling, which depends on applied voltage V, operation temperature T, and t_{diel}. Critical defect density N_{BD} is a function of dielectric area A_{diel} and t_{diel}, which describes statistical breakdown behaviors such as β dependence upon t_{diel} and T_{BD} dependence upon A_{diel} [32]. $\xi(V,T,t_{diel})$ is the defect generation rate related to voltage or field and temperature, and can also be written as P_{gen}. With this equation, various TDDB models can be categorized into three types [32]:

1. Defect generation models, such as the E model and the bond-breakage model.
2. Carrier-conduction driven models, including the well known $\sqrt{E}$ model.
3. Fluency-induced defect generation models, such as the anode hydrogen-release model (AHR), the anode hole injection model (AHI), the impact-damage model, and the intraband impact ionization 1/E model.

The well-known E model is based on a thermochemical bond-breakage mechanism, which is induced by the lowering of thermal activation energy due to applied field [32]. The defect generation rate $\xi(E)$ is given by:

$$\xi(E) \sim e^{\frac{(\gamma_E E - \Delta H)}{k_B T}} \tag{1.20}$$

where ΔH is the activation energy for Si-O bond breakage. γ_E is the field acceleration factor. E and T represent the electric field across the dielectric and the operating temperature. k_B is Boltzmann's constant. Recent research results from transmission electron microscopy (TEM) and electron energy loss spectroscopy (EELS) show that defects are fundamentally oxygen vacancies as a result of dielectric breakdown, which provides support to the E model [32].

The $\sqrt{E}$ model is the widely accepted breakdown model in the back end of line (BEOL) and middle of line (MOL) reliability community [32]. A correlation between T_{BD} and current conducted through the dielectric has been reported in the forward end of line (FEOL) gate dielectrics and BEOL/MOL dielectrics [33–37], which indicates that the field-acceleration model follows a $\sqrt{E}$ dependence as the Poole-Frankel (PF) mechanism (defect-assisted electron transportation) dominates electron conduction through the dielectric. The field-dependent steady-state current J can be described by [38]:

$$log(J) = a + b\sqrt{E} + log(1 - c\sqrt{E} - \frac{d}{E}) \tag{1.21}$$

where a, b, c, d are fitting parameters (more details are presented in [38]).

Hole generation is the main defect generation process in the 1/E model and AHI models. In the 1/E model, holes are generated by incoming electrons within the dielectric via intraband impact ionization, which usually occurs in ultrathick dielectrics [32]. Both the Fowler-Nordheim (FN) tunneling current and impact ionization rate for electron-hole pair generation have a 1/E dependence. In AHI model, a fraction of the electrons tunneling through the dielectric transfers energy to deep valence band electrons of the anode material. This process generates hot holes, which tunnel back into the dielectric. Note that, AHI usually happens in ultrathin dielectrics.

The Anode hydrogen-release model considers the hydrogen-release process as the key dielectric breakdown mechanism, which is a two-step species-release process: [39]

1. The injected electron causes the release of hydrogen ions (positively charged) at the

anode interface.

2. A fraction of the released hydrogen ions migrates in the dielectric to react with precursor damage and creates defects.
3. A fraction of the released hydrogen ions escapes the dielectric without creating any defect.

Overall, there are at least four defect-generation mechanisms associated with dielectric degradation under DC stressing. The first two mechanisms are impact ionization and anode hole injection, which typically occur at higher voltage bias conditions and are responsible for hole trapping and hole-related defect generation [31]. Defect generation due to the hydrogen release process has a lower threshold voltage, which can occur at 1.2V or lower stressing voltage. In the thermochemical-related defect generation mechanism, a field-driven process dominates defect generation inside the dielectric, and hot carrier injection plays at most a secondary role. However, despite the origins of defects, destructive dielectric degradation will be triggered when the defect density reaches the critical level.

1.7 Chapter Summary

High-energy radiation can deposit energy in the semiconductor devices through two mechanisms: 1) electronic ionization or direct ionization, and 2) atomic collision, including non-ionizing processes, and indirect ionization. The significance of these two mechanisms within a semiconductor structure varies based on the radiation type and the characteristics of the device [40]. For electron, proton, X-ray, and gamma-ray environments, the ionization process takes most of the deposited energy, which results in excitation and pair production [40]. For terrestrial neutron environments, a large fraction of the deposited energy is due to atomic collisions, which contribute to displacement damage and indirect ionization. Therefore, radiation can introduce various effects on semiconductor devices and circuits, ranging from temporary performance disorder to permanent destructive damage.

Wide-bandgap power devices are attractive due to their unique ability to operate at high voltages, high temperatures, and high switching frequencies, while providing very low on-resistance, features enabling significantly improved power conversion efficiency. The two primary wide-bandgap materials that have recently become ubiquitous in the power industry are silicon carbide (SiC) and gallium nitride (GaN). SiC can typically sustain higher operating voltages than GaN, but GaN has lower power consumption, lower switching loss, and higher electron mobility. Among the wide-bandgap power devices, AlGaN/GaN high electron mobility transistors (HEMTs) have the potential to provide high reliability in harsh environments due to their outstanding robustness and efficiency. However, GaN-based power devices can also be sensitive to radiation-induced effects at bias conditions below their nominal rated limits, requiring them to be operated at reduced voltages (voltage derating) when they are used in harsh radiation environments. Additionally, since GaN-based technologies have much higher defect densities than those of conventional silicon-based devices, GaN-based devices may suffer from higher device-to-device variation in their radiation robustness.

The primary goal of this work is to elucidate the dominant mechanisms and variables that define the destructive radiation-induced effects on performance of power GaN HEMTs, and improve system reliability at higher bias voltages in aerospace and other high reliability applications. In Chapter 2, a brief review of X-ray-induced TID effects in GaN HEMTs will be presented. In Chapter 3, heavy-ion radiation tolerance of GaN HEMTs has been studied as a function of bias conditions (V_{GS} and V_{DS}), ion LET, injection location, and radiation flux. Both experimental data and simulation results are presented. An exhaustive study of terrestrial neutron-induced SEEs in GaN HEMTs is covered in Chapter 4. Based on the experimental data and simulation results, a percolation theory-based gate dielectric degradation model is proposed, which is described in Chapter 5. A summary of this dissertation will be presented in Chapter 6.

Chapter 2

X-Ray Induced Total Ionizing Dose Effects in GaN HEMTs

2.1 Experimental Details

This dissertation is focused on the radiation effects on a commercially available D-mode GaN HEMT. All the devices under test (DUTs) for the TID effects study are fabricated and packaged inside 32-pin quad flat no lead (QFN) packages (as shown in Fig. 2.1) by a commercial vendor. A simplified cross-section of the D-mode HEMT structure is shown in Fig. 2.2. The two-dimensional electron gas (2DEG) channel is formed at the interface between the GaN and AlGaN layers. The asymmetric structure and field plate above the gate contact ensures higher drain voltage tolerance with a thinner gate dielectric. As shown in Fig. 2.3 the average threshold voltage for this device is -10V (σ=1V). Thus, -14 V gate bias ensures the device is under blocking operation during stress. The maximum operating voltage of this D-mode GaN HEMT is 600 V.

The DC electrical measurements were carried out with a Cascade probe station and NI PXIe system as shown in Fig. 2.4. Three NI PXIe-4135 single-channel source measurement units (SMUs) are installed inside the NI system, which have an output voltage range from -200 V to 200 V and an output current range from -3 A to 3 A. The maximum DC source power is 20 W and the maximum DC sink power is 12 W. The current sensitivity is 10 fA depending on the system configuration. NI LabVIEW programs installed in the embedded controller are used for controlling characterization measurements including DC stressing, and IV sweep (I_D vs V_{GS} characteristic IV curve). On resistance (R_{on}) of each DUT is measured using a Quadtech LR2000 milli ohmmeter with the four-point-probe method. The LR 2000 QuadTech milli ohmmeter measures from 1 mΩ to 2 MΩ over 8 Ranges, with 0.05% basic measurement accuracy.

The X-RAD iR-160 compact cabinet industrial X-ray irradiator (as shown in Fig. 2.5)

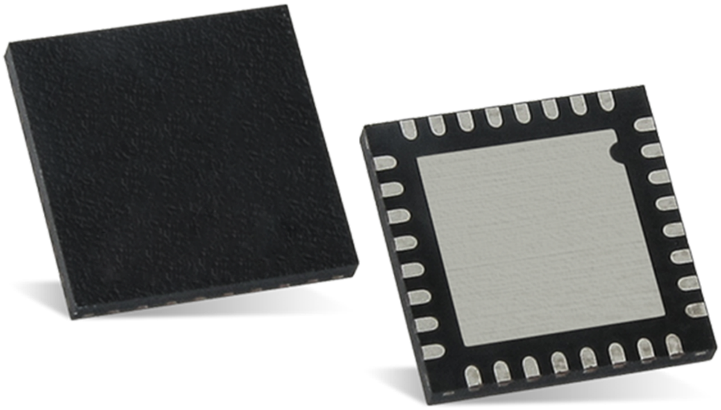

Figure 2.1: A picture of commercially available D-mode GaN HEMT packaged in a 32-pin QFN package. Left is the front side (plastic side) and right is the backside (metal side). X-ray photons can easily penetrate the plastic mold compound and reach the die.

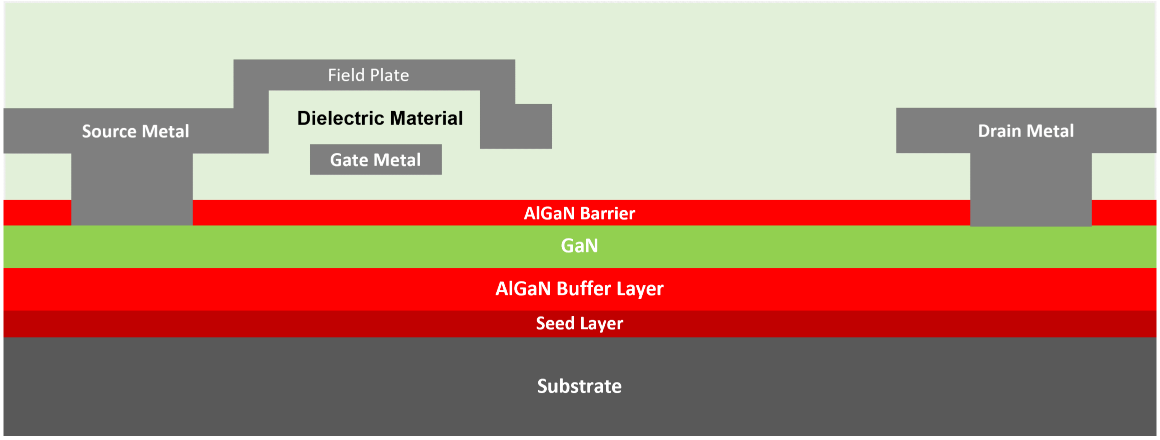

Figure 2.2: Basic structure of the D-Mode GaN HEMT. The schematic of the cross section is simplified. The actual spacing is different. The asymmetric structure and field plate above the gate contact ensures higher drain voltage tolerance with a thinner gate dielectric.

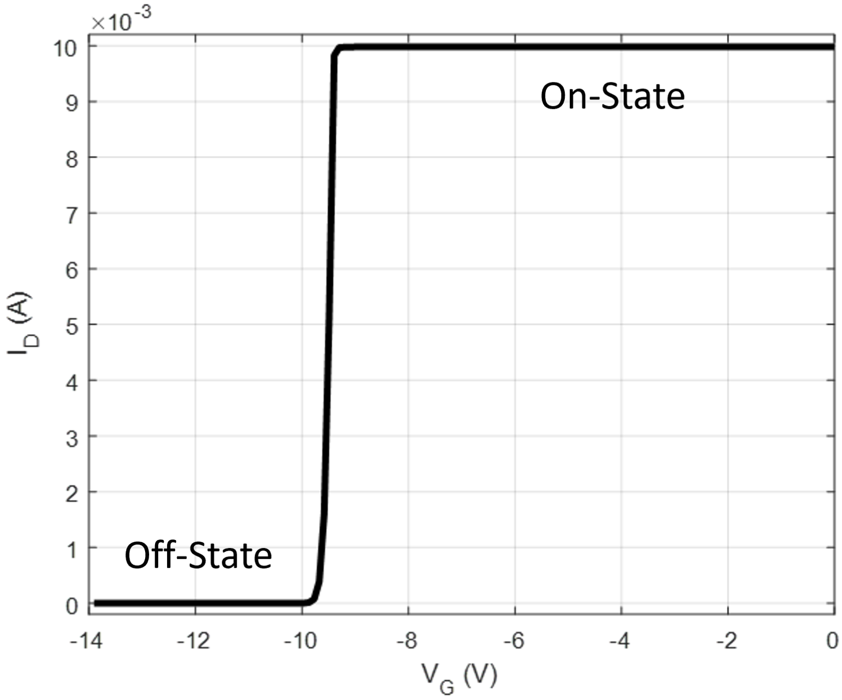

Figure 2.3: A typical IV curve of the D-Mode GaN HEMT. Gate voltage (V_{GS}) is swept from -14 V to 0 V. Drain voltage (V_{DS}) is held at 0.1 V with a drain current limit of 10 mA. The depletion-mode characteristics are clear in that the channel is "ON" until it is shut off by an applied gate voltage of about -10V.

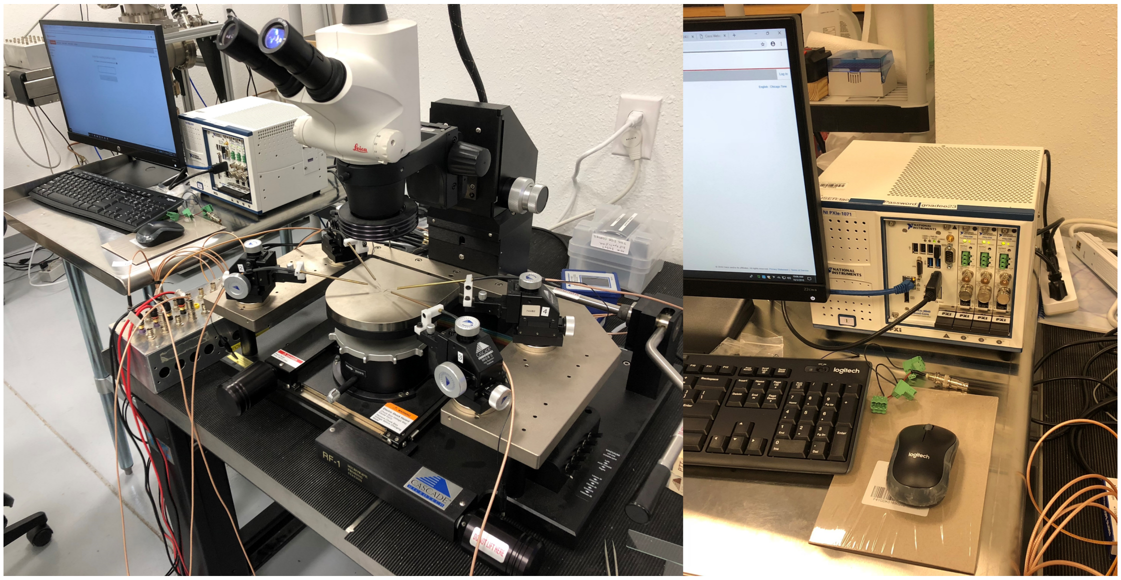

Figure 2.4: A photo of TID effects DC measurement system, consisting of a wafer-level probe station with four probes (left) and a NI PXIe system (right). Three current-voltage source-monitor channels (one for drain, gate, and source-substrate) and an embedded controller are installed in the NI PXIe system.

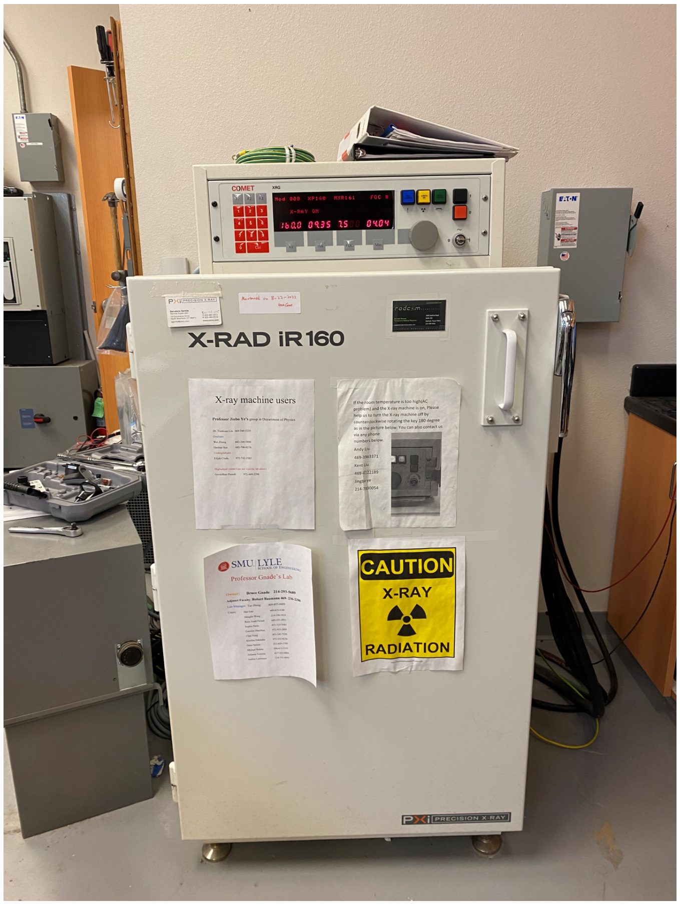

Figure 2.5: A photo of the X-RAD iR-160 compact cabinet industrial X-ray irradiation system. The cabinet X-ray system consists of XRP generator (control unit, power supply, and high-voltage (HV) tank), cabinet, and water cooler.

was used for X-ray radiation experiments at the SMU Reliability Lab. The fixed anode X-ray tube (water-cooled) consists of a Cu target and a 2 mm Al filter. The maximum potential of the X-ray tube is 160 kV. Dose output of the raw beam is about 60 Gy/min (6000 rad/min) at 160 kV, 19 mA, and 30 cm source-skin distance (SSD). Dose output of the filtered beam is about 6.5 Gy/min (650 rad/min) at 160 kV, 19 mA, and 30 cm SSD. Note that, X-ray photons can easily penetrate the packaging material and directly interact with the die [41].

X-ray TID effects in D-mode GaN HEMTs have been studied as a function of radiation fluence and device bias condition. Three different types of experiments were carried out, including total dose irradiation with all device terminals floating, total dose irradiation with

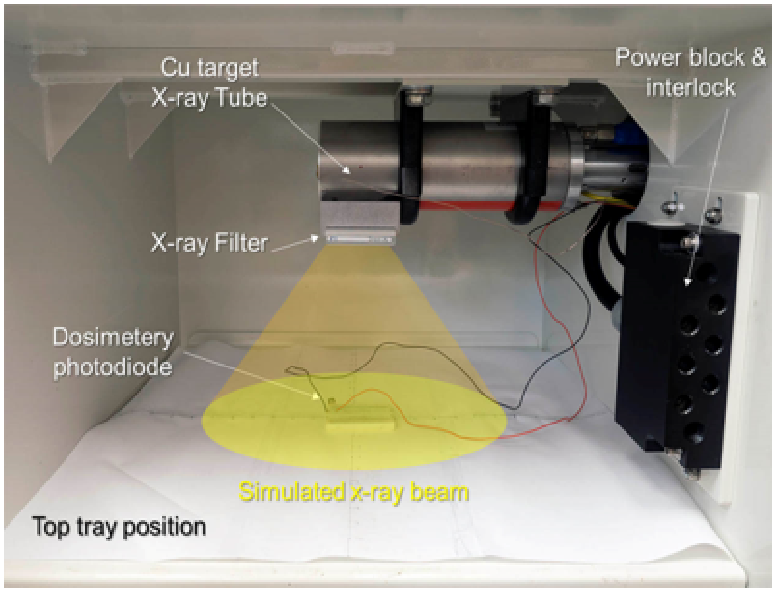

Figure 2.6: A photo of the Cu-target X-ray tube. Electrical contacts can go into the cabinet through the hole on the right side. The corresponding SSD of the top tray position is 10 cm.

gate bias (source grounded, drain floating), and total dose irradiation with gate bias and drain bias (source grounded). All experiments share a similar testing procedure:

1. Transistor characterizations
2. V_{DS} = 600 V, V_{GS} = -14 V, 60 s DC stress
3. Transistor characterizations
4. X-ray radiation (floating/gate bias with source grounded/gate bias and drain bias with source grounded)
5. Transistor characterizations
6. Room-temperature (RT) annealing
7. Transistor characterizations
8. V_{DS} = 600 V, V_{GS} = -14 V, 60 s DC stress
9. Transistor characterizations

Table 2.1: Results of total dose irradiation experiments with all device terminals floating. Both front-side and back-side radiation experiments have been performed.

Device	V_{th} (V)	ΔV_{th} (V)	R_{on} (mΩ)	Cu. Dose (Krad)	Post Process
134	-9.42	0	72.89	0	DC Stress
134	-10.27	-0.85	73.16	0	10 krad (Si), Front side
134	-10.61	-0.34	65.93	10	24 h RT annealing
134	-10.03	0.58	65.69	10	DC Stress
134	-8.7	1.33	68.04	10	48 h RT annealing
134	-8.7	0	70.24	10	10 krad (Si), Back side
134	-9.83	-1.13	66.72	20	17 h RT annealing
134	-9.71	0.12	66.88	20	4 h RT annealing
134	-9.67	0.04	66.73	20	DC Stress
134	-9.70	-0.03	68.49	20	50 krad (Si), Back side
134	-10.34	-0.64	65.29	70	24 h RT annealing
134	-10.09	0.25	66.10	70	DC Stress
134	-8.98	1.11	67.60	70	NA
58	-9.16	0	68.98	0	DC Stress
58	-9.66	-0.5	69.60	0	100 krad (Si), Back side
58	-10.47	-0.81	62.94	100	24 h RT annealing
58	-10.16	0.31	63.40	100	DC Stress
58	-8.82	1.34	65.76	100	NA

where transistor characterizations includes IV sweep (I_D vs. V_{GS}) and R_{on} measurement. Notice that, 600 V off-state DC stress (step 2 and step 8) is used for resetting V_{th} of the D-mode GaN HEMTs.

2.2 Experimental Results and Discussion

Results of total dose irradiation experiments with all device terminals floating are presented in Table 2.1. As expected, threshold voltage (V_{th}) shift (negative direction) is the main X-ray-induced TID effect in GaN HEMTs. On resistance (R_{on}) is relatively immune to X-ray radiation. No destructive damage was observed. X-ray-induced threshold voltage shifts for floating devices are small ($\leq$ 1.1 V), as without an external electric field most radiation-induced charges will recombine in a short time period before damaging the irradiated devices.

Table 2.2 shows the results of total dose irradiation with gate bias (source grounded, drain floating, and $V_{GS} = -14V$). With -14 V on the gate, the channel region below the gate is non-conductive (in the off-state). X-ray-induced V_{th} shifts have been observed. Post-radiation threshold voltage shifted to the negative direction, due to trapped holes above the 2DEG channel. Compared with the irradiation results without gate bias, V_{th} shifts are considerably larger because of enhanced charge collection efficiency. Notice that, after the last 100 krad (Si) radiation, V_{th} shifted 3.8 V in the positive direction, which is the result of trapped electrons. The fact that V_{th} shifting direction can either be positive or negative indicates competition between at least two different types of charge traps. Based on experimental results, hole trapping seems to be the dominant mechanism at low-dose conditions, while at high-dose conditions electron trapping is the dominant process. Electrons and holes may also be trapped at different locations inside the device. Further, the threshold voltage shift can recover over time, but with the accumulation dosage going up, the recovery becomes less effective (from almost full recovery to almost no recovery), which is closely related to the radiation-induced trapped charge lifetime. It has been observed that a DC stress is able to reset the threshold voltage despite the X-ray effects, where the shifting direction can either be positive or negative, depending on the pre-stressing V_{th}. In most cases, DC stress can reset the V_{th} back to approximately -9 V, indicating interface states (hole traps and electron traps) at the dielectric/AlGaN interface are the main cause of X-ray-induced threshold voltage shift.

Unlike the other radiation experiments, I_D and I_G were continuously measured during total dose irradiation with gate bias and drain bias (source grounded, V_{GS}=-14 V). Instead of using a constant drain voltage, the drain voltage was ramped up from 0 to 600 V (the total number of steps is 13 and the step size is 50 V), and the stressing time of each step is 6 mins, which is equivalent to 10 krad (Si) X-ray radiation, and 130 krad (Si) in total. In this way, drain voltage effects on device response to X-ray radiation can be efficiently studied. Fig. 2.7 shows the gate current of sample 58 changes versus radiation time. Each voltage step is marked by different colors and the dash lines represent the beginning of each step. No significant change in off-state gate leakage current was observed. V_{th} shifting to the positive direction was observed, which was due to trapped electrons above the 2DEG

Table 2.2: Results of total dose irradiation with source grounded, drain floating and V_{GS}=-14 V.

Device	V_{th} (V)	ΔV_{th} (V)	R_{on} (mΩ)	Cu. Dose (Krad)	Post Process
134	-8.98	0	70.57	70	DC Stress
134	-8.90	-0.08	70.85	70	50 krad (Si), Back side
134	-10.30	-1.4	67.05	120	24 h RT annealing
134	-8.10	2.2	70.75	120	DC Stress
134	-6.90	1.2	68.86	120	50 krad (Si), Back side
134	-10.00	-3.1	67.45	170	24 h RT annealing
134	-6.8	3.2	68.22	170	DC Stress
134	-9.20	-2.4	69.54	170	24 h RT annealing
134	-7.60	1.6	71.52	170	DC Stress
134	-7.90	-0.3	68.02	170	100 krad (Si), Back side
134	-4.10	3.8	63.25	270	24 h RT annealing
134	-4.90	-0.8	65.43	270	DC Stress
134	-8.10	-3.2	68.88	270	NA

channel, as shown in Fig. 2.8. Compared with total dose irradiation with gate bias, the V_{th} shift is relatively small, because under higher drain bias, the lateral electric field across the device is stronger, which will sweep away the accumulated charges at a faster speed. In general, the drain bias has little effect on X-ray-induced TID effects on GaN HEMTs.

Overall, D-mode GaN HEMTs are relatively insensitive to X-rays (even under a high dose environment and high drain bias), which is consistent with our expectation, as wide-bandgap materials require considerably higher energy to generate an electron-hole pair than silicon. In other words, X-ray-induced charge density is significantly lower in GaN compared with Si. V_{th} shift is the main TID effect observed, which can recover over time, indicating no permanent damage formed inside the device. With gate and drain bias, X-ray radiation can induce larger threshold voltage shifts, due to enhanced charge separation and collection efficiency. Two different trapping mechanisms were observed including hole trapping and electron trapping, which seem to be related to X-ray dose level (fluence). A higher X-ray dose will induce larger V_{th} shifts. DC stress can efficiently depopulate both trapped holes and trapped electrons and reset the threshold voltage. Note that, even experiencing the

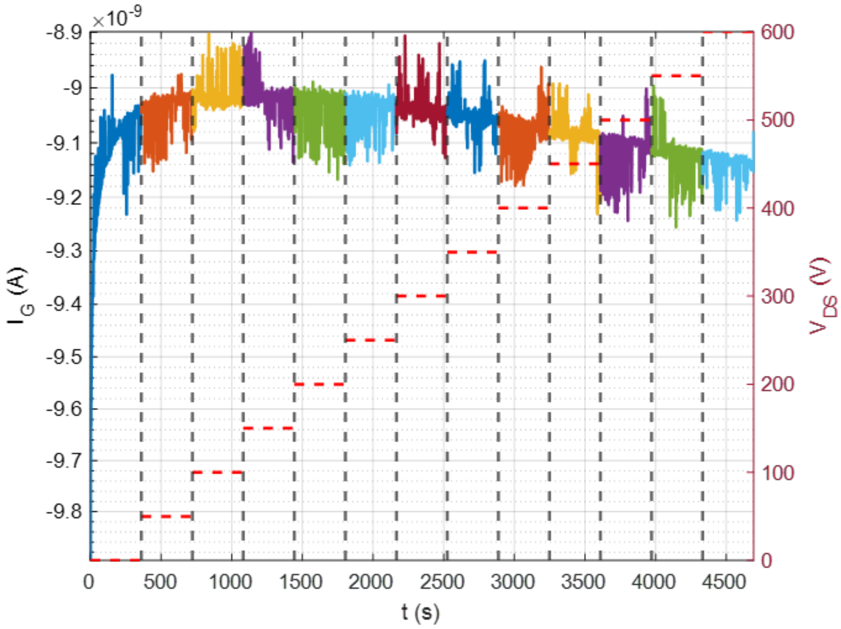

Figure 2.7: I_G vs. time under X-ray radiation with V_{DS} ramping up from 0 to 600 V (13 steps). Black dash lines represent the beginning of each step. The red dash line is the drain voltage. V_{GS}=-14 V, and source is grounded. Each step lasts 360 s and represents a dose of 10 krad (Si) X-ray radiation (130 krad (Si) in total).

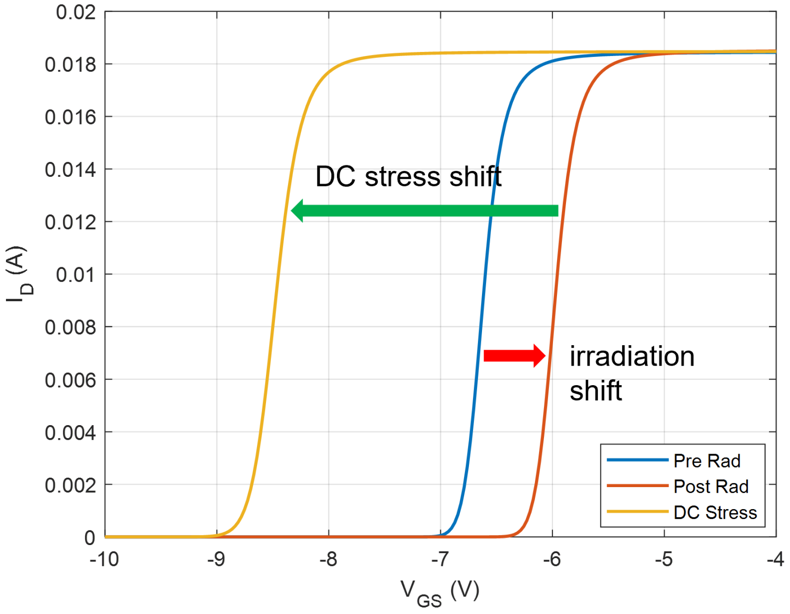

Figure 2.8: Pre-radiation IV curve, post-radiation IV curve, and IV curve after 600 V DC stress. After being exposed to 130 krad X-ray radiation with gate and drain bias, sample 58 showed a relatively small V_{th} shift to the positive direction due to hole trapping. A 600 V DC stress (60 s) can sufficiently reset V_{th}.

largest V_{th} shift, -14 V gate bias still can fully shut off the channel and 0 V gate bias can turn on the channel efficiently, which indicates the functionality of the D-mode GaN HEMT is unharmed. However, in some applications, the threshold voltage shifts observed in X-ray irradiation experiments may lead to degraded power performance or in rare cases circuit failure. No significant gate leakage current was observed in any of the experiments. On-resistance is insensitive to X-ray radiation.

Chapter 3

Heavy Ion Radiation Induced Single Event Effects in GaN HEMTs

In this chapter, we studied the heavy-ion radiation tolerance of AlGaN/GaN high electron mobility transistors as a function of device bias (gate voltage V_{GS} and drain voltage V_{DS}), ion LET, and radiation flux dependence. Heavy-ion-induced gate dielectric degradation was observed, typified by a multistage degradation process combining radiation-induced and field-driven soft breakdown (SBD) and hard breakdown (HBD) events. Results from post-radiation characterization measurements indicate an accumulation of radiation-induced defects inside the dielectric. To further investigate the failure mechanisms, critical injection level experiments were designed and carried out, in which a constant current was forced through the 2DEG channel under heavy-ion radiation. The corresponding results illustrate that heavy-ion-induced electron-hole pairs dominate the SEGR response of the D-mode GaN HEMT.

A two-dimensional (2D) device model of the GaN HEMT was created using the SILVACO Atlas Technology Computer-Aided Design (TCAD) tools. The 2D simulator was used to perform a large number of transient device simulations to understand the impact of heavy ions in the GaN HEMT power devices as a function of their bias conditions (V_{GS} and V_{DS}), particle injection locations, and heavy-ion particle LET in producing the observed SEGR. Our data and simulation results provide evidence supporting the idea that both radiation-induced SBD and HBD are associated with defect-related conduction paths formed across the dielectric, in response to radiation-induced charge injection.

3.1 Experimental Detail

Heavy-ion radiation experiments were carried out in the Radiation Effect Facility at the Texas A&M University (TAMU) Cyclotron Institute. All experiments were done in air with an air gap of 3 cm and the beam was delivered with a high degree of uniformity (ranging

Table 3.1: Characteristics of heavy ions in Si.

Ion Type	Energy [MeV]	Min LET(Si)[a] [MeV·cm^2/mg]	Max LET(Si)[b] [MeV·cm^2/mg]	Range(Si)[b] [μm]
Ne	300	2.7	9.0	8.4
Ar	599	8.2	18.7	13.5
Cu	944	18.9	34.0	22.7

[a] LET after 3 cm air gap without degrader.

[b] LET/Range at Bragg Peak.

from 88% to 95%) over a 2.54 cm diameter circular cross-sectional area. Only one device was irradiated during each run. The characteristics of the heavy ions used in the experiments were calculated in SEUSS and SRIM [42], and are listed in Table 3.1 and Table 3.2. Three different ions were used including 300-MeV Ne, 599-MeV Ar, and 944-MeV Cu covering a linear energy transfer (LET) range from 3 MeV·cm^2/mg to 30 MeV·cm^2/mg (Si). All ion ranges were long enough that the Bragg peak was well away from the sensitive active regions such that the LET in those regions was well-defined. An aluminum degrader was used to vary ion LET. The difference between LET (Si) and LET (GaN) is relatively small. To align with most literature on silicon devices and heavy ion charts and tables at heavy ion facilities, LET in silicon: LET (Si) is used throughout the text. However, the TCAD simulations were correctly scaled for LET in GaN (detailed information in Appendix 6). Heavy ion flux ranged from 1×10^3 ion/cm^2·s to 1.5×10^5 ion/cm^2·s. A transistor-transistor-logic (TTL) signal enabled real-time total effective fluence monitoring. The heavy-ion beam was perpendicular to the DUT surface in all experiments.

Unlike X-ray photons, heavy ions cannot penetrate the packaging material on top of the die. Thus, for heavy-ion irradiation experiments, there are two common ways to prepare the device-under-test (DUT) including: 1) remove the plastic mold compound via the decapping process (detailed procedures are presented in Appendix 6), and 2) directly package die into open top packages. Compared with the decapping process, the custom package solution is faster and does not induce extrinsic damage to devices. Thus, two wafers of the commercially available D-mode GaN HEMTs were singulated and packaged in open-top 56-pin ceramic

Table 3.2: Characteristics of heavy ions in GaN.

Ion Type	Energy [MeV]	Min LET(GaN)[a] [MeV·cm^2/mg]	Max LET(GaN)[b] [MeV·cm^2/mg]	Range(GaN)[b] [μm]
Ne	300	1.5	7.1	6.0
Ar	599	4.5	14.7	8.2
Cu	944	10.4	25.7	14.1

[a] LET after 3 cm air gap without degrader.

[b] LET/Range at Bragg Peak.

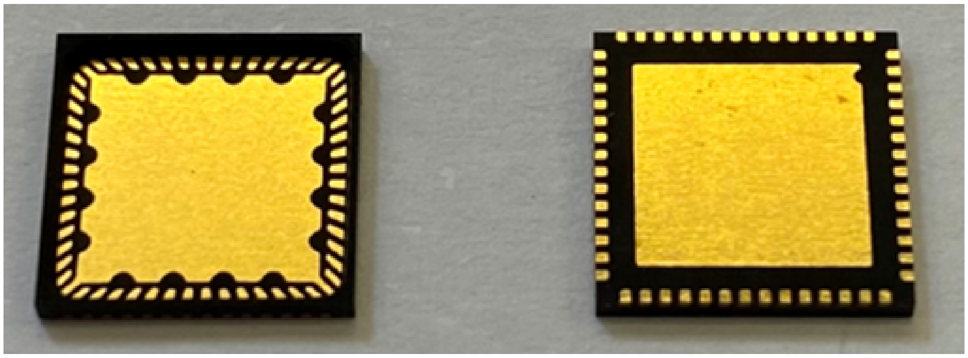

Figure 3.1: A picture of the open-top 56-pin ceramic quad flat no-lead package. Left is the front side (a), and right is the backside (b). With a big enough package cavity and 56 pins, most commercially available GaN HEMT bare dies can be packaged in it.

quad flat no-lead packages, as shown in Fig. 3.1. An open-top socket for a 56-pin QFN package allowed the heavy-ion beam to reach the die surface, as shown in Fig. 3.2.

A schematic of the heavy-ion testing system is shown in Fig. 3.3, which consists of a three-channel switching board and a motherboard. Fig. 3.4 shows a picture of the heavy-ion testing system. The three-channel switching board has three 3×3 reed relay matrices and each matrix has a corresponding multiplexer for switching among 9 relays, which is powered by a Keithley 2231A-30-3. An NI myRIO, a reconfigurable I/O (RIO) device, is used to control the whole switching board. Three NI PXIe-4135 single-channel source measurement units (SMUs) are used for supplying bias voltages (gate, drain, and source). Customized open-top sockets for a 56-pin QFN package are installed on socket adaptor boards, which

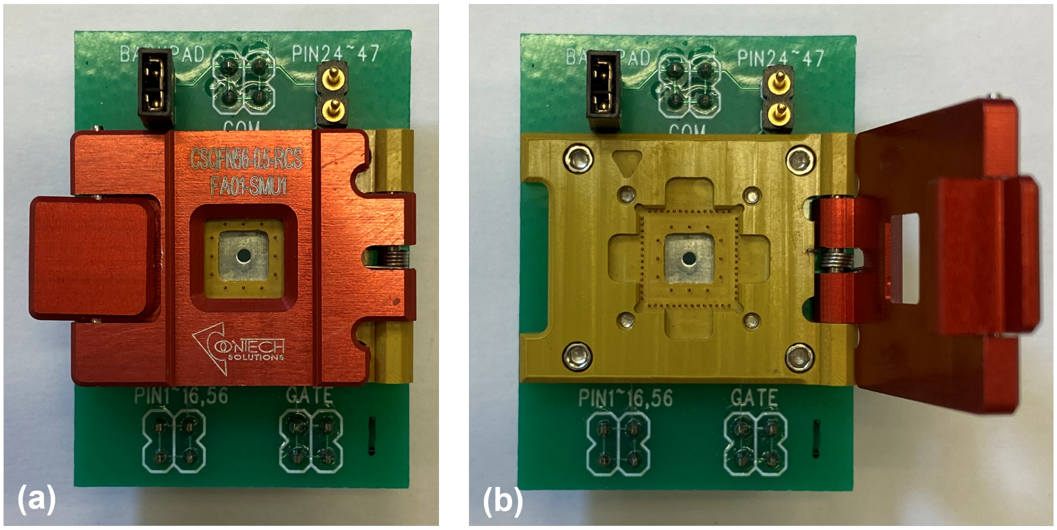

Figure 3.2: Pictures of the open-top socket for 56-pin QFN package installed on a socket adaptor board. (a) shows the cavity on top of the socket, which allows the heavy-ion beam to penetrate the active device layers. Pogo pins (spring-loaded pins) in (b) enable electrical contact from the QFN packages to the PCB boards.

are then plugged into the motherboard via pin-head connectors. Note that, with different socket adaptor boards, this system is compatible with various types of GaN HEMTs. The maximum operating voltage is 250 V and the corresponding parasitic resistance is around 2 Ω. For higher drain voltage stress measurements (V_{DS}>250 V), a high voltage testing board with a single socket on top was used, with the drain voltage supplied by a Keithley 2410, which had an 1100 V maximum voltage output, 1 A current output and 20 W power output.

The in-air station provided by the facility has a target positioning system allowing for the positioning of the target in four directions (x, y, z and θ). With this system, we were able to switch the beam from device to device remotely, which significantly improved our experimental efficiency. During each experiment, the switching board ensured that only the selected DUT was biased (V_{GS} and V_{DS}) under radiation. A gate voltage of -14 V was continuously applied to keep the depletion-mode HEMT in the off-state, or blocking condition, so that the drain region electric field was maximized. This is considered to be the worst-case condition for SEGR, which will be discussed in the following section. Gate current (I_G), drain current (I_D), and source current (I_S) were monitored in real time throughout the

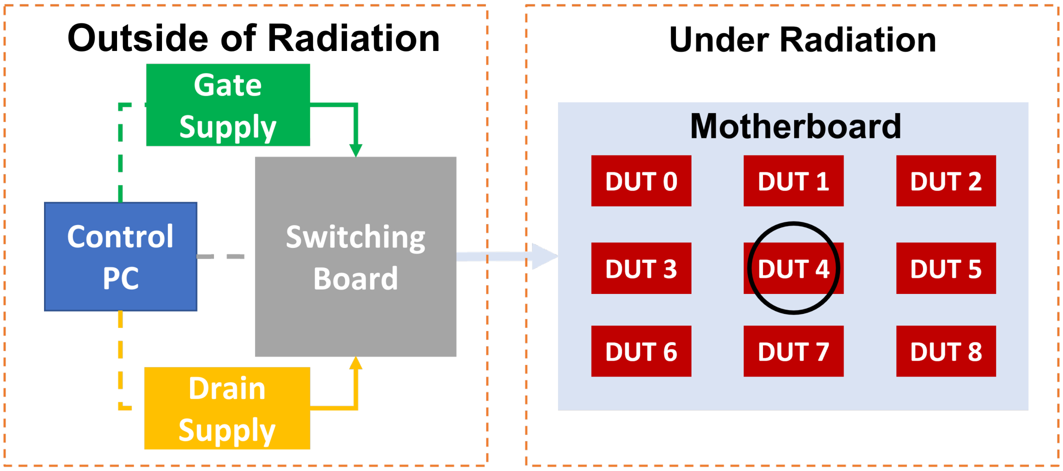

Figure 3.3: Schematic of the heavy-ion testing system. Relay matrices on the switching board provide biases to the single DUT under the beam. The whole system is controlled by an embedded controller via a LabVIEW program. The black circle represents the heavy-ion beam aperture.

experiments. Characterization measurements including IV sweep (I_D vs. V_{GS}), capacitance measurements, and DC testing were carried out before and after radiation.

A total of 148 devices were tested in our experiments. Drain voltages ranged from 0 to the maximum operation drain voltage of 600V. We used two types of experiments to investigate the heavy-ion tolerance of AlGAN/GaN HEMTs:

- Constant fluence experiments, where devices were radiated with a constant effective fluence (e.g., 10^6 ion/cm^2), while under different combinations of V_{DS}, LET, and flux.

- Fluence to failure experiments, where devices were continuously irradiated until the off-state leakage current (I_D and I_G) reached compliance limits or a breakdown event was observed (radiation-induced SBD or HBD). Various combinations of V_{DS}, LET, and flux were used.

In order to account for device-to-device variation, for most experimental conditions a minimum of 3 samples were tested. Most experiments were carried out with moderate LET and V_{DS}. This study focused on the impact of four major parameters that affect radiation-induced dielectric degradation: V_{GS}, V_{DS}, incident ion LET, and ion flux.

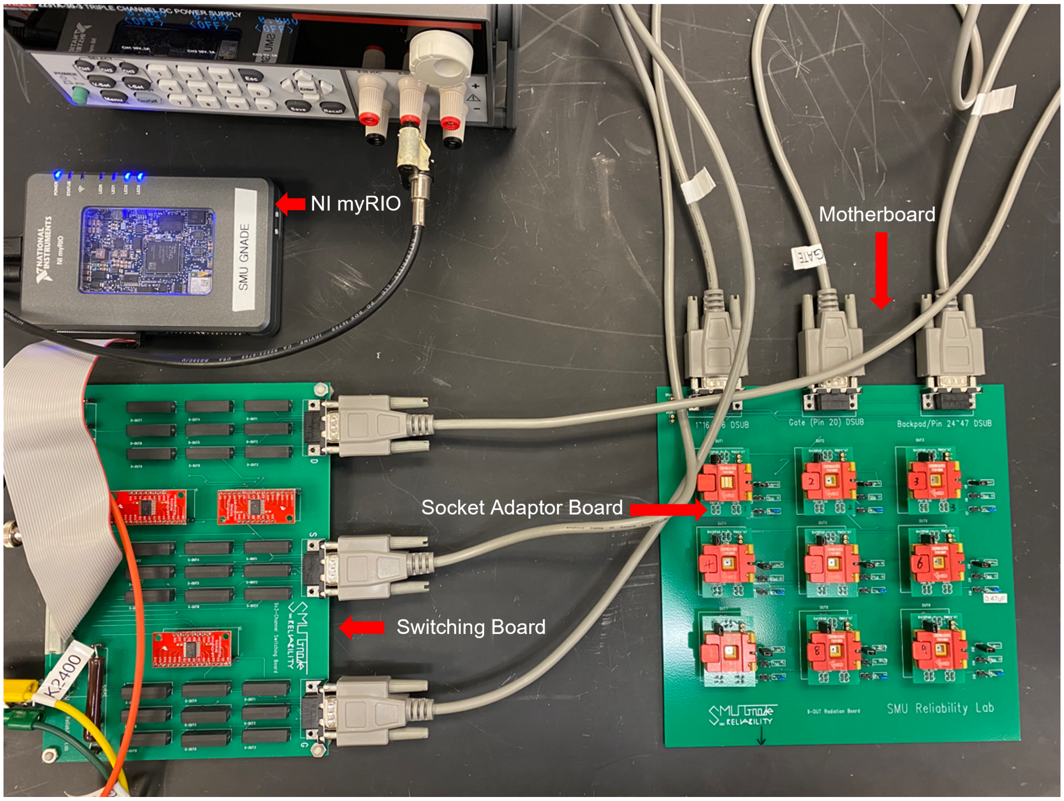

Figure 3.4: A picture of the heavy-ion testing system. The three-channel switching board is controlled by a NI myRIO and powered by a Keithley 2231A-30-3. Nine sockets are plugged into the motherboard. The parasitic resistance of the whole system is approximately 2 Ω. Maximum operational voltage is 250 V.

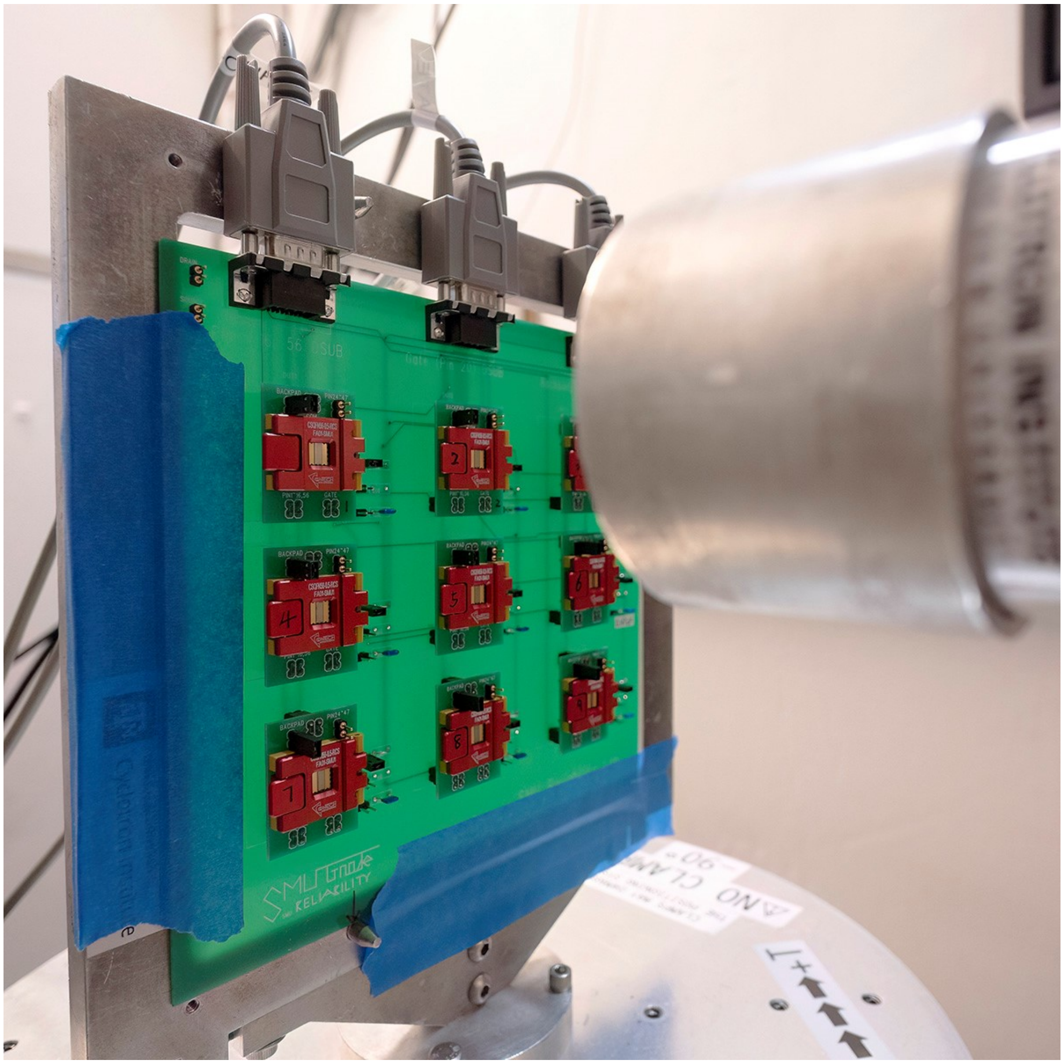

Figure 3.5: A picture of the DUT board mounted on the in-air station provided by TAMU Cyclotron Institute. The distance between the irradiated DUT and the heavy-ion beam window is 3 cm (in this photo the board has not been moved into position yet so the air gap is much larger). The clearance between each open-top socket ensures only the selected DUT is irradiated.

3.2 Experimental Results

3.2.1 Multistage Degradation Process

The main failure mode observed under irradiation was increased leakage current from drain to gate, implying heavy-ion-induced events causing permanent gate dielectric degradation. Of 148 total DUTs tested, only 5 DUTs experienced an increase in source-to-gate leakage under radiation. The low fraction of source-to-gate breakdowns has been attributed to reduced charge collection efficiency around the source-gate region. The change in the gate current as a function of fluence for a typical breakdown event is shown in Fig. 3.6. The stepwise increase in gate leakage implies a multistage degradation process. Each abrupt gate current increase (with corresponding drain current increase) represents a soft breakdown, which is the dominant progression initially. Ultimately, usually after several SBD events, the gate current undergoes a final HBD event evidenced by a gate leakage limited only by the compliance of the voltage source.

A decrease in the leakage current over time can be observed after the soft breakdown, as shown in Fig. 3.7, implying charge redistribution and trap filling. The post-irradiation gate leakage current compensates a fraction of the accumulated charges at the defect sites and reduces electrical stress. One might argue that a simple RC discharge can also induce a similar current decrease. However, if we assume the resistance of the leakage path is 1.7×10^7 Ω and the RC constant time is around 25 seconds (estimated from Fig. 3.7), then the capacitance should be at least 1.5 μF, which is several orders of magnitude higher than the device capacitance we measured in the off-state. Hence, we believe the trapped charges (mainly holes) above the 2DEG channel play an important role in this dynamic gate leakage recovery phenomenon.

On the other hand, hard breakdown (a short circuit between gate and drain) usually happens at higher effective fluence, which could be the result of precursor damage (due to irradiation and electrical stress). During the experiments, only a very limited number of devices (less than 10%) experienced hard breakdown without having any soft breakdown. The fraction of samples that showed a sudden HBD without the usual progression of SBDs likely had a higher level of intrinsic gate defects rendering them more prone to breakdown.

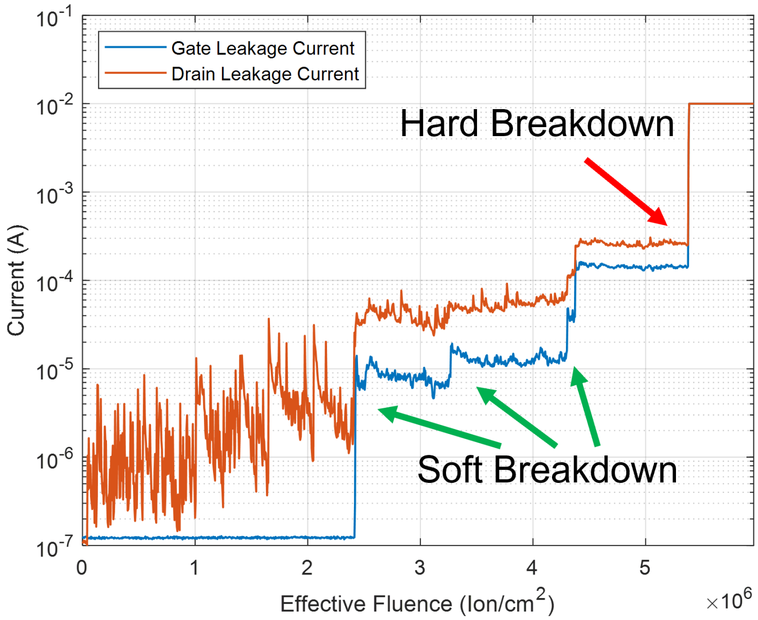

Figure 3.6: A typical multistage degradation process under 599-MeV Ar heavy-ion radiation with LET equal to 15 MeV·cm^2/mg (Si). V_{GS} equals -14 V, and V_{DS} equals 100 V. Flux rate is 10^5 ion/cm^2·s, and total effective fluence is 5.95×10^6 ion/cm^2. Current compliance is 0.1 A. Multiple soft breakdowns occurred before the hard breakdown.

3.2.2 Voltage Dependence

Both gate voltage and drain voltage play important roles in dielectric degradation under heavy-ion radiation. As we mentioned before, off-state is the worst case for SEGR, in which the dielectric and the AlGaN interface under the gate can collect a significant amount of transient ion-induced charge. Fig. 3.8 shows dielectric degradation results with different gate voltages under 599-MeV Ar radiation (LET=15 MeV·cm^2/mg (Si)), where error bars represent the 95% confidence level. This is based on the results from 11 measurements including nine DUTs under off-state (V_{GS}=-14 V) and two DUTs under subthreshold-state (V_{GS}=-10 V) with the same conditions (V_{DS}=150 V). A key finding was that no significant degradation was observed for devices in subthreshold up to 1.25×10^7 ion/cm^2. By comparison, off-state devices experienced multiple soft breakdowns.

With the 2DEG channel partially depleted, part of the excess charge generated by heavy ions will be swept away before getting collected at the dielectric/AlGaN interface. In other

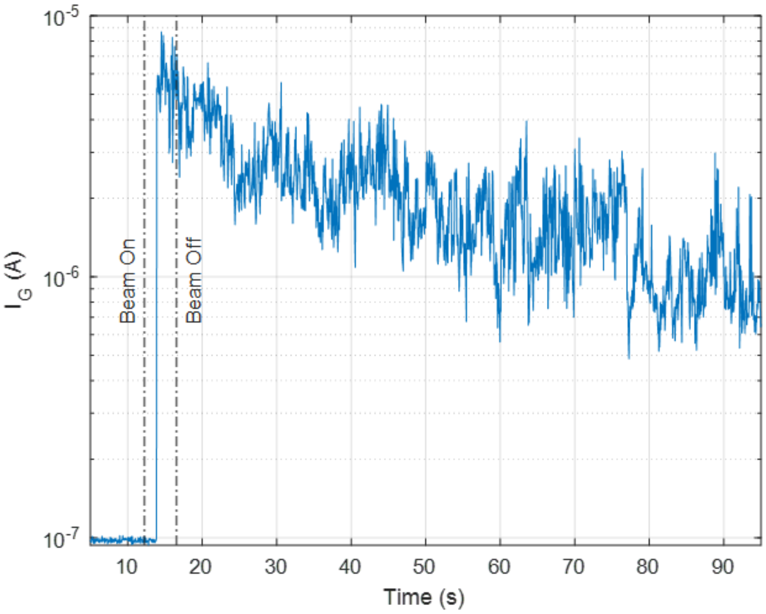

Figure 3.7: An example of gate leakage current changing after radiation-induced SBD. 599-MeV Ar heavy-ion radiation with LET equal to 15 MeV·cm^2/mg (Si) was used, with V_{GS}=-14 V, V_{DS}=150 V, and flux of 1.2×10^5 ion/cm^2·s. The two dashed lines represent the radiation-on time and radiation-off time. The gradually decreasing leakage current could be induced by charge redistribution, trap filling, and interface charge release.

words, off-state has more charge (hole) accumulation under the dielectric compared with subthreshold-state under radiation, which will produce a stronger electric field transient inside the device. Further, hole accumulation at the dielectric interface is also related to dielectric defect (trapped charge) creation via mechanisms like anode-hole injection, as demonstrated in [36], [43].

To study the effects of drain voltage on SEGR, fluence to failure experiments with two different drain voltages were carried out. 599-MeV Ar ion radiation was continuously applied with flux equal to 1.2×10^5 ion/cm^2·s, and LET of 15 MeV·cm^2/mg (Si), until the first breakdown event occurred (radiation-induced SBD or HBD). The corresponding effective fluence is defined as critical fluence F_{crit}. Results are shown in Table 3.3. Notice that, each condition had one device experiencing radiation-induced HBD.

The mean critical fluence F_{crit} for 100V is three times larger than that for 150V V_{DS}, which

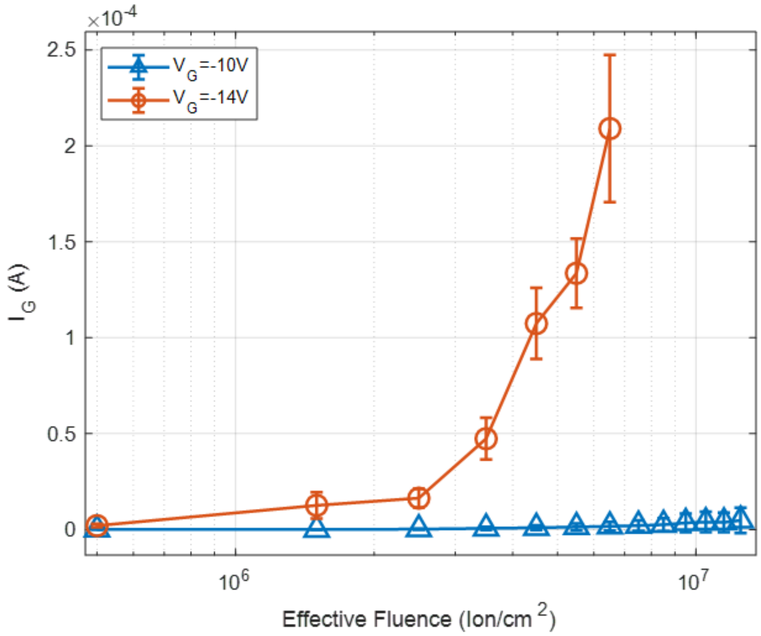

Figure 3.8: Gate leakage current vs. effective fluence under subthreshold-state (V_{GS}=-10 V) and off-state (V_{GS}=-14 V). 599-MeV Ar is used with flux equal to 1.5×10^5 ion/cm^2·s. LET equal to 15 MeV·cm^2/mg (Si), and V_{DS} equal to 150V. Total effective fluence is 1.25×10^7 ion/cm^2. Error bars represent the 95% confidence level. Significant SEGR response differences can be observed under two gate biases.

is due to reduced charge collection at the dielectric/AlGaN interface. Similar experiments were carried out with the same drain bias, ion type, LET, and slightly different flux (1×10^5 ion/cm^2·s). Instead of stopping the radiation when the first breakdown process happened, radiation was continuously applied until the gate leakage current reached the compliance level of 10 mA (final radiation-induced HBD event). The corresponding effective fluence is called failure fluence F_{fail}. Results are given in Table 3.4. Overall, our data demonstrate that higher drain voltages have lower critical fluence and failure fluence. In other words, operation at higher voltage limits the lifetime of the devices in a heavy-ion radiation field.

To further investigate the voltage effect on dielectric degradation, we performed the same experiments with V_{DS}=0 V, V_{GS}=-14 V (same LET and flux). No significant gate degradation was observed up to a total fluence of 2.5×10^7 ion/cm^2, indicating charge collection at the dielectric/AlGaN interface is the dominant factor in heavy-ion-induced SEGR. Without

Table 3.3: Results of critical fluence experiments with two different drain voltages (V_{GS}=-14 V, LET=15 MeV·cm^2/mg (Si), flux=1.2×10^5 ion/cm^2·s).

V_{DS}	Mean F^{a}_{crit}	SD F^{a}_{crit}	Sample Number	HBD Number
100 V	3.3×10^6	1.9×10^6	4	1
150 V	1.1×10^6	6.3×10^5	11	1

^{a}Unit is ion/cm^2.

Table 3.4: Results of failure fluence experiments with two different drain voltages (V_{GS}=-14 V, LET=15 MeV·cm^2/mg (Si), flux=1×10^5 ion/cm^2·s). Radiation was continuously applied until the gate leakage current reached the compliance 10 mA.

V_{DS}	Mean F^{a}_{fail}	SD F^{a}_{fail}	Sample Number
100 V	5.9×10^6	6.9×10^5	2
150 V	3.1×10^6	8.9×10^5	2

^{a}Unit is ion/cm^2.

the strong external electric field, most of the heavy-ion-induced charges will recombine in a short period, thus minimizing the peak transient electric field across the dielectric, reducing the amount of charge collected by the defects/traps at the dielectric/AlGaN interface. The characterization measurement results are given in Table 3.5. The threshold voltage shifts 0.4 V in the negative direction, which is the result of trapped holes above the 2DEG channel. Hole trapping is the dominant charge trapping mechanism observed in heavy-ion irradiation experiments, due to the negative gate bias. Further, heavy-ion-induced defects inside the dielectric may also be closely related to the electric field strength.

3.2.3 LET and Flux Dependence

Constant fluence experiments were used to determine the heavy-ion LET effects on the dielectric degradation process. Devices were biased under a constant drain voltage (starting

Table 3.5: Results of off-state zero-drain-voltage experiments (V_{GS}=-14 V, LET=15 MeV·cm^2/mg (Si), flux=1×10^5 ion/cm^2·s).

Condition	Mean Drain Current[a]	Mean Gate Current[a]	V_{th}
Pre Rad	2.3×10^{-7} A	1.1×10^{-7} A	-9.2 V
Post Rad	1.7×10^{-6} A	7.2×10^{-7} A	-9.6 V

[a] DC testing condition V_{GS} =-14 V, V_{DS} =100 V.

from 150 V) and the effective total fluence was set to 1×10^6 ion/cm^2. After each run, V_{DS} was ramped up by 25 V until reaching 200 V. LET varied from 10 to 18 MeV·cm^2/mg (Si). The corresponding results are shown in Fig. 3.9 and Fig. 3.10, in which each point represents the mean off-state gate current after heavy-ion irradiation. Error bars are the 95% confidence level. Notice that, abnormal data induced by early failures, attributed to higher as-processed defect concentrations, have been removed from the analysis (less than 10% of the total number of DUTs).

Apparently, under the same V_{DS}, the gate leakage current increases with increasing particle LET. Since the dielectric breakdown path acts like a linear resistor (relatively stable leakage current under constant bias), we can calculate the equivalent resistance of the breakdown path R_G to eliminate the simple Ohmic effect. As shown in Fig. 3.11 R_G decreases with increasing LET, suggesting higher defect density or different defect types inside the breakdown path. In other words, the LET dependence we observed is related to the fact that a heavy ion with a higher LET value can generate more electron-hole pairs along its track, which will induce a stronger electric field transient and generate more defects inside the dielectric, resulting in a higher gate leakage current.

We also studied the flux effect on SEGR, and three flux values were used, including 10^3 ion/cm^2·s, 10^4 ion/cm^2·s, and 10^5 ion/cm^2·s (V_{GS}=-14 V, V_{DS}=100 V, LET=15 MeV·cm^2/mg (Si)). For flux=10^3 ion/cm^2·s, only one sample was tested because of limited experimental beam time. Note that, the heavy-ion flux is an average number, and the actual value varies statistically during each experiment. As shown in Fig. 3.12, off-state gate leakage

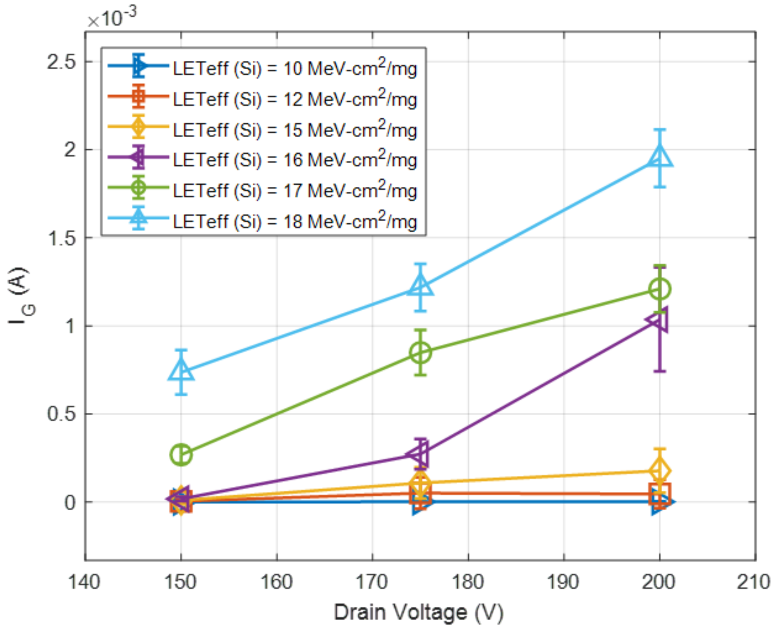

Figure 3.9: Drain voltage vs. gate current under off-state (V_{GS}=-14 V). 599-MeV Ar is used with flux equal to 1×10^5 ion/cm^2·s. LET was varied from 10 to 18 MeV·cm^2/mg (Si) using a degrader. Total effective fluence is 1×10^6 ion/cm^2 for each run. Error bars represent the 95% confidence level.

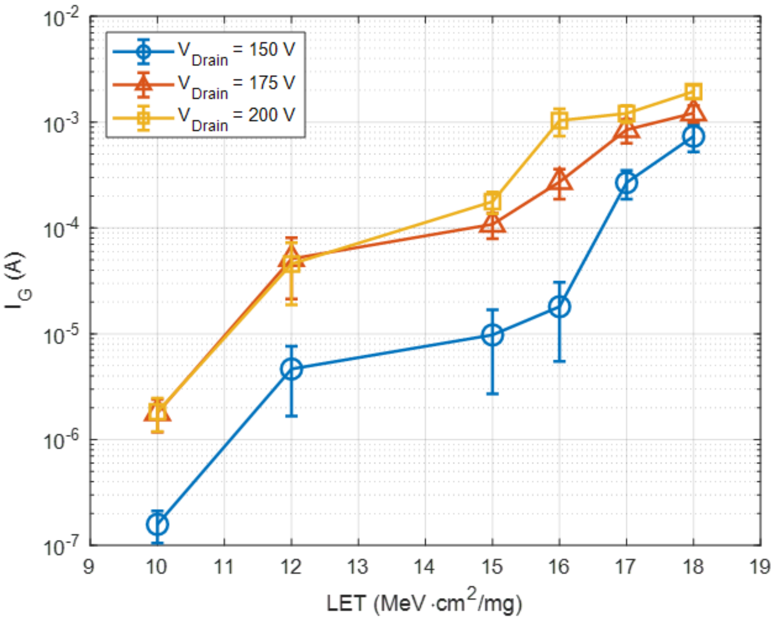

Figure 3.10: Particle LET vs. gate current under off-state (V_{GS}=-14 V). 599-MeV Ar is used with flux equal to 1×10^5 ion/cm^2·s. LET was varied from 10 to 18 MeV·cm^2/mg (Si) using a degrader. Total effective fluence is 1×10^6 ion/cm^2 for each run. Error bars represent the 95% confidence level. Off-state gate leakage current is proportional to particle LET.

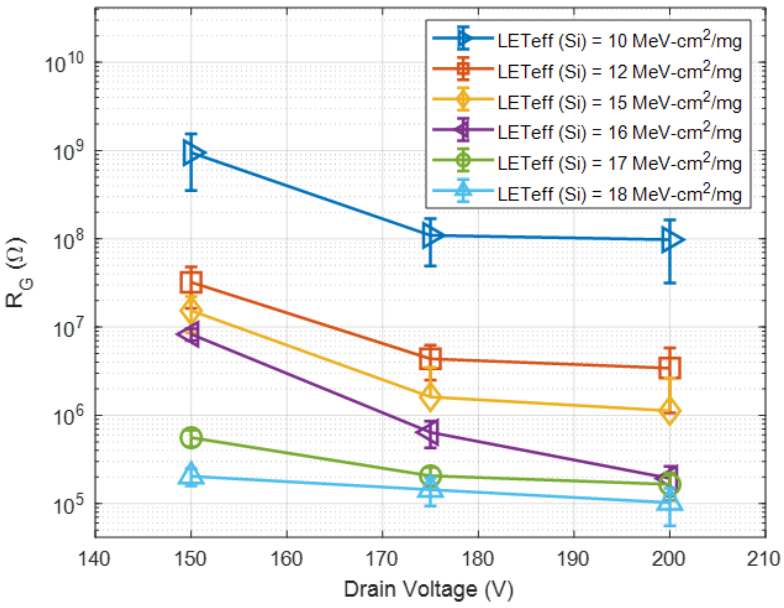

Figure 3.11: Drain Voltage vs. relative gate resistance under off-state (V_{GS}=-14 V). 599-MeV Ar is used with flux equal to 1×10^5 ion/cm^2·s. LET was varied from 10 to 18 MeV·cm^2/mg (Si) using a degrader. Total effective fluence is 1×10^6 ion/cm^2 for each run. Error bars represent the 95% confidence level.

currents were on a similar level before total fluence reaching 5×10^6 ion/cm^2, especially for 10^3 ion/cm^2·s and 10^4 ion/cm^2·s. However, for total fluence above 5×10^6 ion/cm^2, there is a significant difference between 10^4 ion/cm^2·s and 10^5 ion/cm^2·s, which could be the result of enhanced charge collection under the dielectric. Also, if we consider the lifetime of the defects or trapped charges, a higher flux represents a higher chance to generate enough defects to trigger a breakdown process.

In general, particles with higher LET require a lower electric field to initiate the breakdown process, and under the same electric field stress, particles with higher LET can induce larger gate leakage currents (same total fluence). A higher radiation flux will induce a higher gate leakage current due to an increased charge injection rate. The more heavy-ion-induced charges (holes) collected by the dielectric/AlGaN interface, the stronger the electric field transient will be, which in turn can generate more defects inside the dielectric.

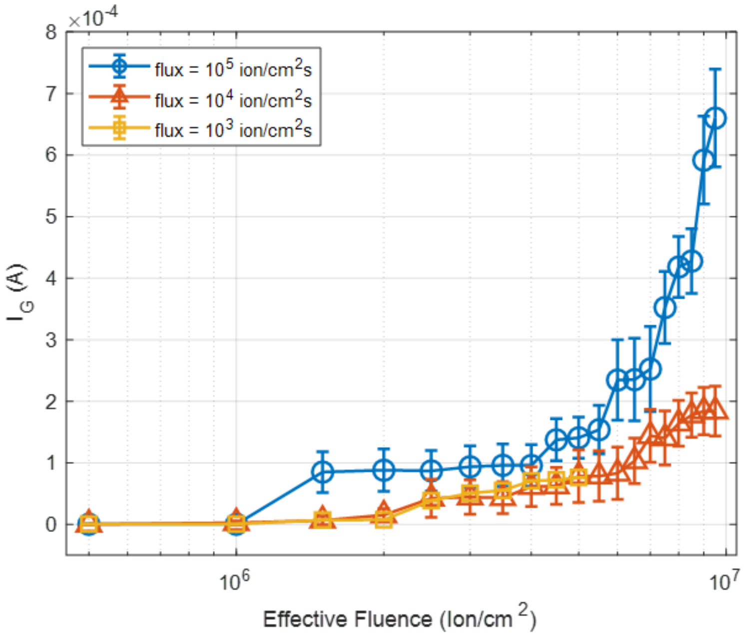

Figure 3.12: Effective fluence vs. gate current under off-state (V_{GS}=-14 V, V_{DS}=100 V) with 599-MeV Ar ion (LET=15 MeV·cm^2/mg (Si)). Error bars represent the 95% confidence level. For flux=10^3 ion/cm^2·s, only one sample was tested because of limited experimental beam time. A higher radiant flux results in a larger gate leakage current.

3.2.4 Critical Injection Level Experiment

During the irradiation experiments, the GaN HEMTs are in the off-state with high applied drain-to-source voltage, so the dielectric and the AlGaN interface under the gate can collect a significant amount of transient ion-induced charge. We postulate that radiation-induced SBD and HBD events could be precipitated in the gate dielectric when transient charge injection produces a high peak transient vertical electric field, E_{peak}, with a significant transient duration, t_{peak} [44]. In general, when the instantaneous electric field reaches or exceeds the breakdown field, E_{BD}, of the dielectric for a sufficient duration, SEGR will be triggered (analogous to electric-field or voltage-driven time-dependent dielectric breakdown). In our case, radiation-induced transient hole charge collection at the dielectric/AlGaN interface due to the negative gate bias is hypothesized to be the main cause of the dielectric degradation and SEGR (note that the lateral electric field induced by V_{DS} is orders of magnitude weaker than the vertical field).

To further prove this hypothesis, critical injection level experiments were designed and carried out at the TAMU Cyclotron Institute, in which the 2DEG channel is partially turned on and maintains constant current conduction under heavy-ion radiation. The device is very sensitive to gate voltage V_{GS} in the subthreshold region, as shown in Fig. 2.3. In other words, a tiny change in the gate voltage will result in a significant change in I_{DS}. Thus, instead of controlling gate voltage, the SMU connected to the source works as a current sink (current source mode) and maintained a constant current level injected through the 2DEG channel under heavy-ion radiation. The source voltage V_S changes dynamically according to I_S, but the overall variation is small ($|\Delta V_S| \leq 6$ V) in terms of V_{DS}. Therefore, we assume V_{DS} as a constant value throughout the whole experiment.

A total of six injection levels were used in critical injection level experiments, including 0 A, 1 μA, 10 μA, 100 μA, 1 mA, and 10 mA. At least 3 DUTs were tested under each injection level (21 DUTs were tested in total). Constant fluence experiments were carried out with 599-MeV Ar (fluence=1×10^7 ion/cm^2, flux=1×10^5 ion/cm^2·s, LET=10 MeV·cm^2/mg (Si)) V_G=-14 V and V_{DS}=150 V. Table 3.6 shows the critical fluence of each injection level and its corresponding standard deviation. Only under 0 A and 1 μA conditions, radiation-induced HBDs were observed, indicating HBD requires a stronger electric field transient to be triggered than SBD. Basically, a higher current injection level has a higher corresponding critical fluence F_{crit}, because of reduced charge collection efficiency. With the 10 mA injection level, no degradation on the gate dielectric was observed, which is due to most heavy-ion-induced charges being swept away via the 2DEG channel.

Fig. 3.13 shows the mean off-state gate leakage current versus total effective fluence, where error bars represent the 95% confidence level. Note that, abnormal data induced by early failures, which are attributed to higher as-processed defect concentrations, have been removed from the analysis (less than 10% of the total number of DUTs). Detailed experimental data plots are presented in Appendix 6. Apparently, the current injection level has a significant impact on the heavy-ion-induced dielectric degradation process. However, injection levels below 1 mA have little effect on the off-state leakage current (effective fluence above 5×10^6 ion/cm^2), which may be due to the fact that the current level is too low to remove most of the heavy-ion-induced charges before being collected by the dielectric/AlGaN

Table 3.6: Results of critical fluence experiments with different injection levels (V_{GS}=-14 V, LET=15 MeV·cm^2/mg (Si), flux=1.2×10^5 ion/cm^2·s).

I_S	Mean F^{a}_{crit}	SD F^{a}_{crit}	Sample Number	HBD Number
0 A	1.2×10^6	7.5×10^5	3	1
1 μA	2.4×10^6	7.5×10^5	4	1
10 μA	2.5×10^6	4.9×10^5	3	0
100 μA	2.3×10^6	4.1×10^5	5	0
1 mA	4.5×10^6	1.3×10^6	3	0
10 mA	NA	NA	3	0

[a] Unit is ion/cm^2.

interface. With a 10 mA current constantly conducted through the 2DEG channel, the gate dielectric was well protected from heavy-ion radiation (LET=10 MeV·cm^2/mg (Si)).

In general, with a higher injection level, fewer charges (holes) will be collected by the dielectric/AlGaN interface, resulting in a significantly weaker electric field transient inside the device and less damage to the dielectric, which is consistent with our heavy-ion-induced gate dielectric degradation hypothesis.

3.2.5 Experimental Data Summary

Fig. 3.14 shows a summary of the experimental data. Each point is the result of a corresponding constant fluence experiment with V_{GS}=-14 V, flux=10^5 ion/cm^2·s and effective fluence equals 1×10^6 ion/cm^2. As expected, with higher V_{DS} and particle LETs, the D-mode GaN HEMTs have a much higher chance to experience a breakdown event. Radiation-induced HBD typically occurred at conditions of high V_{DS} and LET. In other words, F_{crit} and F_{fail} are proportional to particle LET and V_{DS}. The overlapping data points are due to device-to-device variations.

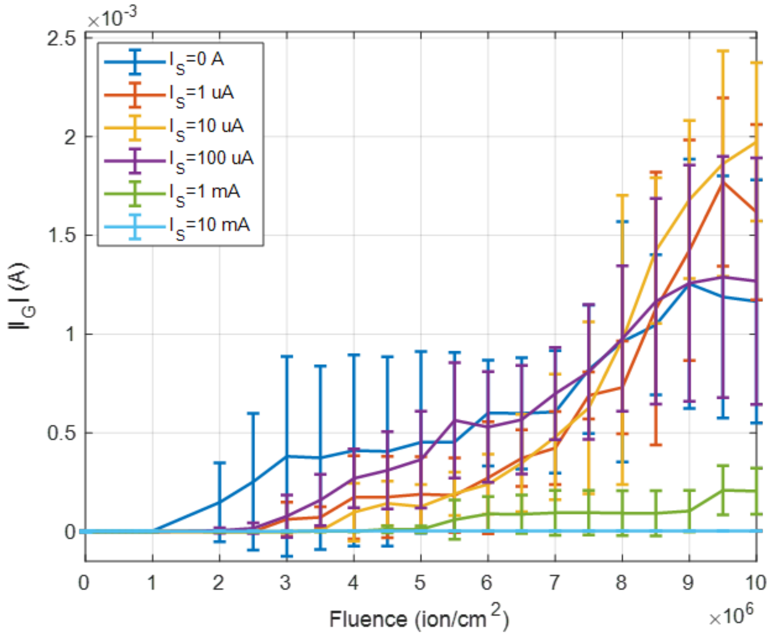

Figure 3.13: Effective fluence vs. gate current under off-state (V_{GS}=-14 V, V_{DS}=150 V) with different current injection levels. 599-MeV Ar (LET=10 MeV·cm^2/mg (Si)) is used with flux equal to 1×10^5 ion/cm^2·s. Total effective fluence is 1×10^7 ion/cm^2 for each run. Error bars represent the 95% confidence level. A higher injection level results in a lower off-state gate leakage current.

3.2.6 Charge Accumulation and Defect Generation

Threshold voltage V_{th} shift has been observed, which is a combined effect of charges trapped in both the dielectric and the interface. To further understand the radiation-induced charge trapping and interface states, characterization measurements pre and post-radiation have been carried out on our samples. Unfortunately, most of our post-radiation samples experienced high drain-gate leakage (multiple radiation-induced SBDs or HBDs), making it hard for us to perform high-frequency capacitance measurements. Fig. 3.15 shows the normalized high-frequency capacitance measurement results of 5 post-radiation samples with moderate gate leakage, which were irradiated under 599-MeV Ar ion (LET=15 MeV·cm^2/mg (Si)) with flux of 10^4 ion/cm^2·s and effective fluence equal to 1×10^7 ion/cm^2. The drain voltage is set to 100 V and the gate voltage is -14 V. From the plot, we can observe midgap voltage V_{mg} shifts around 0.48V and flat-band voltage V_{fb} shifts around 0.48V respectively,

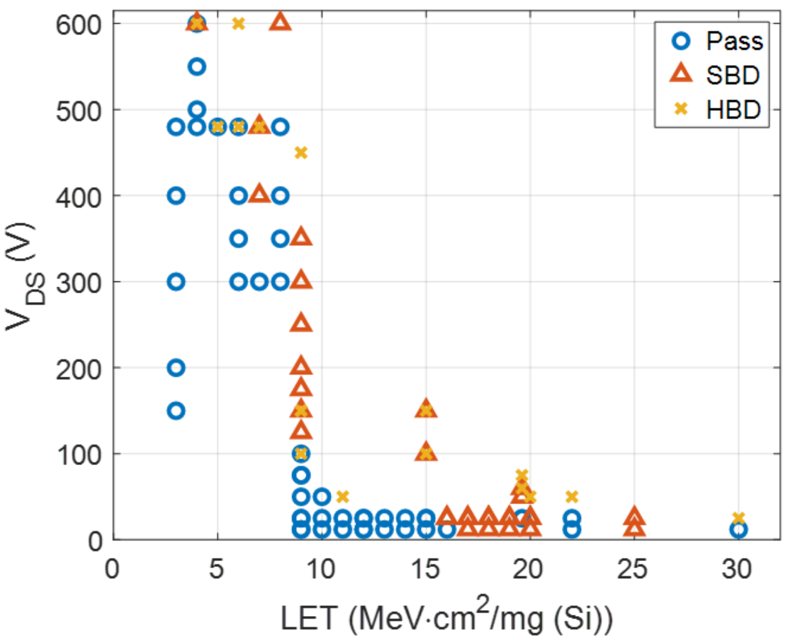

Figure 3.14: Summary of the heavy-ion irradiation experimental results. Each data point represents a constant fluence experiment with V_{GS}=-14 V, flux=10^5 ion/cm^2·s and effective fluence equals 1×10^6 ion/cm^2. Overlapping points are due to device-to-device variations. F_{crit} and F_{fail} are proportional to particle LET and V_{DS}.

indicating positive charge trapped inside the gate dielectric, which can be used to estimate heavy-ion induced net dielectric charge density, ΔN_{dt}, by the following equation [45], [46]:

$$\Delta N_{dt} = -\frac{C_{Dielectr}\Delta V_{mg}}{qA} \tag{3.1}$$

where $C_{Dielectr}$ is the dielectric capacitance, $-q$ is the electronic charge, and A is the gate area. Note that we are assuming all interface traps are neutral when the Fermi energy is at midgap [47]. Similarly, the radiation-induced interface trapped charge density, ΔN_{it}, can be estimated by [45], [46]:

$$\Delta N_{it} = \frac{C_{Dielectr}(\Delta V_{fb} - \Delta V_{mg})}{qA} \tag{3.2}$$

Based on the values we mentioned before, we find that the interface trapped charge

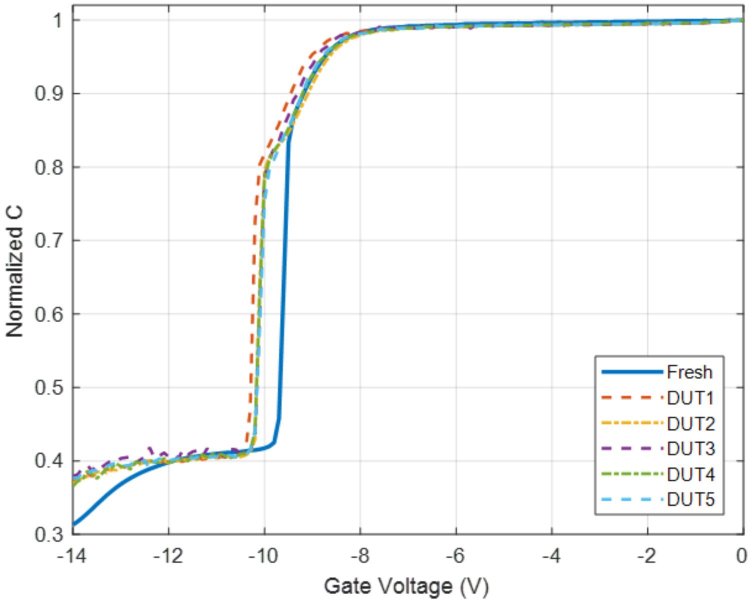

Figure 3.15: Normalized high-frequency capacitance measurements before and after radiation. The solid blue line is a typical $C-V$ curve of our samples. DUT1-5 are the post-radiation samples, which were irradiated under 599-MeV Ar ion with flux=10^4 ion/cm^2·s, effective fluence=1×10^7 ion/cm^2, V_{DS}=100 V, V_{GS}=-14 V.

build-up is too small to be measured, which could be due to the large pre-radiation interface trapped charge density. Similar results were reported by authors in [48]. However, it doesn't mean interface states are unrelated to radiation-induced dielectric degradation. Moreover, in [49] the authors demonstrated that interface states with relatively shallow donor states and very deep acceptor states (in our case relatively shallow donor states) made it possible that the states are fully ionized throughout the studied gate bias range, which would also generate a CV shift as shown in Fig. 3.15. Under such circumstances, the interface states have a high density and are indistinguishable from a fixed charge [49]. They also argued that capacitance measurements under different temperatures were necessary to estimate the interface states. We believe both charges trapped inside the dielectric and at the interface between the dielectric and AlGaN layer are directly related to CV curve shifting and dielectric breakdown.

In general, the fact that five devices experienced similar midgap voltage (flat-band voltage) shift after being exposed to the same amount of heavy-ion radiation indicates heavy-ion induced charge (hole) accumulation inside the dielectric, which also causes the threshold voltage V_{th} shift we mentioned before. Nitrogen vacancies are thought to be one of the main reasons for trapped holes in the nitride dielectric [50].

We also observed the 2DEG channel gradually turning on under heavy-ion radiation, as shown in Fig. 3.16. After several soft breakdowns, the main leakage path changes from I_{DG} to I_{DS}, suggesting partially depleted 2DEG channel recovery, which may also be due to trapped positive charges in the bulk and surface of the dielectric and AlGaN layer. This is the opposite process of a common failure in GaN HEMTs called current collapse, which has been referred to as an output current reduction caused by negative traps in the device structure [51]. In [51], the authors suggested that the negative charge on the AlGaN layer surface acted like a negatively biased metal gate, which would reduce the surface potential and deplete the 2DEG channel, leading to an extension of the gate depletion region, known as the virtual gate effect. In our case, the trapped positive charges in the bulk and surface of the dielectric and AlGaN layer, act as a positively biased gate, which will raise the surface potential and reduce the gate depletion region, as shown in Fig. 3.17. With a sufficient amount of trapped positive charges, the 2DEG will partially recover and start to conduct current. The output drain current is now controlled by the mechanism that supplies charge to, and removes charge from the virtual gate, in addition to the applied gate bias [51]. Therefore, after we turned off the beam, which was the main mechanism supplying the positive charge, the virtual gate effect gradually weakened and the 2DEG channel was slowly depleted as shown in Fig. 3.16. Moreover, we also observed that in most cases the virtual gate effect can prevent further fatal gate dielectric breakdown (radiation-induced SBD to HBD), which agrees with our sub-threshold state experimental data that reduced charge collection (by compensation by sub-threshold current injection) led to a reduction in defect generate rate.

3.3 Device Simulation Analysis

To further understand the device response to heavy-ion-induced charge transients, a 2D Silvaco Atlas TCAD model of the GaN HEMT structure was constructed and tuned against current-voltage parameters from real devices. The TCAD simulations were performed to

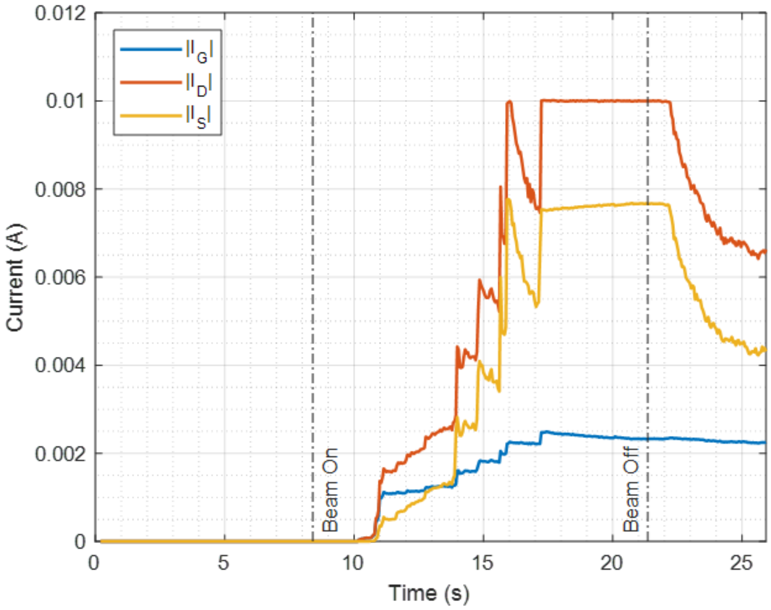

Figure 3.16: An example of a heavy-ion radiation-induced virtual gate effect. 599-MeV Ar heavy-ion radiation with LET equal to 18 MeV·cm^2/mg (Si) was used, with V_{GS}=-14 V, V_{DS}=200 V, and flux equals 2×10^5 ion/cm^2·s. The two dashed lines represent the radiation-on time and radiation-off time. After turning off the beam, the virtual gate effect gradually weakened.

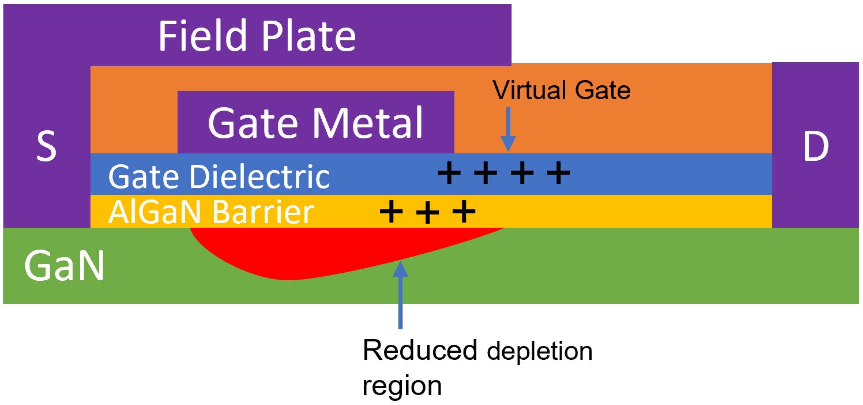

Figure 3.17: An illustration of positive virtual gate effect on a GaN HEMT. The plus sign represents trapped positive charges. Trapped holes diminish the gate depletion region.

elucidate the impact of four variables independently: Particle injection location, particle LET, HEMT drain-to-source voltage (V_{DS}), and HEMT gate-to-source voltage (V_{GS}). Three parameters were selected as primary metrics to evaluate heavy-ion particle-induced transients. The peak transient vertical electric field (E_{peak}) across the gate, the fraction of the gate length (F_{BD}) for which the peak field reached or exceeded the breakdown field of the dielectric (E_{BD}), and the duration of the event where $E \geq E_{BD}$, or t_{peak}. The assumption for any event is that the higher the peak transient electric field, the higher the fraction of the gate area that reaches or exceeds the breakdown strength, and the longer the duration of this transient, the more the dielectric is damaged. The breakdown field, E_{BD}, of the dielectric used in this type of D-mode GaN HEMTs is based on literature values [52], [53] and for the purposes of this evaluation has been assumed to be approximately 10 MV/cm. In these simulations, we found that the maximum E_{peak} generated by the injected particles were in the same range or exceeded the E_{BD}, and were thus likely to cause dielectric degradation that could lead to soft or hard breakdown events (SEGR).

3.3.1 Particle Injection Location Dependence

For each simulation run, one of five different heavy-ion particle injection locations (Loc1-Loc5 indicated by red arrows) was assumed along the channel (gate length is 4 μm), as shown in Fig. 3.18. For the analysis, nine equally spaced sensing probes (0 to 4 μm with 0.5 μm spacing) were placed along the gate dielectric for calculating the three transient parameter values (E_{peak}, F_{BD} and t_{peak}). The source-gate edge (Loc1) is at 0 μm and the drain-gate edge (Loc4) is at 4 μm. For each simulated ion event, an LET of 10 MeV·cm^2/mg (Si) was assumed (most heavy-ion experiments were carried out with an LET of 10). For these simulations, the HEMT device was biased in the off-state (V_{GS}=-14 V) and the drain-to-source voltage was 100 V.

Fig. 3.19 shows the transient peak electric field, E_{peak}, and the fraction F_{BD} of different particle injection locations. Note that each smooth curve is obtained by cubic spline interpolation of 9 data points obtained from the sensing probes. Unsurprisingly, the further away the ion event occurred from drain-gate edge (maximum vertical electric field region), the lower the magnitude of the induced peak electric field. This is consistent with a lower

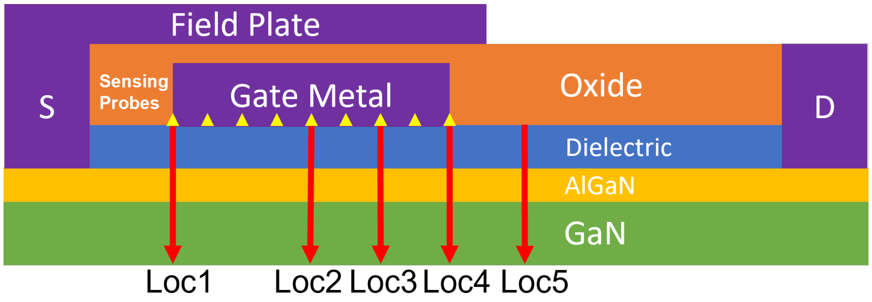

Figure 3.18: Heavy-ion particle injection locations (Loc1 to Loc5) along the channel. Yellow triangles mark 9 sensing probes along the gate length from 0 to 4 μm. The layers below GaN are not shown.

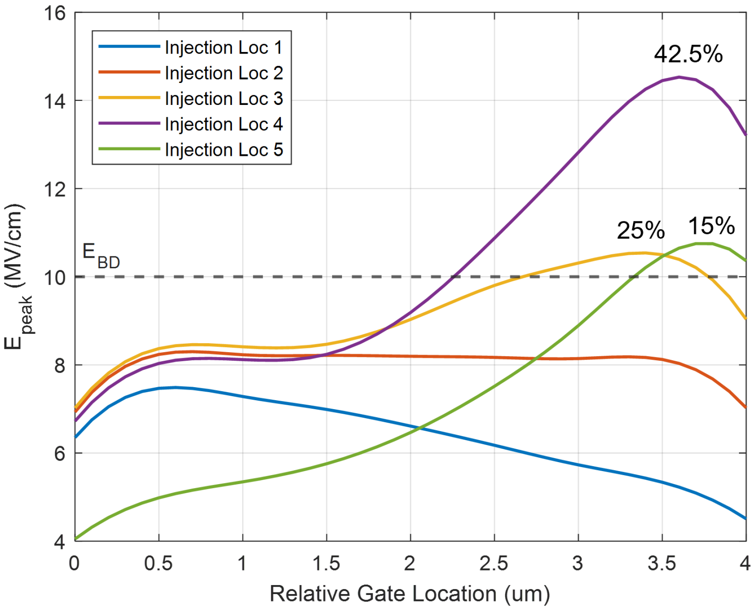

Figure 3.19: E_{peak} plotted as a function of position along the gate. Each plot represents a different ion injection location (Loc1 to Loc5). The percentage above each curve corresponds to the fraction of the transient that exceeds the breakdown field of the dielectric. V_{GS}=-14 V (off-state), V_{DS}=100 V, and LET=10 MeV·cm^2/mg (Si).

Table 3.7: t_{peak} of each sensing probe with different particle injection location.

Sensing Probe	Loc1	Loc2	Loc3	Loc4	Loc5
0 μm	0	0	0	0	0
0.5 μm	0	0	0	0	0
1 μm	0	0	0	0	0
1.5 μm	0	0	0	0	0
2 μm	0	0	0	0	0
2.5 μm	0	0	0	247 ps	0
3 μm	0	0	212 ps	442 ps	0
3.5 μm	0	0	260 ps	548 ps	158 ps
4 μm	0	0	0	419 ps	142 ps

efficiency of hole collection under the gate dielectric at longer distances away from the drain edge. The drain-gate edge (Loc4) event injection can therefore generate the largest transient peak electric field inside the dielectric due to the high vertical field component around this spot at the interface between the gate dielectric and the AlGaN layer. Compared with the 4 μm sensing probe, the 3.5 μm sensing probe has a slightly longer t_{peak} and a similar E_{peak} level. Therefore, the 3.5 μm sensing probe was selected for this study as it was considered the near-maximal case. We believe the lateral offset toward the source in the peak electric field is due to the much smaller lateral field (caused by V_{DS} across the off-state channel) displacing the hole distribution away from the drain node. Since this field is orders of magnitude smaller than the vertical field, there is only a small displacement observed. Conversely, these simulations also revealed that injections near the source-gate edge (Loc 1) produced peak transient electric fields with magnitudes far below the breakdown field. This result is strongly supported by the experimental data, in that only a few devices experienced source-side failures (source to gate) in the heavy-ion irradiation experiments.

Fig. 3.20 shows the time evolution of the transient peak electric field at the 3.5 μm sensing probe, generated by particles injected at seven different locations. Particle injection location has a significant effect on the transient spike shape and t_{peak}. Table 3.7 shows the t_{peak} of each sensing probe with different injection locations.

A similar trend can be observed as the injection location moves away from the drain-

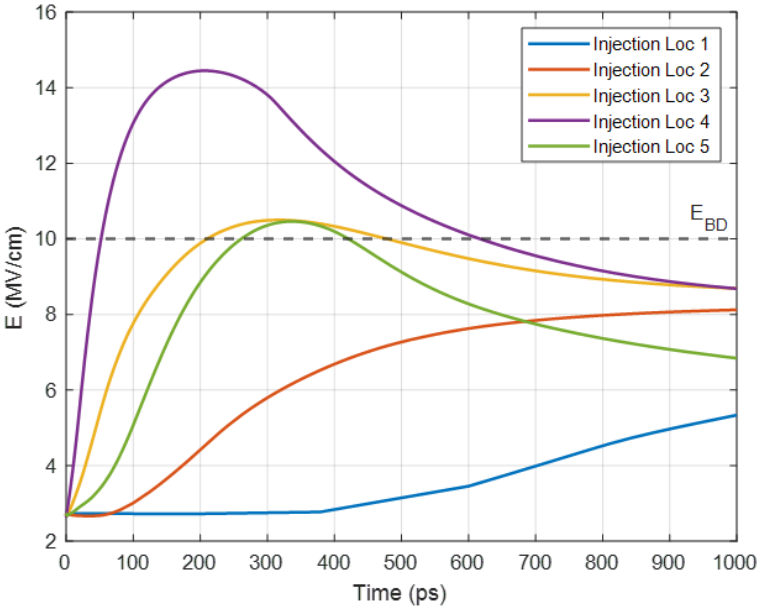

Figure 3.20: Electric field variation as a function of time for the 3.5 μm sensing probe for different particle injection locations. Total simulation time is 1000 ps. V_{GS}=-14 V (off-state), V_{DS}=100 V, and LET=10 MeV·cm^2/mg (Si). Radiation-induced electric field transient becomes weaker as the injection location moves away from the drain-gate edge (Loc4).

gate edge, t_{peak} becomes shorter, and the transient peak electric field becomes wider, related to the longer charge migration time. For example, injection locations Loc3 and Loc5 have similar E_{peak} and F_{BD} (Loc5 has slightly smaller F_{BD}), as shown in Fig. 3.19, but the time evolution of each transient is quite different. The transient peak electric field at Loc5's t_{peak} is considerably larger than that of Loc4 (3 μm and 3.5 μm sensing probes), which internally will lead to significantly different SEGR responses.

3.3.2 Particle LET Dependence

To better understand the influence of particle LET on SET magnitude and duration, five heavy-ion LET values were selected (from 1 to 20 MeV·cm^2/mg (Si)) spanning the entire range of LETs used in heavy-ion irradiation experiments. All particles were injected at the drain-gate edge (Loc4), which was shown to produce maximal SET responses, as previously discussed. For all these simulations, the device was biased in the off-state (V_{GS}=-14 V,

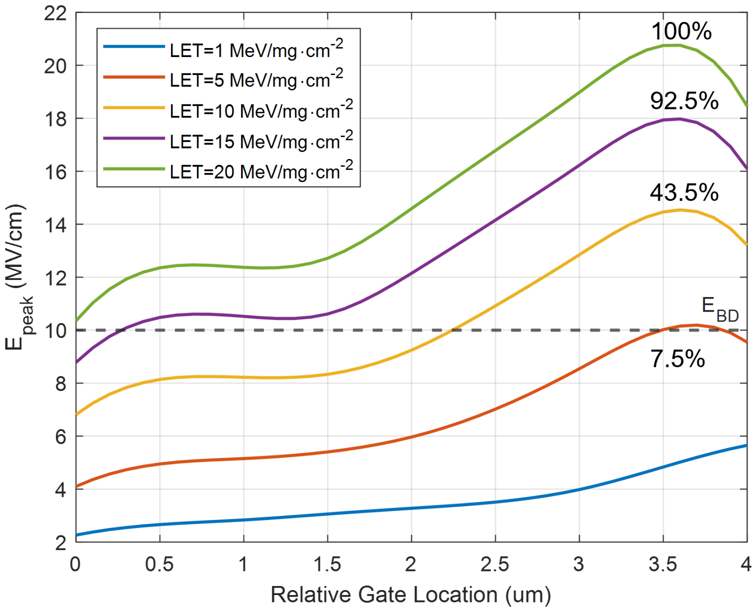

Figure 3.21: E_{peak} plotted as a function of position along the gate. Each plot represents a different particle LET (1 MeV·cm^2/mg (Si) to 20 MeV·cm^2/mg (Si)). The percentage above each curve corresponds to the fraction of the transient that exceeds the breakdown field of the dielectric. V_{GS}=-14 V (off-state), V_{DS}=100 V, and injection location is Loc4. Particles with higher LETs can produce stronger electric field transients.

V_{DS}=100 V).

Simulated E_{peak} and F_{BD} are presented in Fig. 3.21, while the resulting time-evolution of the electric-field transients vs. LET at the 3.5 μm probe point are shown in Fig. 3.22. Table 3.8 shows the corresponding t_{peak} of each sensing probe with different LETs.

Particles with higher LETs can deposit more energy density (charge density) along the injection track, inducing higher electron-hole pair density and larger peak transient electric fields. As expected, E_{peak}, F_{BD} and t_{peak} are proportional to particle LET and do not show much saturation as LET goes from 1 to 20 MeV·cm^2/mg (Si). Heavy-ion particle LET seems to have little effect on the transient shape. In general, particles with higher LETs have a significantly larger impact area and can generate an electric field transient inside the device with a higher peak and longer stress time, which potentially will create more defects inside the dielectric. This is consistent with the fact that particles with higher LETs will degrade

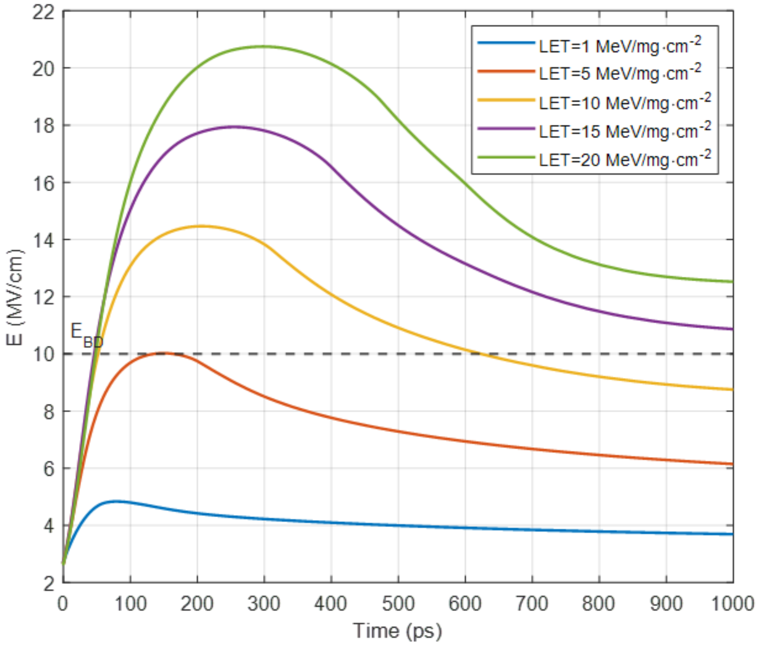

Figure 3.22: Electric field variation as a function of time for the 3.5 μm sensing probe for different particle LETs. Total simulation time is 1000 ps. V_{GS}=-14 V (off-state), V_{DS} =100 V, and injection location is Loc4. t_{peak} is proportional to particle LET.

Table 3.8: t_{peak} of each sensing probe with different particle LETs.

Sensing Probe	1[a]	5	10	15	20
0 μm	0	0	0	0	196 ps
0.5 μm	0	0	0	181 ps	404 ps
1 μm	0	0	0	278 ps	506 ps
1.5 μm	0	0	0	564 ps	638 ps
2 μm	0	0	0	717 ps	742 ps
2.5 μm	0	0	258 ps	818 ps	828 ps
3 μm	0	0	448 ps	895 ps	899 ps
3.5 μm	0	276 ps	548 ps	954 ps	952 ps
4 μm	0	0	421 ps	725 ps	967 ps

[a] Unit is MeV·cm^2/mg (Si).

the GaN HEMTs faster and induce a higher gate leakage current observed in heavy-ion experiments.

3.3.3 Drain Voltage Dependence

Heavy-ion radiation experimental results indicate drain voltage plays an important role in dielectric degradation. Thus, simulations were carried out with seven different drain voltages (V_{DS}), ranging from 75 to 400 V. For all simulations, a 10 MeV·cm^2/mg (Si) particle was injected through Loc4, while V_{GS} was set to -14 V.

Fig. 3.23 shows the simulated E_{peak} and F_{BD} with different V_{DS}. The electric field transients at 3.5 μm sensing probe are shown in Fig. 3.24. Table 3.9 shows the corresponding t_{peak} of each sensing probe with different V_{DS}.

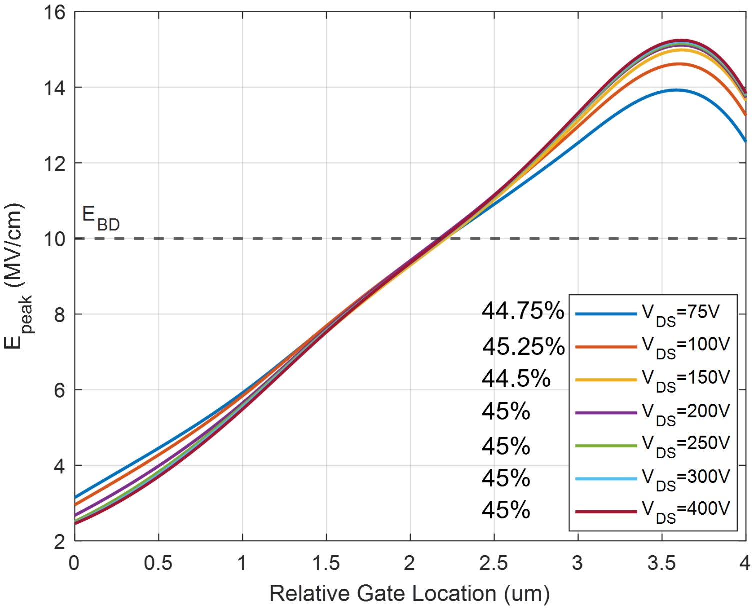

Figure 3.23: E_{peak} plotted as a function of position along the gate. Each plot represents a different drain voltage (75 V to 400 V). The percentage next to the legend corresponds to the fraction of the transient that exceeds the breakdown field of the dielectric. V_{GS}=-14 V (off-state), injection location is Loc4, and LET=10 MeV·cm^2/mg (Si). The fact that V_{DS} has little effect on particle-injected charge density causes the curves to overlap.

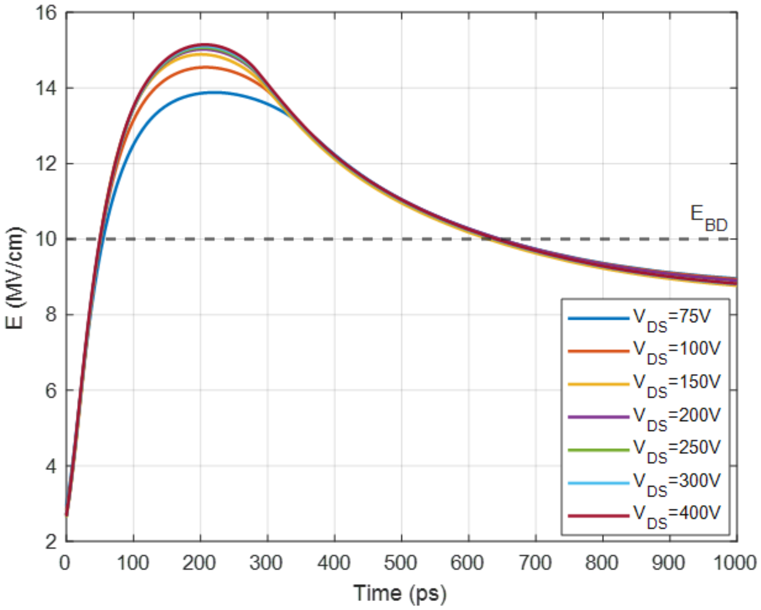

Figure 3.24: Electric field variation as a function of time for the 3.5 μm sensing probe for different drain voltages. Total simulation time is 1000 ps. V_{GS}=-14 V (off-state), injection location is Loc4, and LET=10 MeV·cm^2/mg (Si). t_{peak} remains at a similar level as V_{DS} increases, due to saturated charge collection.

As expected, E_{peak} and F_{BD} increase with the increasing drain voltage V_{DS}, because when biased under higher V_{DS}, particle-induced electron-hole pairs will be separated and collected with higher efficiency, which also leads to higher charge density accumulated at the dielectric/AlGaN interface. The electric field transient shape is relatively independent of V_{DS}. As V_{DS} increases above 200 V, F_{BD} starts to saturate. Compared with particle LET and injection location, drain voltage V_{DS} is not the dominant factor for E_{peak} and F_{BD}, as V_{DS} has little effect on particle injected charge density. Further, V_{DS} has little effect on t_{peak} at the 3.5 μm sensing probe, as the total amount of charge collected at the interface saturates when V_{DS} is above 100 V.

To further understand V_{DS} effects on heavy-ion-induced SET, the same simulations have been carried out, but with injection location Loc5. Fig. 3.25 and Fig. 3.26 show the corresponding results. Table 3.10 shows the corresponding t_{peak} of each sensing probe with different V_{DS} when particles are injected at Loc5. Apparently, with particle injection loca-

Table 3.9: t_{peak} of each sensing probe with different drain voltages. The particle is injected at Loc4.

Sensing Probe	75 V	100 V	150 V	200 V	250 V	300 V	400 V
0 μm	0	0	0	0	0	0	0
0.5 μm	0	0	0	0	0	0	0
1 μm	0	0	0	0	0	0	0
1.5 μm	0	0	0	0	0	0	0
2 μm	0	0	0	0	0	0	0
2.5 μm	273 ps	289 ps	261 ps	280 ps	278 ps	280 ps	290 ps
3 μm	450 ps	457 ps	461 ps	482 ps	468 ps	464 ps	466 ps
3.5 μm	570 ps	574 ps	574 ps	595 ps	575 ps	575 ps	575 ps
4 μm	428 ps	429 ps	426 ps	435 ps	435 ps	436 ps	436 ps

tion moving away from drain-gate edge, the electric field transient becomes more sensitive to V_{DS}. Higher V_{DS} results in higher charge collection efficiency due to the enhanced lateral electric field.

Table 3.10: t_{peak} of each sensing probe with different drain voltages. The particle is injected at Loc5.

Sensing Probe	75 V	100 V	150 V	200 V	250 V	300 V	400 V
0 μm	0	0	0	0	0	0	0
0.5 μm	0	0	0	0	0	0	0
1 μm	0	0	0	0	0	0	0
1.5 μm	0	0	0	0	0	0	0
2 μm	0	0	0	0	0	0	0
2.5 μm	0	0	0	0	0	0	0
3 μm	0	0	0	0	0	0	0
3.5 μm	0	158 ps	243 ps	268 ps	265 ps	287 ps	294 ps
4 μm	0	142 ps	252 ps	274 ps	277 ps	291 ps	296 ps

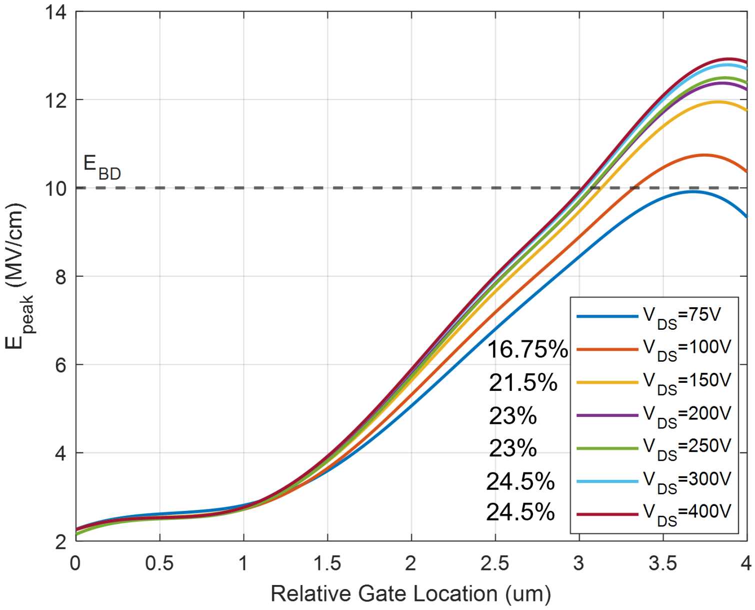

Figure 3.25: E_{peak} plotted as a function of position along the gate. Each plot represents a different drain voltage (75 V to 400 V). The percentage next to the legend corresponds to the fraction of the transient that exceeds the breakdown field of the dielectric. V_{GS}=-14 V (off-state), injection location is Loc5, and LET=10 MeV·cm^2/mg (Si).

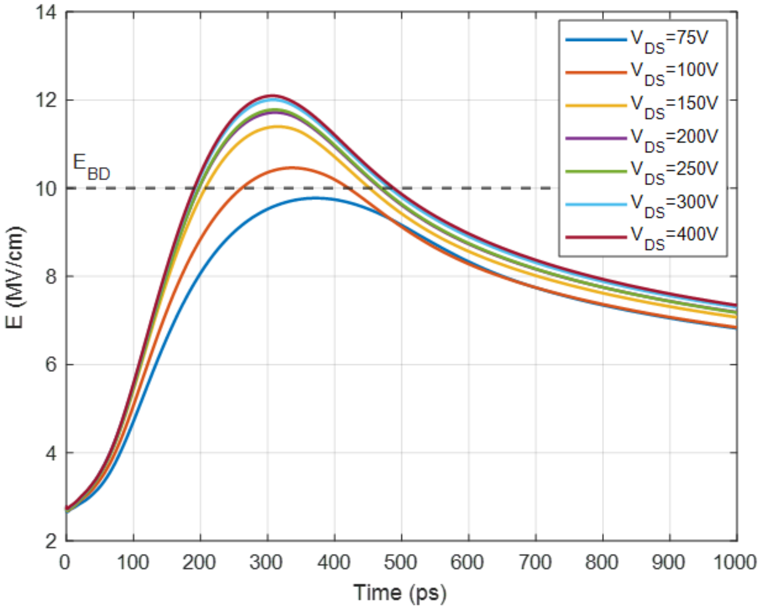

Figure 3.26: Electric field variation as a function of time for the 3.5 μm sensing probe for different drain voltages. Total simulation time is 1000 ps. V_{GS}=-14 V (off-state), injection location is Loc5, and LET=10 MeV·cm^2/mg (Si). With particle injection location moving away from drain-gate edge, the electric field transient becomes more sensitive to V_{DS}.

In addition, a simulation was carried out to explain the fact that no significant damage on the gate dielectric is observed in off-state zero-drain-voltage experiments, in which a 10 MeV·cm^2/mg (Si) particle was injected at Loc4 with V_{GS}=-14 V and V_{DS}=0 V. Corresponding simulation results are presented in Fig. 3.27 and Fig. 3.28. 100 V curve (same LET and injection location) is for direct comparison. As expected, without drain voltage, most of the heavy-ion-induced charges will recombine before being collected by the dielectric/AlGaN interface, which results in a significantly weaker electric field transient and little damage to the dielectric.

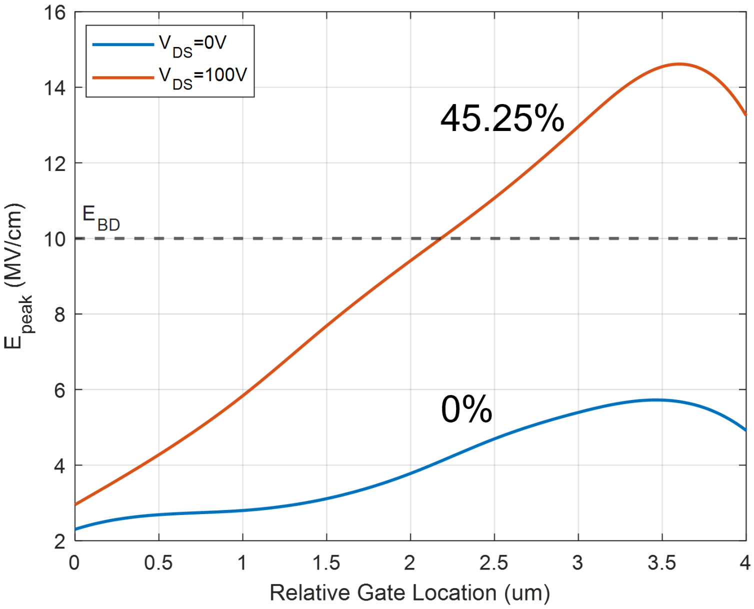

Figure 3.27: Simulated E_{peak} of zero drain voltage with particles injected at Loc4.The percentage above each curve represents the fraction of the transient that exceeds the breakdown field of the dielectric. V_{GS}=-14 V (off-state), injection location is Loc4, and LET=10 MeV·cm^2/mg (Si). Without drain voltage, most of the heavy-ion-induced charges will recombine quickly.

In general, GaN HEMT DUTs are more sensitive to SEGR, when they are biased under

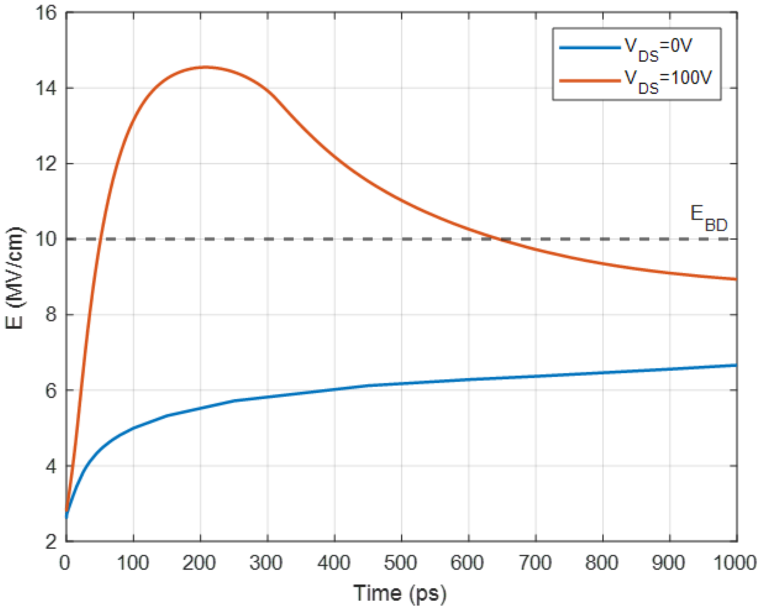

Figure 3.28: Electric field variation as a function of time for the 3.5 μm sensing probe for zero drain voltage with particle injected at Loc4. Total simulation time is 1000 ps. V_{GS}=-14 V (off-state), injection location is Loc4, and LET=10 MeV·cm^2/mg (Si). Charge collection efficiency has been significantly reduced with V_{DS} equals 0.

higher drain voltages, due to enhanced charge collection at the dielectric/AlGaN interface. The V_{DS} effects may play a more important role in reality, as a high density of electron-hole pairs are deposited inside regions that are further away from the gate edge. In other words, the gate area associated with drain area injection is a small portion of the total gate area. This V_{DS} dependency is consistent with our experimental data as shown in Fig. 4.11 and implies that SEGR is not limited to occurring only at or near Loc4 (at the drain edge), which explains why the experimental data previously presented show more sensitivity to V_{DS}.

3.3.4 Gate Voltage Dependence

Simulations were carried out with 6 different current injection levels (I_S), ranging from 0 A to 10 mA (same as the injection levels used in critical injection level experiments). Due to the 2DEG channel conductivity difference between the simulated device and the real device, a scaling factor of 10 is used for the injection level. Different gate voltages are used to achieve target current injection levels, which is slightly different from the actual experiments. This is due to the fact that the voltages on each of the electrodes in the device have to be defined first and then the current through each electrode can be calculated in TCAD DC solution. In other words, it is extremely hard to define the current conducting through each electrode first and calculate the corresponding voltage dynamically with our tool. To exclude injection location effects on the overall simulation results, four injection locations were used including Loc3, Loc3+, Loc4, and Loc5, as shown in Fig. 3.18. Loc3+ is slightly closer to the drain-gate edge (Loc4) compared to Loc3. For each location, a 10 MeV·cm^2/mg (Si) particle was injected with source grounded and V_{DS} equals 150 V.

Fig. 3.29, Fig. 3.30, Fig. 3.31, and Fig. 3.32 show the simulated E_{peak} and F_{BD}. Corresponding time-evolution of the electric-field transients vs. injection level at the 3.5 μm probe point are presented in Fig. 3.33, Fig. 3.34, Fig. 3.35, and Fig. 3.36. As expected, with the increasing 2DEG channel conductivity, the electric field transient induced by the injected particle becomes weaker, due to reduced charge collection efficiency. The corresponding electric field transients of injection levels below 1 mA are relatively similar, as the injected charge density is too high to be completely transported by the channel in a short time. This phenomenon is consistent with the experimental data (similar post-radiation off-state gate leakage current as shown in Fig. 3.13). The further the injection location is away from the source, the smaller the impact of current injection level on the transient electric field, which is related to reduced hole collection efficiency at the source contact. When the particle injection location is away from the source contact, radiation-induced holes have to migrate across the device before reaching the source electrode, during which part of the holes will be collected by the dielectric/AlGaN interface and contribute to electric field transient.

Overall, V_{GS} or the current injection level has a significant impact on E_{peak}, P_{BD}, and t_{peak}, which is due to weakened charge collection efficiency at the dielectric/AlGaN interface. With sufficiently large current injection levels, most of the radiation-induced charges will be swept away immediately before damaging the gate dielectric. The simulation results are consistent with our dielectric degradation hypothesis.

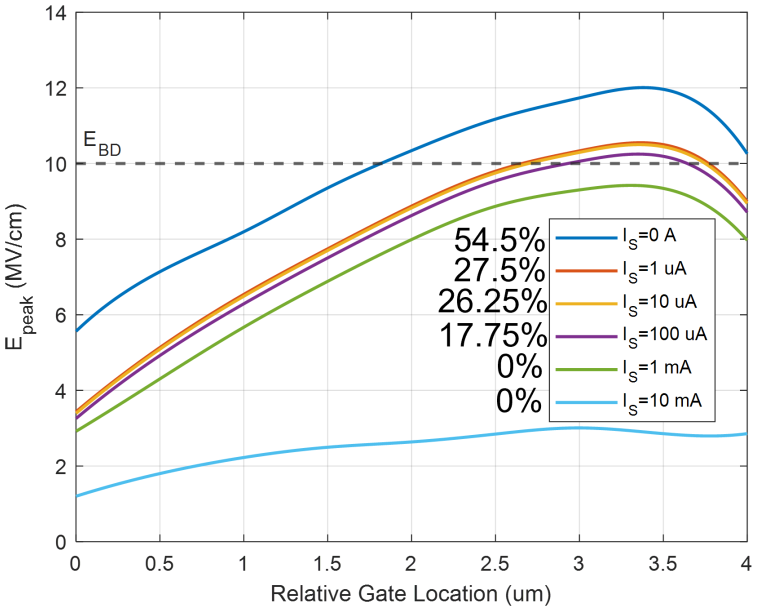

Figure 3.29: E_{peak} plotted as a function of position along the gate. Each plot represents a different current injection level (0 A to 10 mA). The corresponding F_{BD} is listed next to the legend. LET=10 MeV·cm^2/mg (Si), V_{DS}=150 V, and injection location is Loc3. A higher injection level leads to a weaker electric field transient.

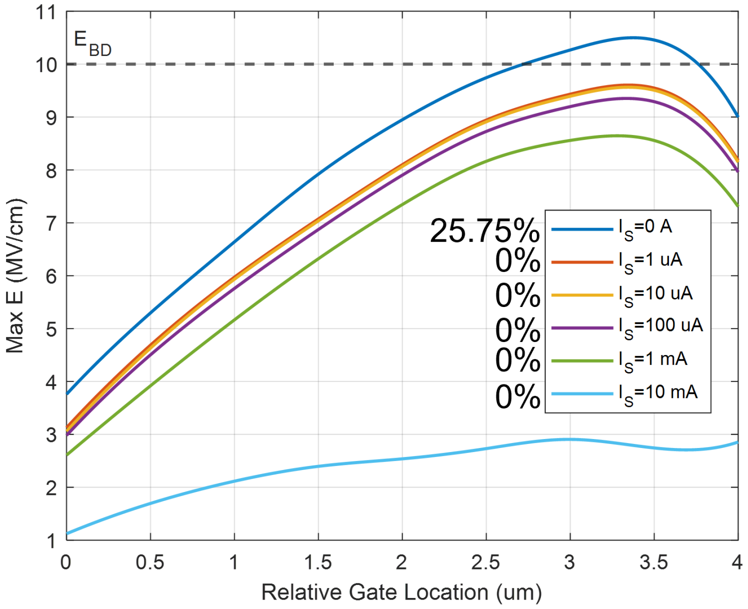

Figure 3.30: E_{peak} plotted as a function of position along the gate. Each plot represents a different current injection level (0 A to 10 mA). The corresponding F_{BD} is listed next to the legend. LET=10 MeV·cm^2/mg (Si), V_{DS}=150 V, and injection location is Loc3+. $E_{peak} < E_{BD}$, when injection level $\geq$ 1 mA.

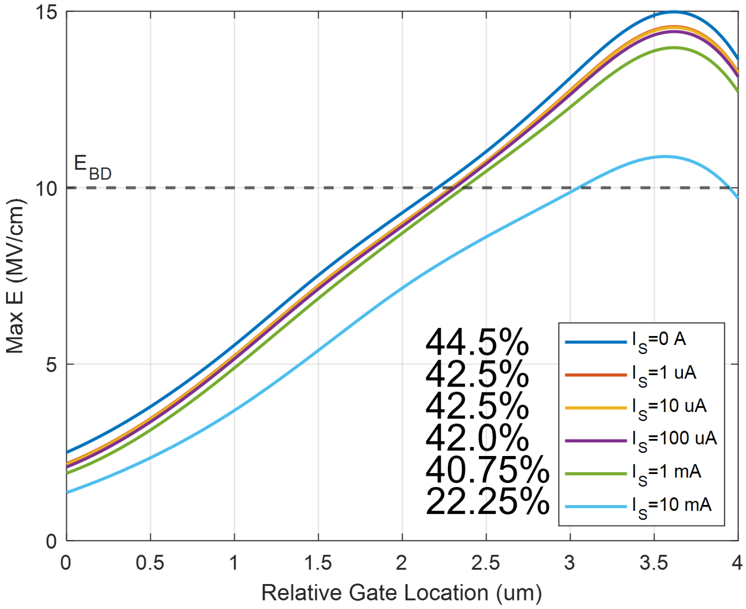

Figure 3.31: E_{peak} plotted as a function of position along the gate. Each plot represents a different current injection level (0 A to 10 mA). The corresponding F_{BD} is listed next to the legend. LET=10 MeV·cm^2/mg (Si), V_{DS}=150 V, and injection location is Loc4. Injection levels below 1 mA (1 to 100 μA), E_{peak}, and F_{BD} remain at similar levels.

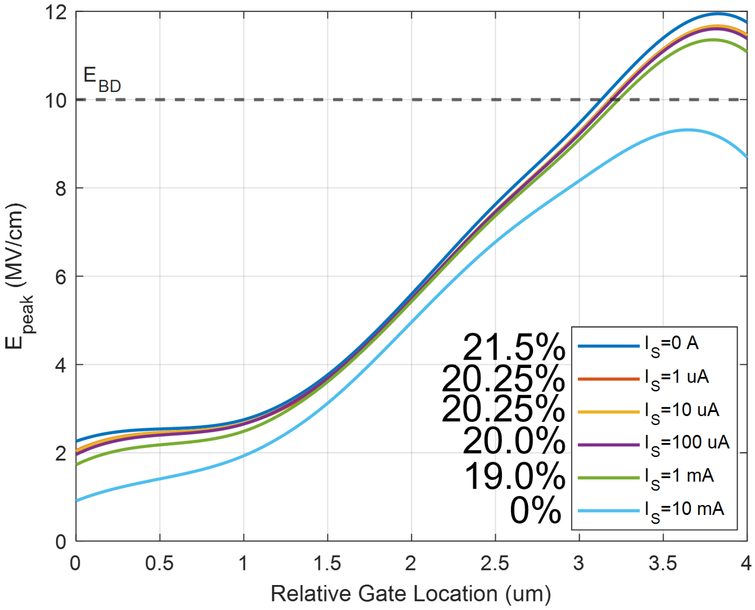

Figure 3.32: E_{peak} plotted as a function of position along the gate. Each plot represents a different current injection level (0 A to 10 mA). The corresponding F_{BD} is listed next to the legend. LET=10 MeV·cm^2/mg (Si), V_{DS}=150 V, and injection location is Loc5. Only at the 10 mA injection level, $Epeek$ and F_{BD} decreased significantly.

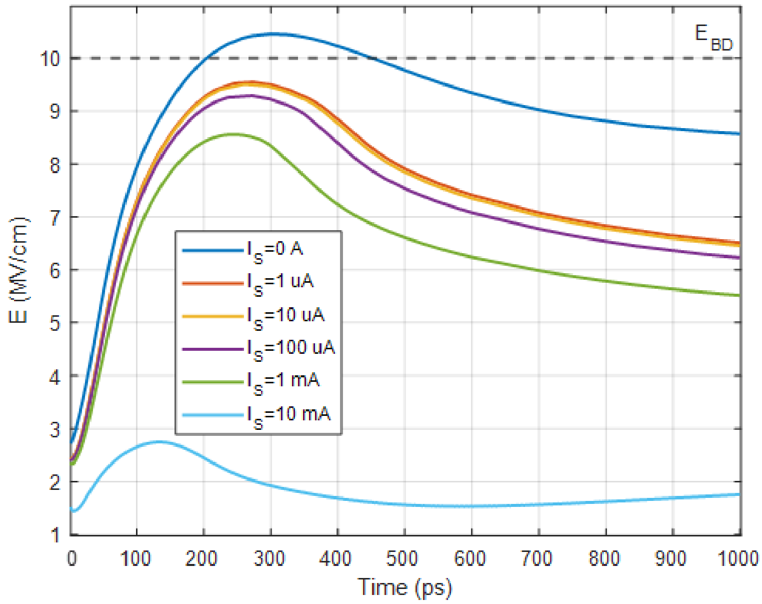

Figure 3.33: Electric field variation as a function of time for the 3.5 μm sensing probe for different current injection levels. Total simulation time is 1000 ps. LET=10 MeV·cm^2/mg (Si), V_{DS}=150 V, and injection location is Loc3. t_{peak} is proportional to the current injection level I_S.

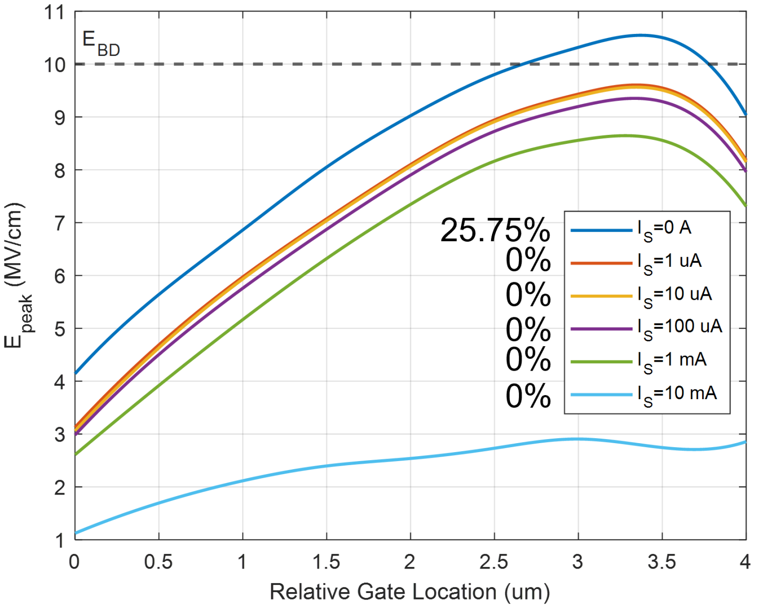

Figure 3.34: Electric field variation as a function of time for the 3.5 μm sensing probe for different current injection levels. Total simulation time is 1000 ps. LET=10 MeV·cm^2/mg (Si), V_{DS}=150 V, and injection location is Loc3+.

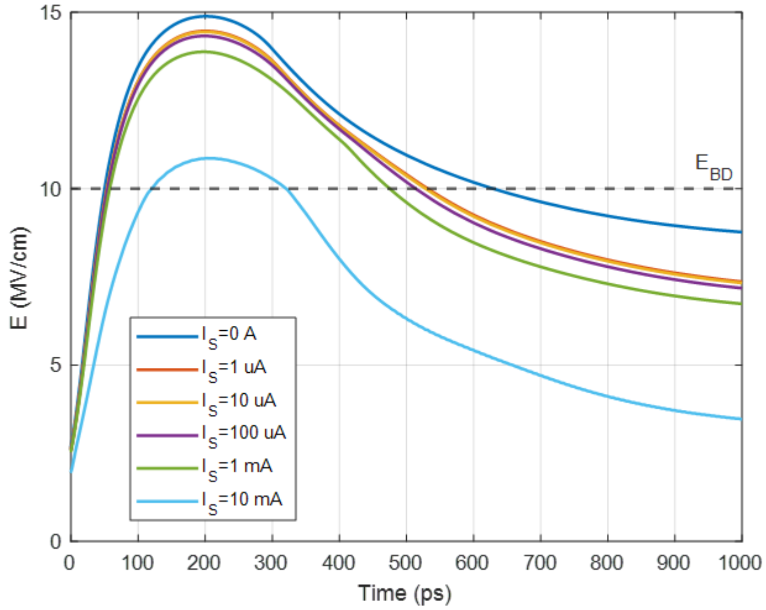

Figure 3.35: Electric field variation as a function of time for the 3.5 μm sensing probe for different current injection levels. Total simulation time is 1000 ps. LET=10 MeV·cm^2/mg (Si), V_{DS}=150 V, and injection location is Loc4.

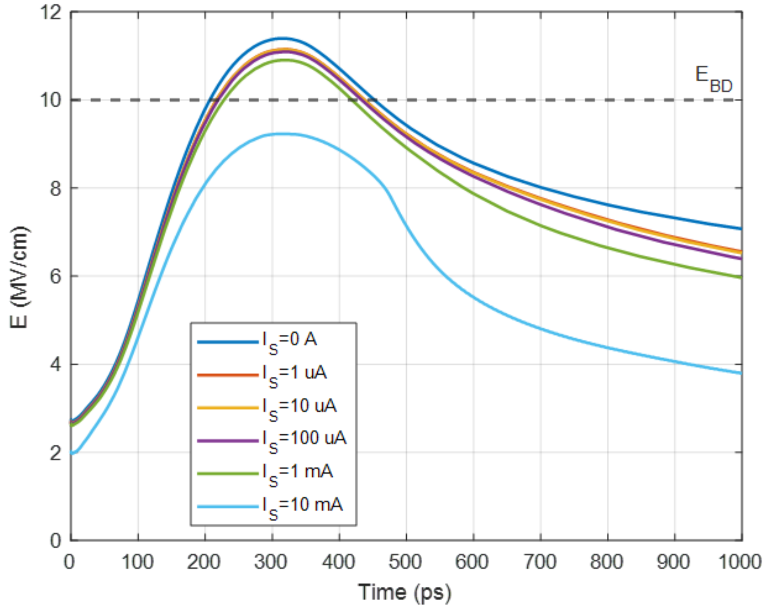

Figure 3.36: Electric field variation as a function of time for the 3.5 μm sensing probe for different current injection levels. Total simulation time is 1000 ps. LET=10 MeV·cm^2/mg (Si), V_{DS}=150 V, and injection location is Loc5.

3.4 Discussion

Displacement damage is believed to be another dominant mechanism in heavy-ion-induced dielectric degradation [29], [44]. However, the fact that no significant dielectric degradation was observed in off-state zero-drain-voltage experiments with a relatively high total effective fluence, indicates in our case charge-injection-related interaction is the dominant effect rather than displacement damage, as heavy-ion induced displacement damage is independent of device bias conditions. The results from critical injection level experiments and corresponding TCAD simulations further illustrate the idea that charge collection at the dielectric/AlGaN interface dominates SEGR response of this type of D-mode GaN HEMT rather than displacement damage. Although, it also could be due to the LETs we used in our experiments being too low compared with the values reported in [29], which will not be able to generate enough displacement damage to initiate a breakdown process.

As discussed before, our dielectric degradation hypothesis is that the electric field transients induced by heavy ions exceed the dielectric critical strength and consequently lead to radiation-induced SBD and HBD events observed during heavy-ion irradiation by generating defects inside the dielectric, which is consistent with experimental and simulation data. As reported in [28], [54], and [55], authors proposed that radiation-induced SBD and radiation-induced HBD shared a common statistical and physical origin, in other words, both breakdown modes were related to the same kinds of defect generation and initiated by the same effect (a defect-related conduction path was formed eventually). We believe that compared with radiation-induced SBD, radiation-induced HBD has a higher critical defect density and a lower relative conduction path resistance. This hypothesis is consistent with the phenomenon that radiation-induced HBD usually happened at higher V_{DS}, higher LET, and higher heavy-ion fluence, as shown in Fig. 3.14. More details on the radiation-induced dielectric degradation mechanism will be presented in the next chapter.

Particle injection locations have a significant impact on incident-particle-induced SETs. For a particle LET of 10 MeV·cm^2/mg (Si) with V_{GS}=-14 V, V_{DS}=100 V), the only injection locations that could produce a transient magnitude exceeding E_{BD} were between the Loc3 and Loc5 – a third of the gate length from the drain edge to in the drain itself. Here we define the region between Loc3 and Loc5 as the sensitive area, A_{sen}, for 10 MeV·cm^2/mg

(Si) particles. Typically, the width of the sensitive area is proportional to particle LET. In heavy-ion experiments, we observed a certain level of radiation fluence was required to initiate dielectric degradation at moderate field strength. A similar phenomenon was also reported in [53], which can be explained by the fact that compared with the total device area, A_{sen} is a considerably smaller region and the probability of a particle hitting it is relatively small. The transient electric field spikes which are lower than E_{BD} can also generate defects inside the dielectric, which will contribute to dielectric degradation [28].

Particle LET is another crucial factor in GaN HEMTs' SEGR response. In general, particles with higher LET require a lower electric field to initiate the breakdown process, and under the same electric field stress particles with higher LET can induce larger gate leakage currents (same total fluence). Moreover, particles with larger LETs can generate more defects along their tracks, also considered to be a key factor in dielectric degradation [44], [32]. Both V_{DS} and V_{GS} have a significant impact on the radiation-induced charge collection efficiency. Basically, a higher V_{DS} or a lower 2DEG channel conductivity (lower V_{GS} in our case) will lead to a stronger electric field transient, when an incident particle is injected into the device. V_{DS} may also affect the defect types generated by heavy ions inside the dielectric.

Overall, E_{peak}, F_{BD}, and t_{peak} are closely related to secondary particle injection location, particle LET, V_{DS}, and V_{GS}. Compared with V_{DS}, V_{GS}, particle injection location, and corresponding LET are the dominant factors that impact t_{peak}. On the other hand, all four factors have a significant effect on E_{peak} and F_{BD}. Among the parameters, V_{DS} has the least influence. Basically, all four factors have a significant impact on the total amount of charges collected by the dielectric/AlGaN interface, which defines device responses to heavy-ion radiation.

Chapter 4

Terrestrial Neutron Induced Single Event Effects in GaN HEMTs

Terrestrial cosmic rays consist of neutrons, protons, pions, muons, electrons, and photons, with neutrons making up more than 90% of the flux at terrestrial altitudes [9]. It has been experimentally validated that terrestrial neutrons can induce Destructive Single-Event Effects (DSEEs) in various power semiconductor devices like high-voltage diodes, thyristors, power MOSFETs and insulated-gate bipolar transistors (IGBTs) [16], [17], [18] and limit their reliability performance in terrestrial power applications. While the neutrons themselves are not ionizing, the ionizing secondary particles generated by nuclear reactions between incident neutrons and the device materials can induce huge transient excess charge events and are the main cause of neutron-induced destructive SEEs in GaN HEMTs in the terrestrial environment.

In this chapter, the effects of neutron-induced single-event damage in depletion mode (D-mode) GaN HEMTs have been studied as a function of off-state (blocking) drain voltage stress in the highly accelerated neutron beam provided by Los Alamos Neutron Science Center (LANSCE) Irradiation of Chips Electronics (ICE) house. Post-radiation characterization measurements indicate neutron radiation-induced dielectric degradation, including soft and hard breakdown. LANSCE provides a neutron spectrum that mimics the actual terrestrial cosmic ray neutron spectrum [56] and thus the observed failure rates under the accelerated beam conditions can be directly extrapolated to field failure rates under nominal terrestrial conditions.

Further, Monte-Carlo nuclear reaction simulations using Geant4 [57] software produced an accounting of all the neutron-induced secondary particle events within the GaN HEMT sensitive regions irradiated by the LANSCE neutron beam. For each secondary particle event predicted by Geant4, a corresponding linear energy transfer (LET) in both silicon and GaN was calculated using SRIM [58]. The results of numerous simulations were combined to pro-

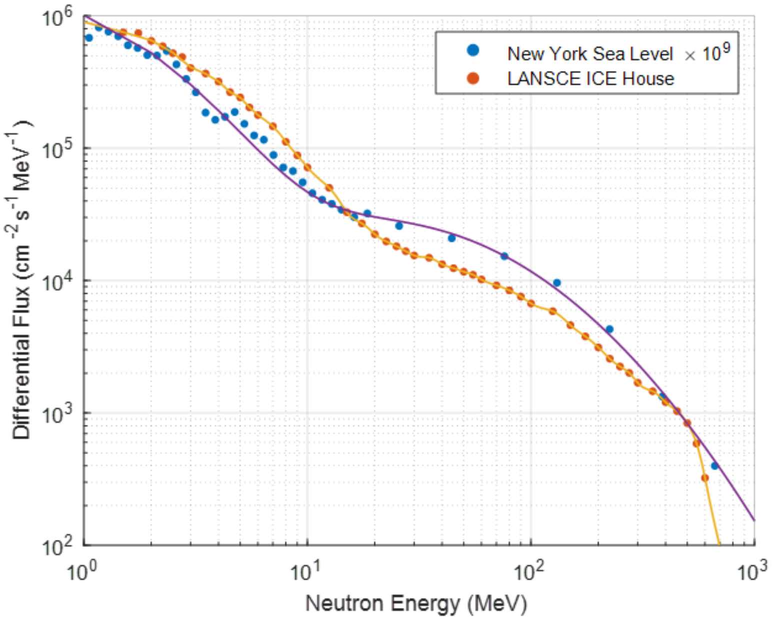

Figure 4.1: The LANSCE neutron spectrum is very similar to the cosmic-ray-induced neutron spectrum at New York City, but with a cutoff around 700 MeV. The LANSCE neutron spectrum is $> 10^8$ more intense. The purple line is the fitting curve for the terrestrial neutron spectrum. The yellow line is the fitting curve of the LANSCE neutron spectrum.

duce an estimate of the terrestrial neutron-induced secondary particle LET spectrum. From this, it was determined that most events in the GaN HEMT had an LET $\leq$ 10 MeV·cm^2/mg (Si). Together with the 2D TACD simulation results presented in the last chapter we provide an insight into the impact of neutron-induced heavy ions in the GaN HEMT power devices as a function of their bias conditions, particle injection locations, and secondary particle LET in producing the observed SEGR.

4.1 Experimental Details

The broad-spectrum neutron source provided by the LANSCE ICE-House provides a highly-accelerated analog of the terrestrial neutron spectrum, as shown in Fig. 4.1 [59]. The acceleration factor of the LANSCE facility is approximately 2×10^8, or roughly, about 23,000 years per hour of test time (based on neutron flux spectrum with $E_n > 10$ MeV) with respect to N.Y.C sea-level flux [59].

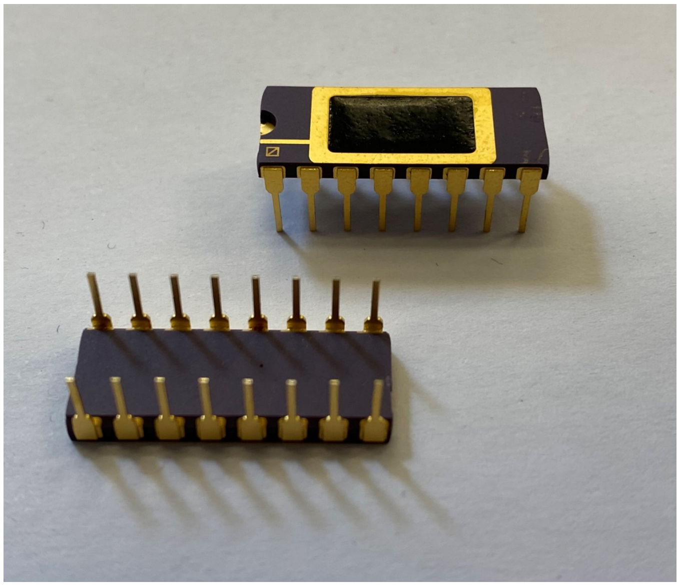

Figure 4.2: A picture of commercially available D-mode GaN HEMT packaged in 16-pin DIP package. Compared with the QFN package, DIP package is cheaper and easier to handle.

One wafer of transistor test structures fabricated from a commercially available D-mode GaN HEMT technology was singulated and packaged in 16-pin ceramic dual-in-line packages (DIP) as shown in Fig. 4.2, which serve as the device-under-test (DUT) for neutron experiments.

A parallel neutron testing system is designed and validated to maximize beam time usage efficiency at LANSCE, consisting of motherboards (Fig. 4.3 (a)), DUT boards (Fig. 4.3 (b)), and current sensing modules. A schematic of the parallel neutron testing system is shown in Fig. 4.4. Fig. 4.5 shows a picture of the parallel neutron testing system placed in the neutron beam line, which has four motherboards and DUT boards connected. The vertical boards are the DUT boards. A unique motherboard is the horizontal base for each DUT board, and the individual DUT sense modules are the numerous small vertical boards plugged into the motherboards. Due to the relatively large neutron beam area (8 cm in diameter) provided by LANSCE, the DUT boards are optimized to place twenty devices in the neutron beam. The fact that the neutrons are highly penetrating enabled us to stack up to eight DUT boards in the beam. During the neutron irradiation, multiple DUT boards were placed in parallel in the neutron beam with individual high-voltage power supplies providing a unique stress voltage for each pair of DUT boards. Twenty DUTs were connected in parallel on each DUT board, which was plugged into a motherboard via a large edge connector. A common gate voltage (V_{GS}) of -14 V was continuously applied to keep the depletion-mode HEMT in the off-state, or blocking condition, so that the drain region electric field was maximized, which is considered the worst-case condition for DSEEs, as demonstrated previously.

Every DUT has its own unique current sense module (20 sense modules per motherboard) that outputs a transistor-transistor logic (TTL) signal for real-time status monitoring and isolates the DUT from the others when a failure is detected. A picture of the current sensing module is shown in Fig. 4.6. Failure was defined as an off-state I_G or I_D leakage current exceeding 100 μA. For comparison, the baseline off-state gate leakage is 10 nA and the off-state drain leakage is on the same level. Single-event burn-out and gate-rupture (SEB/SEGR) are the basic failure mechanisms we expected under neutron radiation. The TTL signal of each DUT is collected by two NI PXI-6509 digital input/output (DIO) modules. Each NI PXI-6509 DIO module has 94 digital channels, which is able to monitor up to four motherboards at one time.

Four high-voltage DC power supplies (three NI RMX-4127 and one Keithley 2260B-800-1) and a low-voltage DC power supply (Keithley 2231A-30-3) were used for providing V_{DS} and V_{GS} in the neutron irradiation experiments. The NI RMX-4127 has a maximum output power of 1500 W, output voltage ranges from 0 to 650 V, and output current ranges from 0 to 7 A. The maximum output power of Keithley 2260B-800-1 is 360W, with 800 V maximum output voltage and 1.44 A maximum output current. The Keithley 2231A-30-3 is a triple-channel power supply, which can output 30 V and 3 A, with a maximum total power of 95 W. All instruments, including power supplies and DIO modules, are controlled by the embedded controller via an NI LabVIEW program.

Seven different drain voltage stresses were used from 75 V to 400 V. The DUTs were irradiated with the neutron beam continuously. Typically, the reliability experiments are taken to 80% to 90% failures. Due to the limited beam time available in LANSCE, we stopped the neutron beam when up to 50% of the devices failed on each DUT board, which will tend to over-emphasize the early failures.

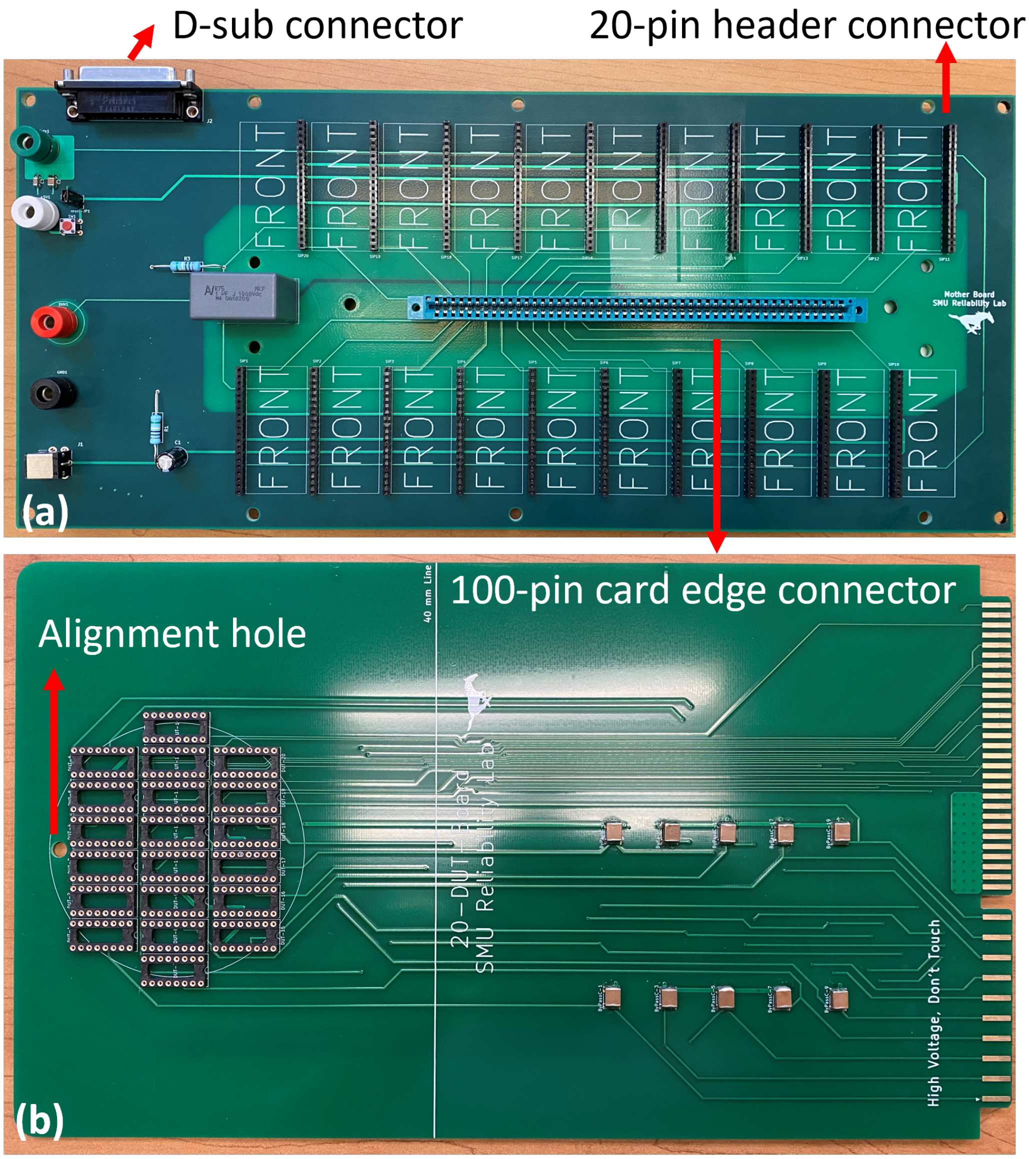

Figure 4.3: Pictures of the parallel neutron testing system motherboard (a), and DUT board (b). The current sensing module is connected to the motherboard via a 20-pin header connector. A D-sub cable enables communication between the controlling PC and the motherboard. The DUT board is vertically plugged into the motherboard via a 100-pin card edge connector. The small hole on top of the DUT board is used for aligning all DUT boards in the neutron beam line via a laser pointer.

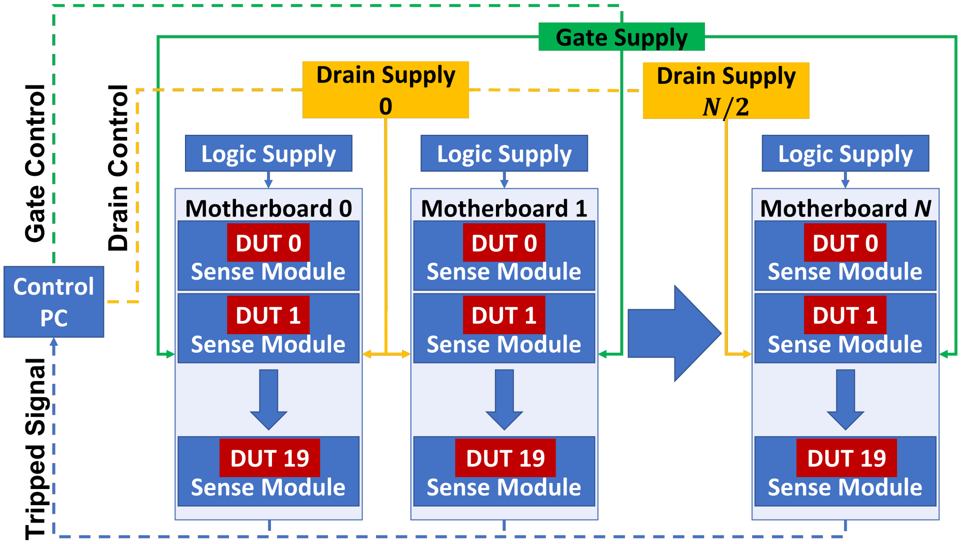

Figure 4.4: Schematic of the parallel neutron testing system. For each motherboard, 20 devices are connected in parallel and kept in the off-state. Each individual sense module outputs a TTL signal for real-time DUT status recording. The maximum handling voltage for the system is 1kV.

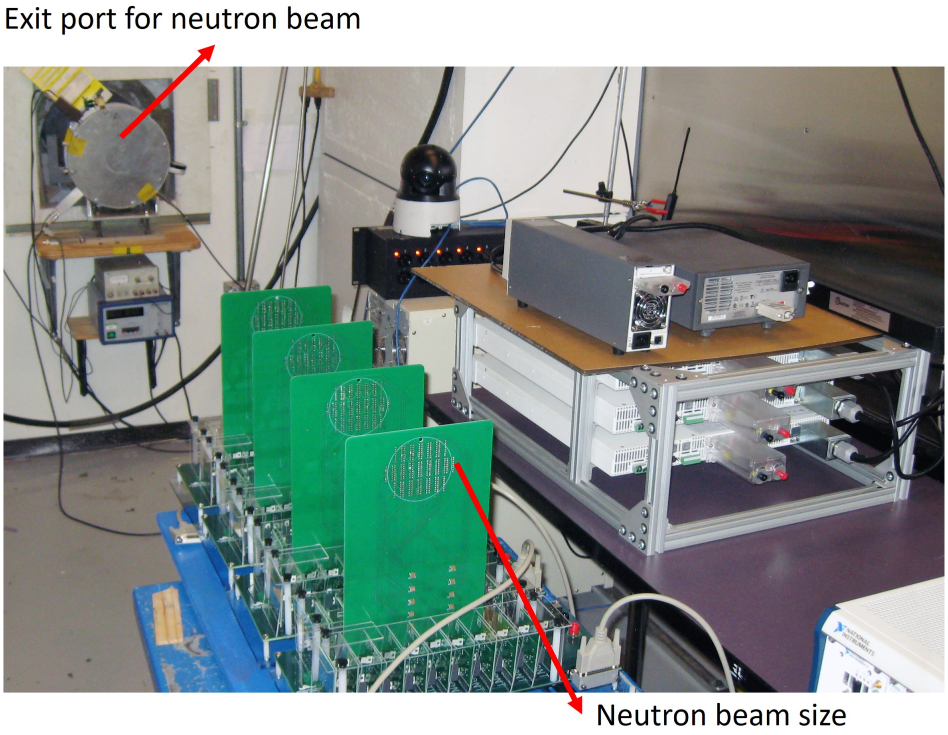

Figure 4.5: Parallel neutron testing system with four motherboards connected. Photo was taken in the LANSCE ICE house. The neutron beam is within the white circles printed on the top of the four vertical DUT boards in the photo.

Figure 4.6: A picture of the current sensing module. Total power consumption at 600 V is approximately 0.9 W. The low-cost modular design allows for fast replacement in the event of damage. The circuit was designed and validated by Danyal Ahsanullah.

4.2 Experimental Results

4.2.1 Neutron Irradiation Results

A total of 360 devices were tested in our experiment to evaluate the variation in neutron tolerance. The test results and corresponding setups are shown in Table 4.1. Notice that the listed results are the combination of multiple experimental outcomes with different neutron fluence. Fig. 4.9 summarizes the cumulative probability vs neutron fluence with different drain voltages. Neutron beam divergence and board attenuation have been accounted for – the detected neutron flux is reduced due to the divergence as the distance increases between the DUT and the source, and a percentage of the flux is absorbed/scattered at each DUT board [11]. The total neutron fluence f_N that irradiated the Nth DUT board is given by the following equation:

$$f_N = f_0 \cdot \Omega_N \cdot (a)^{(N-1)} \tag{4.1}$$

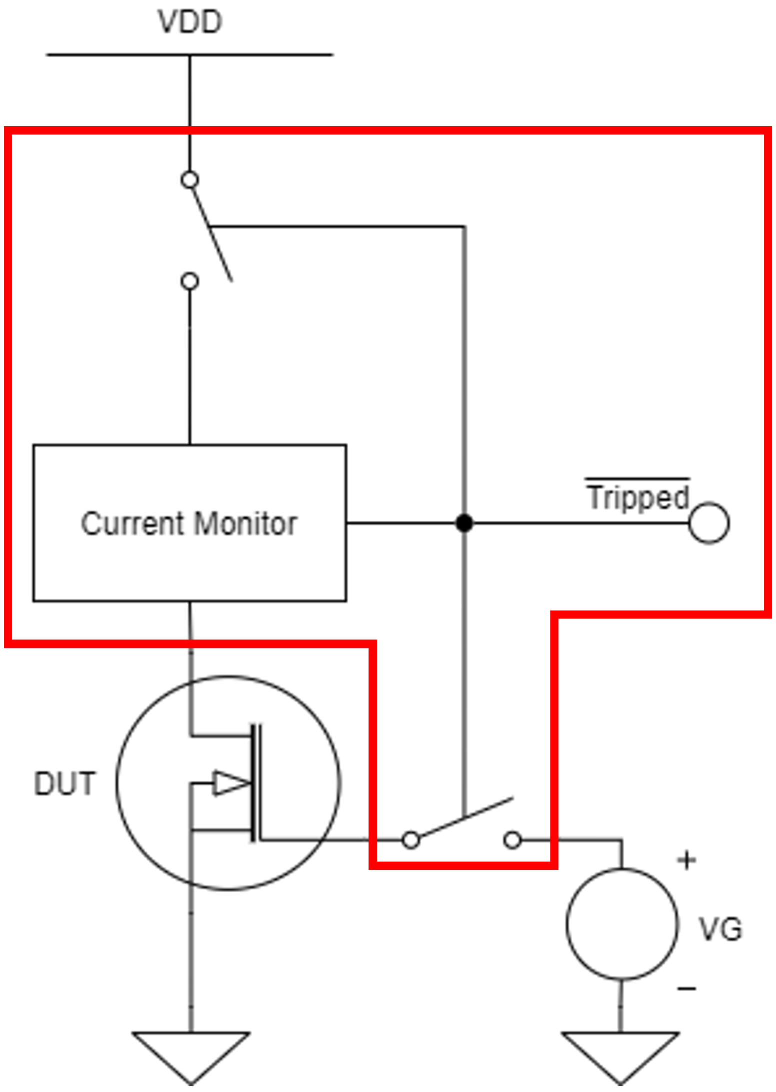

Figure 4.7: A simplified schematic of the current sensing module. Red lines mark the current sensing module. Two reed relays at the drain and gate prevent failed devices from further impacting the system, which theoretically enables us to keep irradiating the DUTs until all of them experience failures. Instead of monitoring real-time current, the parallel neutron testing system records the status (tripped or not) of each DUT.

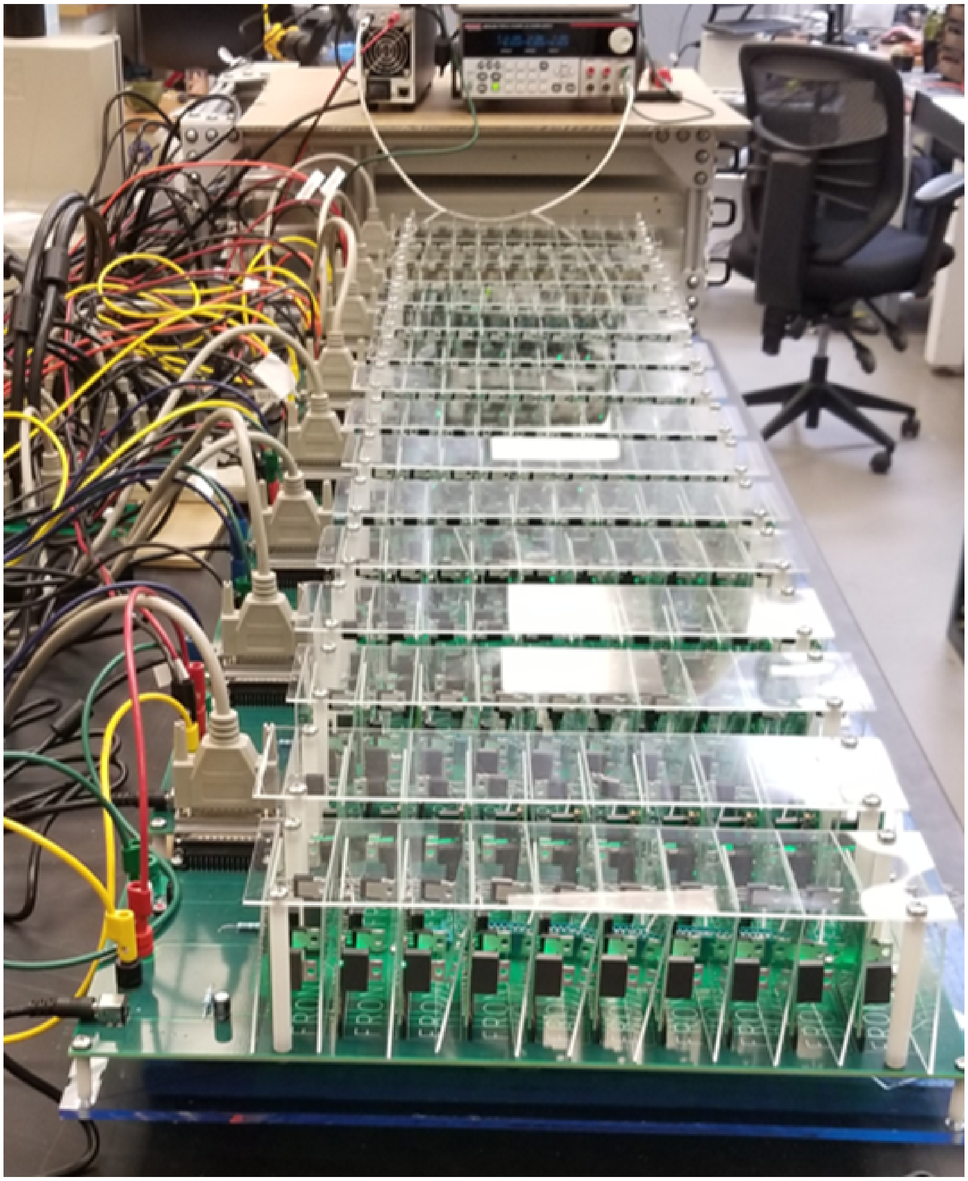

Figure 4.8: A picture of the parallel neutron testing system without DUT boards. To prevent neighboring sensing modules from touching each other and causing catastrophic failures, thick acrylic boards are put between the sensing modules. The top acrylic boards prevent people from touching the high-voltage components. The bottom blue acrylic boards ensure no potential shorts at the back side of the PCB boards. Eight motherboards are mounted on a wood base, ensuring the good alignment of DUT boards.

Table 4.1: Neutron Radiation Experiment Results.

Drain Voltage[a]	Sample Number	Cu. Failures	Cu. Probability
75 V	40	21	52.5%
100 V	60	23	38.3%
150 V	100	31	31.0%
200 V	80	31	38.8%
250 V	40	22	55.0%
300 V	20	8	40.0%
400 V	20	9	45.0%

[a] Gate voltage is -14 V for all conditions.

where f_0 is the total neutron fluence, Ω_N is the solid angle of the Nth DUT board and a is the dispersion coefficient per DUT board [11]. In our case, we chose a=5% [11].

All the data points plotted in Fig. 4.9 are derived from the mean value of several experimental results at each condition. Early failures were observed with a cumulative probability below 15% for most drain stresses. These are attributed to higher as-processed defect concentrations (no burn-in or high-temperature op-life was used to screen devices prior to testing them under neutron irradiation). The fact that a certain level ($> 10^8$ n/cm^2) of radiation fluence was required to initiate dielectric degradation at moderate field strength ($V_{DS} \leq 300$ V) is due to the fact that compared with the total device area, the sensitive area is a small region and the probability of a particle hitting it is relatively small.

For the voltage range from 75 to 200 V, no significant relationship between drain bias and cumulative probability was observed. On the contrary, above 200V a distinct increase in cumulative probability was observed with increasing drain stress. The fact that data points can be separated into two clusters ($V_D \geq 250$ V and $V_D \leq 200$ V) implies a mechanistic threshold voltage around 200 to 250 V. The main failure mode observed under irradiation was increased leakage current from drain to gate, with the majority of failures occurring at the high-field drain edge. During the experiments, some of the failed devices experienced catastrophic failure (hard short between gate and drain), indicative of the traditional SEB/SEGR. However, most of the observed failures were compliance failures, where the gate

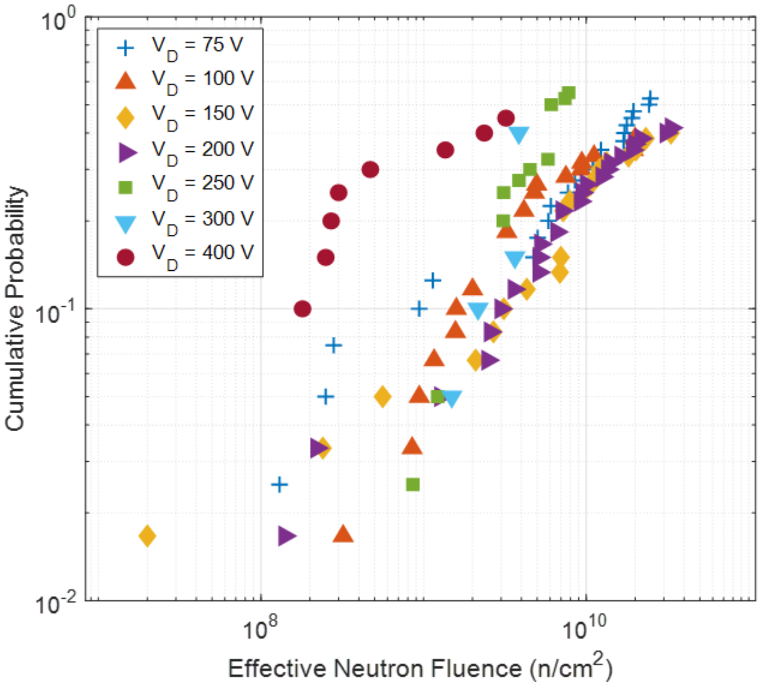

Figure 4.9: Mean Cumulative Probability vs Effective Neutron Fluence under different drain voltages. Early failures were observed with a cumulative probability below 15%. A certain level of radiation fluence was required to initiate dielectric degradation at moderate field strength.

to drain leakage current had increased to 100 μA. This failure mode has also been seen in heavy-ion radiation experiments we performed on similar devices – where the transistor is still functional but with higher gate/drain/source leakages implying a partial breakdown of the gate dielectric.

To understand the statistical properties of the neutron radiation-induced failures in AlGaN/GaN HEMTs, we performed the Weibull fitting on the calculated cumulative probability data, which has the following functional form [60]:

$$F = 1 - e^{-(\frac{f}{\lambda})^k} \tag{4.2}$$

where F is the cumulative probability, f is the effective neutron fluence, and λ and k are the scale parameter and the shape parameter, respectively, determining the width and slope

Table 4.2: Summary of Weibull fitting parameters.

Drain Voltage[a]	Scale Param λ	Shape Param k	R Square
75 V	4.0×10^{10}	1.1	0.98
100 V	4.3×10^{10}	0.8	0.85
150 V	3.9×10^{10}	1.2	0.88
200 V	3.8×10^{10}	1.1	0.94
250 V	9.8×10^{9}	1.4	0.94
300 V	5.8×10^{9}	2.4	0.74
400 V	4.9×10^{9}	0.6	0.76

[a] Gate voltage is -14 V for all conditions.

of the function. The parameters with their coefficients of determination, and R^2, are summarized in Table 4.2. The cumulative probability curves calculated with the corresponding Weibull distribution parameters are plotted in Fig. 4.10. We cut off the distributions below 1×10^9 n/cm^2 effective neutron fluence (eliminating part of the early failures), except for the 400 V drain bias condition. In general, higher drain stress voltage exhibits a higher cumulative probability of failure for a given neutron fluence, as higher V_{DS} results in higher charge collection efficiency due to the enhanced lateral electric field.

For most bias conditions, the shape parameter k is close to 1 with random failures implying that λ is proportional to the mean fluence to failure [60]. k is smaller than 1 for 100 V, 250 V, and 400 V data, which indicates the presence of early failures which happened at the beginning of the experiment. A possible explanation for these early failures is that they were induced by defective devices. The scale parameter k for 100 V and 250 V data are close to 1 because we already excluded the early failures. For 300 V, the corresponding shape factor k is 2.4, much larger than 1, which is because most failures happened at the same time. However, for the 400 V case, 30% of the testing samples failed before the neutron fluence reached 10^9 n/cm^2, which cannot be explained by our defective device assumption.

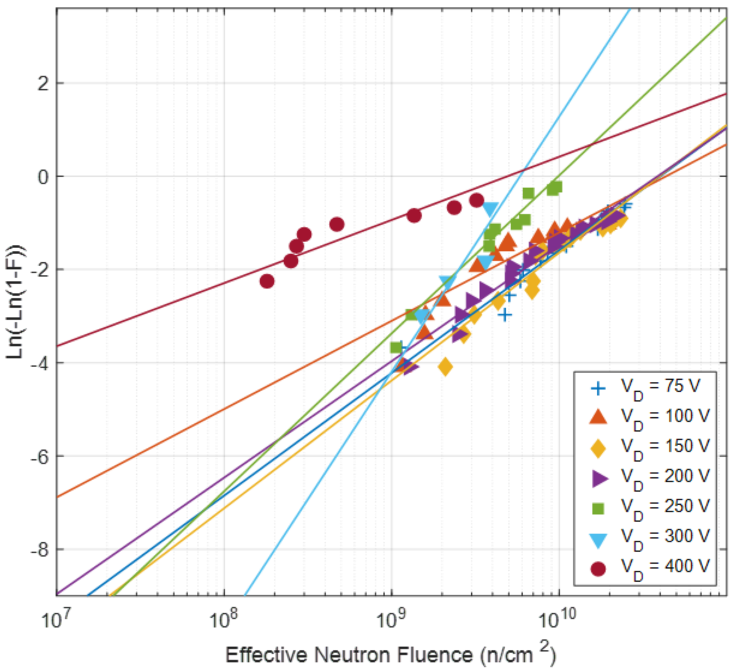

Figure 4.10: The normalized mean cumulative probabilities fitted to Weibull distributions. The early failures for drain voltage below 400 V are ignored. Higher drain stress voltage exhibits a higher cumulative probability of failure for a given neutron fluence.

This phenomenon could also be an indication of another failure mechanism under neutron radiation. To further investigate this problem, more experiments are required for drain voltages above 400 V. No matter from the calculated scale parameters or the plots, we find a dramatic change between 200 V and 250 V, which may indicate a threshold voltage in this range.

Extrapolated failure rates at sea level (1 FIT = 1 failure/billion hours) have been calculated as a function of drain voltage, as shown in Fig. 4.11, where the error bars represent the 95% confidence level. The orange dashed lines are the first-order linear fitting curve of the first 4 data points and the exponential fitting curve of the last 4 data points with the 95% confidence level. The red solid line is the summation of the orange lines, which indicates an experimental reliability function with a threshold voltage around 200 V. It appears that the failure rate is independent of drain voltage stress up to about 200-250 V, at which

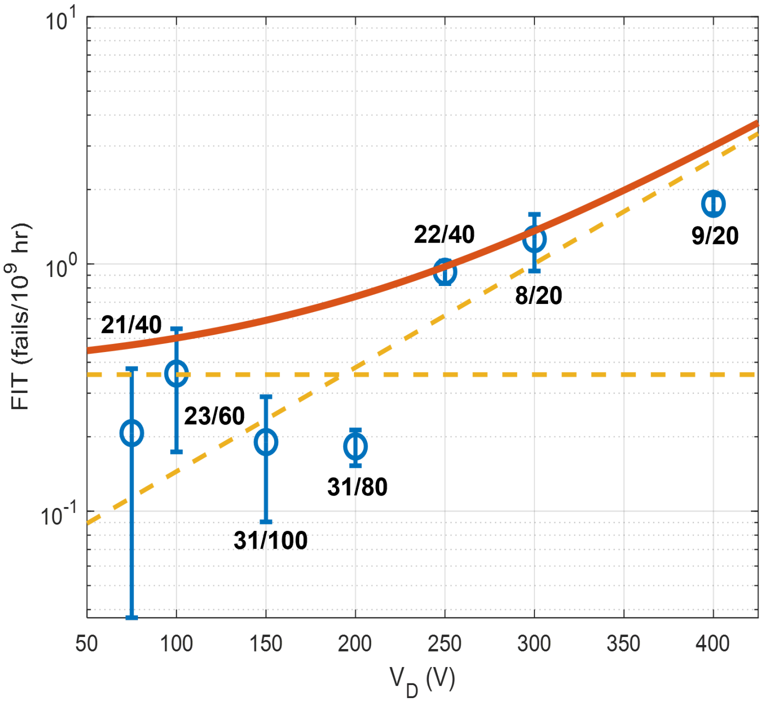

Figure 4.11: Drain voltage dependent FIT. Orange dash lines are the fitting curves with the 95% confidence level. Red solid line is the summation of the two individual fitting curves. Error bars represent a 95% confidence level. Number of tested devices/Number of failures for each condition are shown.

point, increases in drain voltage increase the failure rate. At 95% confidence, the failure rate at 400 V is approximately 2 FIT in the terrestrial neutron environment at sea-level NYC conditions. This GaN HEMT technology offers sufficient neutron reliability tolerance for most terrestrial power applications @ 400 V. This result suggests that GaN HEMT radiation robustness is as good, or better than, the robustness observed with similarly-irradiated SiC transistors [61], [62], [63] and [64]. Note that SiC transistors have higher operation voltages compared with our samples.

4.2.2 Post-Radiation Characterization

In order to have a better understanding of neutron radiation-induced damage in GaN HEMTs, post-radiation characterizations were carried out, which consisted of IV sweeps ($V_D = 0.1$ V, V_G swept from -14 V to 0 V) and DC stress ($V_D = 150$ V, $V_G = -14$ V). Gate

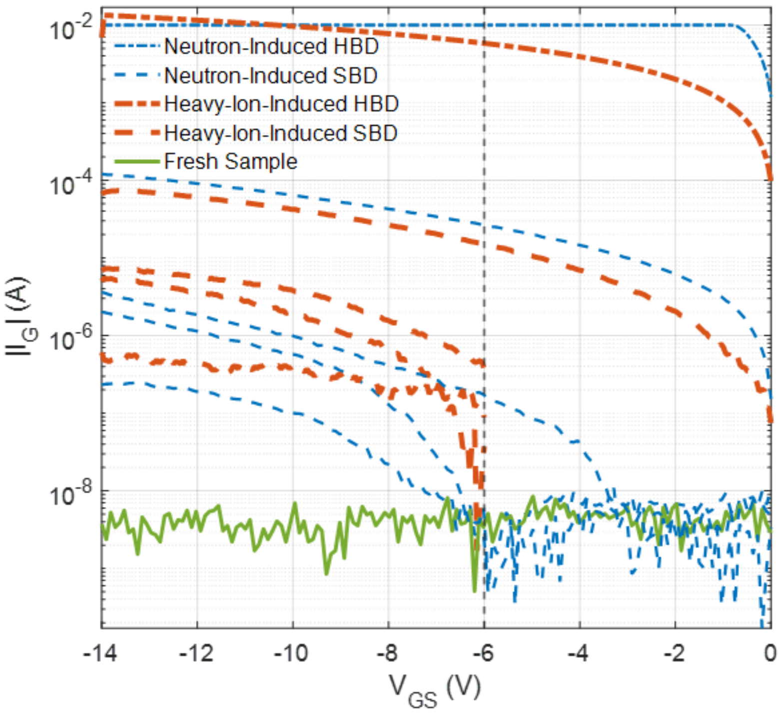

Figure 4.12: Select post-breakdown characterization results showing the similarity in neutron and heavy-ion induced SBD and HBD events. For neutron experiments, V_{GS}=-14 V, V_{DS}=75-300 V. For heavy-ion experiments, V_{GS}=-14 V, V_{DS}=300-480 V, and LET ranges from 5 to 9 MeV·cm^2/mg (Si). Each condition contains data from multiple DUTs.

dielectric degradation, including radiation-induced soft breakdown (SBD) and radiation-induced hard breakdown (HBD) were observed, where soft breakdown was characterized by an abnormal increase in gate leakage, with transistor action still observed, while hard breakdown was characterized by high gate and drain leakage and a catastrophic loss of transistor action (a short from gate to drain or gate to source). Note that, the post-breakdown IV behaviors as we observed in low LET heavy-ion radiation experiments on the same type of device, as shown in Fig. 4.12, which further illustrates our hypothesis that neutron-induced secondary particles play an important role in dielectric degradation.

The leakage paths for all radiation-induced SBDs and most radiation-induced HBDs are from drain to gate, except for one device that exhibited a radiation-induced HBD from source to gate. This preponderance of drain side failures is consistent with the TCAD simulation results previously presented, which is attributed to the high electric fields at the drain side of the dielectric. The fact that both radiation-induced SBD and radiation-induced HBD form a permanent conduction path inside the dielectric, with a relatively constant impedance, implies the possibility that radiation-induced SBD and radiation-induced HBD share a common statistical and physical origin [28], [55], [54].

To further illustrate the radiation-induced HBD dependence on drain voltage stress, we introduce the radiation-induced HBD probability P_{RHB}, defined as:

$$P_{RHB} = \frac{N_{RHB}}{N_{tot}} \tag{4.3}$$

where N_{RHB} is the number of radiation-induced HBD. N_{tot} is the total sample number tested under radiation. Fig. 4.13 shows the normalized P_{RHB} under different bias conditions. As with the earlier data, this plot suggests that the physical mechanism causing hard breakdown requires a drain stress of 200V or more. No drain to source shorts (without dielectric breakdowns) were observed indicating that SEGR always occurred whether or not SEB-type events occurred.

For each drain bias, the total number of radiation-induced SBD and radiation-induced HBD events is smaller than the cumulative failure number we recorded during neutron radiation, especially for drain voltages below 200 V. In other words, based on the failures observed during irradiation, the number of devices exhibiting breakdown based on I-V characterization was lower than expected. There are three possible explanations:

1. Transients triggered a false breakdown. The sensing module was looking for current excursions above a compliance limit - a transient caused by a big event could have triggered the detection of a breakdown. Since the sense circuit removes the device from stress immediately upon detection of the event, perhaps some large single event transients (SETs) were captured instead of actual breakdown events. The system is being redesigned to add an RC delay that will require the high current state to persist for milliseconds to mitigate false events induced by big SETs.

2. Positive charge trapping in the gate dielectric during irradiation caused a virtual gate to form which partially turned on the channel and caused the sensing module to trigger

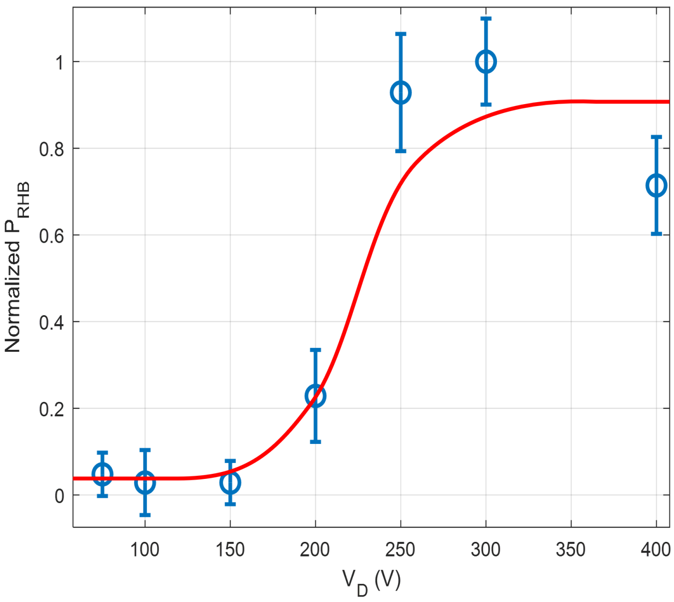

Figure 4.13: Normalized radiation-induced HBD probability ratio P_{RHB} vs. Drain voltage V_D. Blue dots are the data points. The red line is simply to guide the eye. Error bars represent a 95% confidence level. P_{RHB} indicates a degradation threshold voltage around 200 V.

an event. This effect has also been observed during heavy ion experiments and recovers over time.

3. Annealing effects caused by the long delay (necessitated by neutron activation of our samples, which were not available until 6 months after the experiments) between neutron experiments and IV analysis of individual devices. In this case, the anneal could allow recovery, or the prior mechanism (virtual gate effect), and/or the recovery of soft breakdowns. To address this, in future studies we plan to bring additional equipment so that IV measurements can be performed on failing units immediately after they fail.

In addition to radiation-induced effects, the I-V measurements also revealed evidence of current collapse in many of the devices. Current collapse is a well-known effect in GaN HEMTs and refers to the phenomenon of increased "ON" channel resistance R_{DSon} (decreased on-state I_{DS}) [65]. Fig. 4.14 shows a typical IV curve of a device that exhibited current collapse. This degradation occurred at all stress levels and was seen in devices that had not broken down. Unlike radiation-induced SBD and HBD, current collapse does not show strong drain voltage dependence, but has a significant dependence on neutron fluence, which can be explained by two hypotheses, including: 1) neutron-induced displacement damage reduced the electron density inside the 2DEG channel, which requires a significant amount of displacement damage at the AlGaN/GaN interface, or 2) part of the energetic electrons generated by neutron-induced secondary particles are trapped in the dielectric above the 2DEG channel and form the virtual gate effect, which depletes the 2DEG channel and reduces the saturation current. Further investigations are necessary to understand this failure mechanism. Note that SEGR characterization results would not have been directly impacted by this effect (since the DUT sensing modules were designed to detect signs of high leakage, not reduced leakage, so this effect would not have triggered any false breakdown events) and the calculated failure rates due to neutron effects are believed to be independent of it.

Overall, the D-mode GaN HEMT devices showed neutron-induced gate dielectric degradation, which caused increased leakage in many failed samples, and catastrophic breakdown in a few of the failed devices. The failures are consistent with SEGR, which is closely related to the electric field transients generated by neutron-induced secondary particles. The size and duration of electric field transients induced by secondary ions have the same dependence upon injection location in the device, ion LET, and applied V_{DS} as demonstrated in the Chapter 3 section "Device Simulation Analysis".

4.3 Neutron-Induced Secondary Particle Production

The secondary particles produced by neutrons inside GaN HEMTs were simulated using Geant4, a Monte Carlo tool that simulates nuclear reactions at a target based on incident radiation, in our case, the LANSCE neutron beam [66]. Detailed information about the Python-based Geant4 is given in Appendix 6. To estimate the worst-case for neutron-induced damage, two different targets were defined, representing two main material stacks that exist in the actual device. A diagram of the two device stacks is shown in Fig. 4.15. These ignore the ultrathin AlGaN layer but otherwise include actual layer thicknesses of the GaN HEMTs that were tested. A parallel neutron “beam” perpendicular to the device

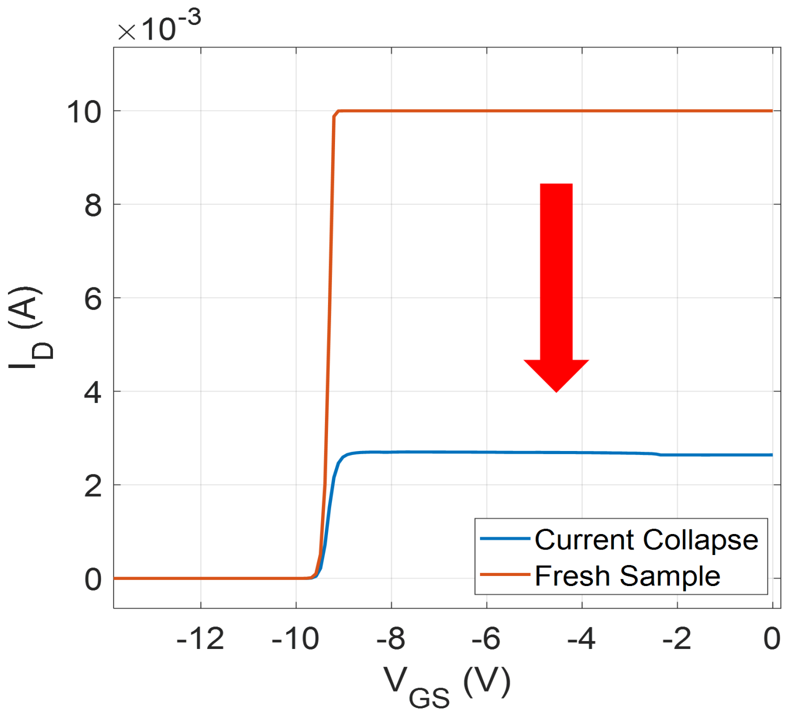

Figure 4.14: Typical I-V curves demonstrating drain current collapse effect. Drain voltage equals 0.1 V with a drain current limit of 10 mA.

surface was injected with the LANSCE neutron energy spectrum. The pre-packaged physics list QGSP_BIC_HP including the hadronic and electromagnetic physics was enabled, using a high precision neutron model for neutrons below 20 MeV and a binary cascade model for neutrons above 20 MeV [67]. Information of every single secondary particle generated inside the sensitive region (marked by green rectangular in Fig. 4.15) was recorded, including initial energy, location, direction, etc. The specific LET of each secondary particle calculated by Geant4 was then determined using SRIM simulations. A comparison between both structures revealed that terrestrial neutrons generated more secondary particles in structure (a) and that the maximum LET distribution was similar. Thus, structure (a) was selected as the "standard" for this study.

One hundred simulations were performed for a total of two billion neutrons, enabling an accurate extrapolation of the terrestrial neutron-induced secondary particle spectrum. In our irradiation experiments, the GaN HEMT DUTs started exhibiting failures at a neutron

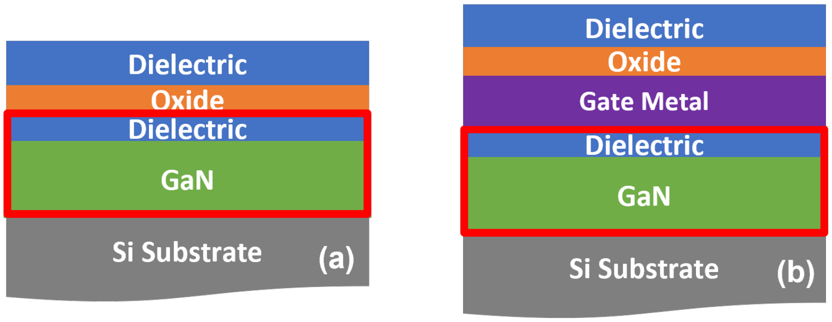

Figure 4.15: Cross-section of simulated HEMT structures used in Geant4. Each material layer has the same thickness as the actual device. The green rectangle marks the sensitive region. The neutron beam was injected perpendicularly from the top to the bottom of the device.

fluence of $1{\times}10^9$ n/cm^2, hence the simulated spectra that represent a physical fluence of $2{\times}10^9$ n/cm^2 should be an accurate representation of the spectra that the devices were exposed to, and the LET spectra they were sensitive to.

Table 4.3 shows the results of our simulations, including secondary particle types, corresponding maximum LET reported in silicon (for equivalency to silicon results) and in GaN for correctness, their relative probabilities P_{se} (determined by the number of observed secondaries of a specific type, n_p, divided by the total number of neutrons, n_0) and corresponding standard deviations. Notice that, each secondary particle type consists of different types of ions. As expected, gallium and nitrogen are the main secondary particles generated by neutrons inside the sensitive region, with the maximum LET around 14 MeV·cm^2/mg (Si). Secondary particles like Cu, Co, and Mn have the maximum LET reaching 20 MeV·cm^2/mg (Si). However, the probabilities of the secondary particles are small, which could be one of the reasons for the fact that most radiation-induced SBD and HBD happened at high neutron fluence.

The blue histogram in Fig. 4.16 (b) shows the overall neutron-induced secondary particle LET spectrum in gallium nitride: LET (GaN), which includes every secondary particle type predicted by Geant4. We also calculated an LET spectrum in silicon: LET (Si), as shown in Fig. 4.16 (a). The standard deviation error bars were too small to be visible in the histogram. The integrated number of events for each LET value (integration from high LET

Table 4.3: Summary of neutron-induced secondary particles in GaN HEMTs.

Name	Max LET (Si)[a]	Max LET (GaN)[a]	P_{se}	P_{se} SD
Ga	13.8	10.9	7.35×10^{-5}	1.82×10^{-8}
H	0.5	0.4	6.74×10^{-5}	2.12×10^{-8}
N	6.1	4.8	3.91×10^{-5}	1.63×10^{-8}
He	1.5	1.2	1.83×10^{-5}	1.42×10^{-8}
Si	14.0	11.1	1.13×10^{-5}	9.93×10^{-9}
Zn	15.6	12.4	6.21×10^{-6}	7.46×10^{-9}
C	5.2	4.1	4.64×10^{-6}	5.43×10^{-9}
B	4.2	3.3	3.95×10^{-6}	4.64×10^{-9}
O	7.3	5.8	2.43×10^{-6}	4.20×10^{-9}
Cu	20.3	16.1	1.97×10^{-6}	3.39×10^{-9}
Al	12.5	9.9	1.72×10^{-6}	4.86×10^{-9}
Li	2.3	1.8	1.58×10^{-6}	4.00×10^{-9}
Ni	19.8	15.7	1.35×10^{-6}	3.65×10^{-9}
Mg	11.9	9.4	8.63×10^{-7}	3.71×10^{-9}
Ge	5.3	4.2	6.46×10^{-7}	2.49×10^{-9}
Co	21.9	17.4	4.66×10^{-7}	2.22×10^{-9}
Be	3.2	2.6	4.27×10^{-7}	1.93×10^{-9}
Na	10.8	8.6	2.53×10^{-7}	1.67×10^{-9}
Fe	19.6	15.6	2.04×10^{-7}	2.94×10^{-9}
Ne	9.2	7.3	1.31×10^{-7}	1.29×10^{-9}
Mn	20.3	16.2	8.40×10^{-8}	8.00×10^{-10}
Cr	20.4	16.3	7.80×10^{-8}	1.17×10^{-9}
F	8.5	6.7	3.35×10^{-8}	5.10×10^{-10}
Sc	17.4	13.8	7.50×10^{-9}	2.40×10^{-10}
Ca	10.9	8.6	4.50×10^{-9}	2.00×10^{-10}

[a] Unit is MeV·cm^2/mg.

to the specific x-axis LET value) is shown in Fig. 4.16 (red curve). Basically, corresponding LET values of terrestrial neutron-induced secondary particles in GaN HEMT range from 0 to 22 MeV·cm^2/mg (Si) / 12 MeV·cm^2/mg (GaN). In heavy-ion studies on the same devices, we observed SEGR failure with ions as low as LET=3 MeV·cm^2/mg (Si). It was observed that higher LETs produced more damage with much lower fluence. In other words, the higher the LET of the ion the lower the fluence-to-failure needed (by SEGR). There appears to be an LET-dependent damage continuum for SEGR in the dielectric. This is consistent with the fact that higher LET events will deposit a higher charge density, which will produce larger peak transient electric fields due to the higher charge injection.

Overall, the LET range of neutron-generated secondary ions in GaN was monotonically decreasing (lower LET events are more common than higher LET events) from an LET of 0 to 12 MeV·cm^2/mg (GaN) corresponding to a LET range of 0 to 22 MeV·cm^2/mg (Si) equivalent.

4.4 Discussion

Based on the Geant4 simulation results, more than 15,000 secondary particles are generated inside the GaN HEMTs with LETs $\geq$ 10 MeV·cm^2/mg (Si) after being irradiated with $2{\times}10^9\ n/cm^2$ neutrons. According to the TCAD simulation results, when these secondary particles strike the A_{sen}, they are able to generate an electric field transient reaching or exceeding the E_{BD}. Secondary particles with LET values lower than 5 MeV·cm^2/mg (Si), may not be able to create enough defects to initiate destructive SEEs in a GaN HEMT by a single strike. But defects generated along their injection tracks can reduce the dielectric breakdown field E_{BD}. Thus, for the D-mode GaN HEMTs irradiated with a given terrestrial neutron fluence f_n, the corresponding probability failure rate P_{FIT} can be estimated by the following equation:

$$P_{FIT} = \int_{LET_{min}}^{LET_{max}} \frac{P_{LET}(f_n) \cdot A_{sen}(LET) \cdot P_{BK}(LET)}{A_{Device}} dLET \tag{4.4}$$

where P_{LET} is the probability of generating a secondary particle with LET equal to a given value (from LET_{min} to LET_{max} MeV·cm^2/mg (Si)), which is able to generate an electric field transient reaching the dielectric breakdown field. In our case, LET_{min} equals 5 and LET_{max}

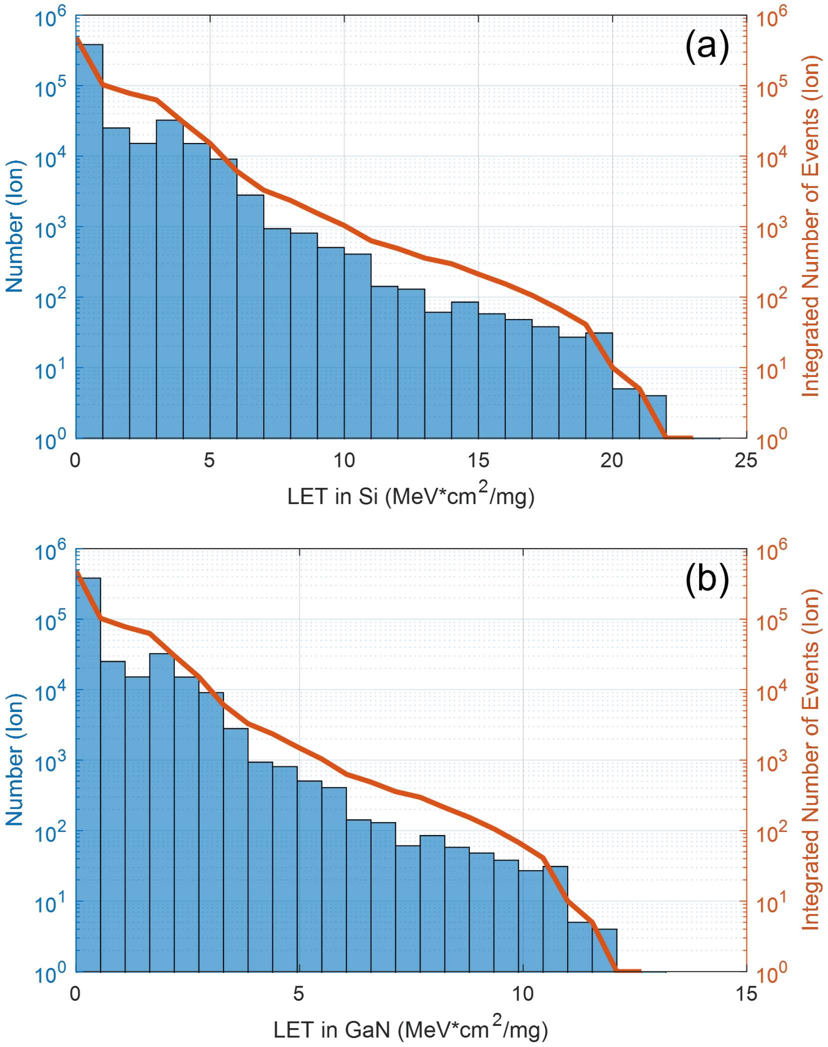

Figure 4.16: Secondary particle LET spectrum generated by neutrons in GaN HEMTs. Results for silicon are shown in (a) and for GaN in (b). The effective neutron fluence for each simulation was 2×10^9 n/cm^2, which was of the same order as the fluence used in the neutron testing.

equals 22. A_{sen} is the sensitive region area for the given LET value. A_{Device} is the device area. P_{BK} is the dielectric breakdown probability when stressed under a certain electric field E, which is a function of secondary particle LET. In reality, P_{BK} can be estimated based on time-dependent gate oxide breakdown (TDDB) experimental results of the dielectric material. Then we can have the worst-case failure rate P_{FITMax} under neutron fluence f_n:

$$P_{FITMax} = 17 \cdot \frac{P_{LET=22}(f_n) \cdot A_{sen}(LET = 22) \cdot P_{BK}(LET = 22)}{A_{Device}} \tag{4.5}$$

And the corresponding minimum failure rate P_{FITMin}:

$$P_{FITMin} = 17 \cdot \frac{P_{LET=5}(f_n) \cdot A_{sen}(LET = 5) \cdot P_{BK}(LET = 5)}{A_{Device}} \tag{4.6}$$

The fact that both heavy-ion-induced SEGR and neutron-induced SEGR have similar post-breakdown IV behaviors indicates common physics mechanisms behind the failures. However, in our neutron experiments we did not monitor the terminal current, so it is unknown whether neutron-induced SEGR also has a similar multistage degradation process, to what we observed in heavy-ion experiments. In future work, we will do real-time current monitoring in neutron irradiation experiments. Further, current collapse was observed to be a common failure induced by neutron radiation, which was unexpected. There are 100 out of 300 devices that only experienced current collapse. Specific experiments will be designed and carried out in future neutron irradiation experiments.

Chapter 5

Discussion

5.1 Multiple-impact hypothesis vs. Single-strike hypothesis

A certain number of ion strikes was required to initiate dielectric degradation both in neutron irradiation experiments (most failures happened after 1×10^9 n/cm^2 effective neutron fluence as shown in Fig. 4.9) and in heavy-ion irradiation experiments (moderate field strength and heavy-ion LET, no breakdown before $1{\times}10^6$ ion/cm^2 as shown in Fig. 3.12). Similar phenomenon has also been reported by Johnston *et al.*, which can be interpreted in two ways [53]:

- Multiple-impact hypothesis: The dielectric is gradually weakened by ion strikes (precursor damage accumulation process), only valid when a single heavy ion strike cannot induce a strong enough electric field transient and generate an efficient number of defects inside the dielectric.

- Single-strike hypothesis: Localized regions exist inside the dielectric, which are more sensitive to heavy-ion-induced effects. Dielectric degradation is initiated by an ion strike near sensitive regions. A particle with a higher LET value has a larger sensitive region area.

In both cases, the dielectric degradation process is initiated by a single ion strike. The essential difference between the two hypotheses is the origin of sensitive regions, intrinsic or stress (both radiation and electric stress) induced. In other words, the multiple-impact hypothesis requires at least double ion hits within a small area, in which defects generated by multiple heavy ions form a conduction path through the dielectric. Based on our data, we believe the multiple-impact hypothesis is the dominant mechanism for particles with low LET values. A single particle with a low LET value cannot generate enough defects inside the dielectric to initiate the degradation process, which might be because E_{peak} of the electric field transient is too low or t_{peak} of the electric field transient is too short. However, when another low LET particle is injected around the same location, the total defect density induced by both incident particles might reach the critical defect density of the dielectric, and a breakdown event will occur. For high LET particles, the single-strike hypothesis is the dominant failure mechanism, as a high LET particle can induce a strong electric field transient and generate a significant number of defects inside the dielectric when it strikes the sensitive region of the device. That is to say, a single incident particle can initiate a breakdown event in a brand new device when it hits the right spot, e.g., radiation-induced HBDs without any pre-SBDs as shown in Fig. 5.1. Overall, particles with low LET values have much higher F_{crit} and F_{fail} compared with high LET particles. In other words, with the same effective fluence, high LET particles will induce a significantly higher off-state gate leakage than low LET particles, which is consistent with our experimental data.

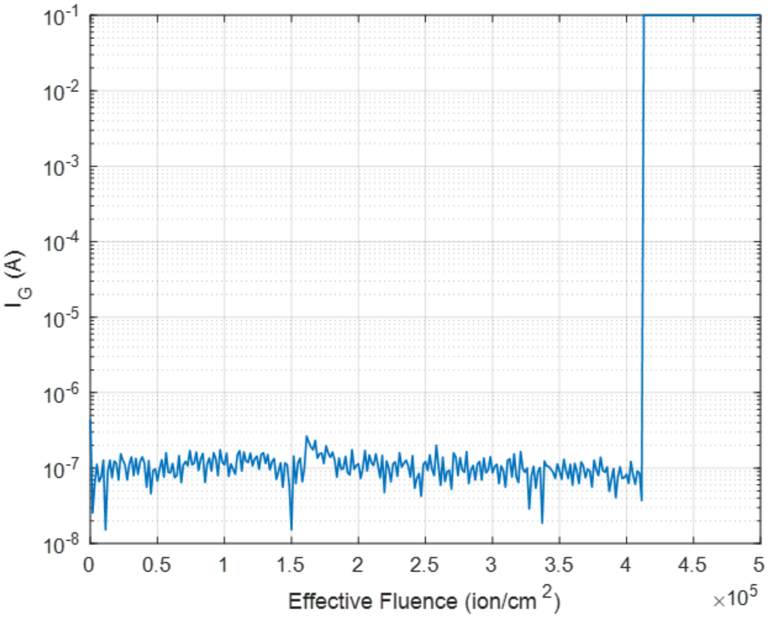

Figure 5.1: An example of heavy-ion-induced single event gate rupture. DUT was irradiated under 944-MeV Cu ions with an equivalent LET of 22 MeV·cm^2/mg (Si). V_{GS}=-14 V, V_{DS}=50 V, and flux=10^5 ion/cm^2·s. DUT experienced a radiation-induced HBD without any pre-SBD.

To further understand whether multiple ion strikes are related to dielectric degradation, we describe a statistical model, which is based on the approach proposed in [43]. First, we consider a device area S exposed to heavy ion radiation. The impact area of each particle is α, which is the average damage area produced by a single incident particle, and $\alpha \ll S$. α is a function of bias condition and particle LET. In this case, the total cell number n equals to S/α. We define a double hit or more occurs on one cell as one event. During our experiments, heavy ions were uniformly distributed within the beam aperture, thus we consider each cell has the same probability of being hit by an ion. For simplicity, we assume the defect lifetime is much longer than the radiation time, in other words, no annealing of defects. Then, the probability of no event, when total effective fluence equals F, can be calculated by the following equation:

$$P(x=0) = \prod_{i=1}^{k}(1-\frac{i-1}{n}). \tag{5.1}$$

where k is the total ion number received by the device and equals $S \cdot F$. x is the number of multiple impact events. Then, the probability that at least one event happens is straightforward:

$$P(x \geq 1) = 1-\prod_{i=1}^{k}(1-\frac{i-1}{n}). \tag{5.2}$$

The diameter of the ion injection track (funnel-like plasma filament) typically ranges from tens to hundreds of nm [23]. Due to charge redistribution, α should be larger than the cross-sectional area of the ion injection track. Therefore, three different α values (0.1 μm^2. 1 μm^2, 10 μm^2) were selected to validate the statistical model. Fig. 5.2 shows the corresponding $P(x \geq 1)$ of different α values with effective fluence up to 1×10^6 ion/cm^2. Note that, S was estimated based on the actual gate area of tested D-mode GaN HEMTs ($S \gg$10 μm^2). At least one multiple-impact event will occur at 1×10^6 ion/cm^2 even with the smallest impact area 0.1 μm^2, which is consistent with the fact that the mean critical fluence F_{crit} equals 1.1×10^6 ion/cm^2 with V_{DS}=150 V, V_{GS}=-14 V, and LET=15 MeV·cm^2/mg (Si), as presented in Table 3.3. The corresponding α of a given bias condition and particle LET can be estimated based on the fluence to failure experimental data.

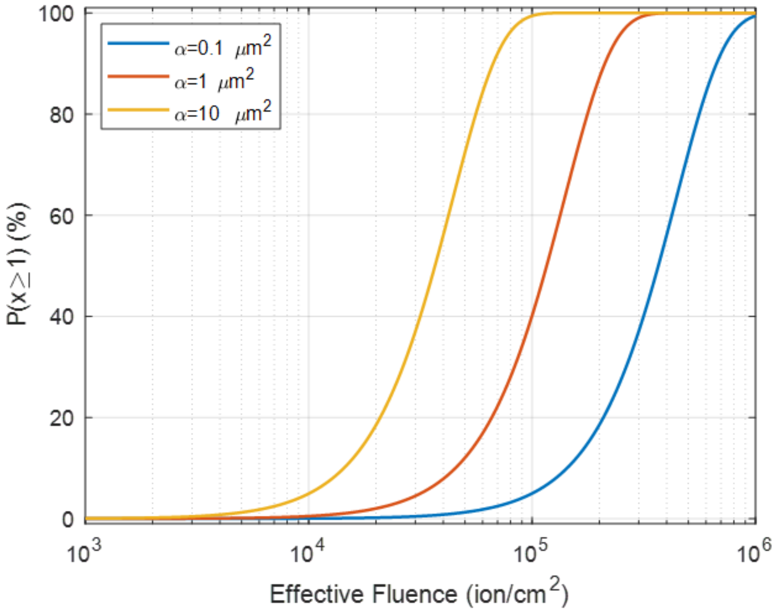

Figure 5.2: Probability of at least one event ($x \geq 1$) as a function of effective fluence, with the area size S estimated from our device. At least one event will happen at 1×10^6 ion/cm^2 for all three impact areas.

Furthermore, the probability of a given cell i being hit by at least two ions can be calculated by:

$$P_i(y \geq 2) = 1 - (\frac{n-1}{n})^{k-1}. \tag{5.3}$$

where y is the number of ions striking the ith cell. We can also use expectation, $E[P_i(y \geq 2)]$, to estimate the number of the cells impacted by at least a double hit, as the total cell number is large:

$$E[P_i(y \geq 2)] = n \cdot P_i(y \geq 2). \tag{5.4}$$

Fig.5.3 shows the corresponding $P_i(y \geq 2)$ with different impact area sizes. At 1×10^6 ion/cm^2 fluence, the corresponding probabilities for three impact areas (0.1 μm^2. 1 μm^2, and 10 μm^2) are 0.1%, 1.0%, and 9.8%. Given the device area is 0.01 cm^2, then the corresponding number of the cells impacted by at least a double hit for three impact areas are given in

Fig.5.4, which are on a similar level due to the fact that a smaller impact area has a larger total cell number. When the effective fluence equals 1×10^6 ion/cm^2, more than 10^4 cells experienced at least one multiple-impact event. We assume the defect lifetime is much longer than the radiation time, which might be invalid in actual experiments ($P(x \geq 1)$ and $P_i(y \geq 2)$ are slightly lower in reality). Overall, our model provides a solid statistical basis for the multiple-impact hypothesis.

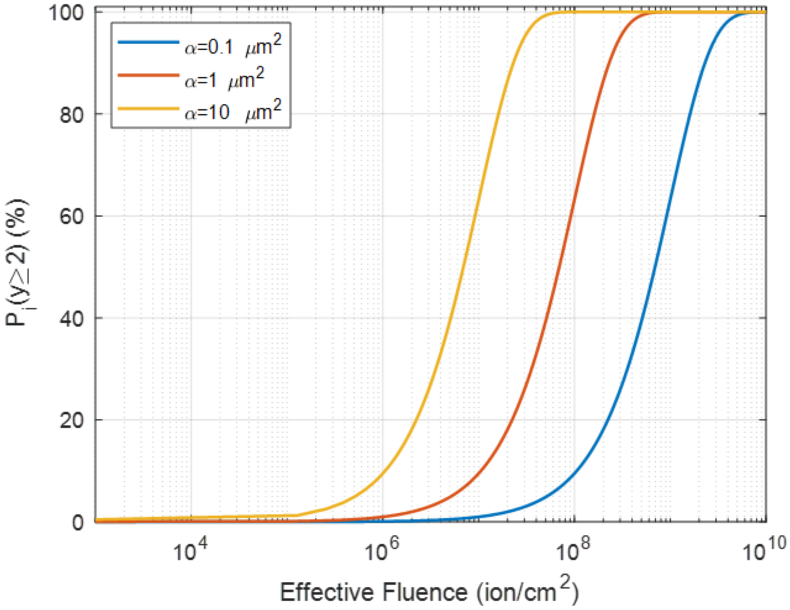

Figure 5.3: Probability of at least 2 ion hits on ith cell as a function of effective fluence, with the area size S estimated from our device. Maximum effective fluence is 1×10^{10} ion/cm^2. At 1×10^6 ion/cm^2 fluence, the corresponding probabilities for three impact areas (0.1 μm^2. 1 μm^2, and 10 μm^2) are 0.1%, 1.0%, and 9.8%.

Specific experiments were designed to further illustrate the multiple-impact hypothesis, including ultra-low LET irradiation experiments and fluence to failure experiments with a 10 mA current injection level. In the ultra-low LET irradiation experiments, DUTs were irradiated under 300-MeV Ne radiation (LET=4 MeV·cm^2/mg (Si), flux=1×10^5 ion/cm^2·s)

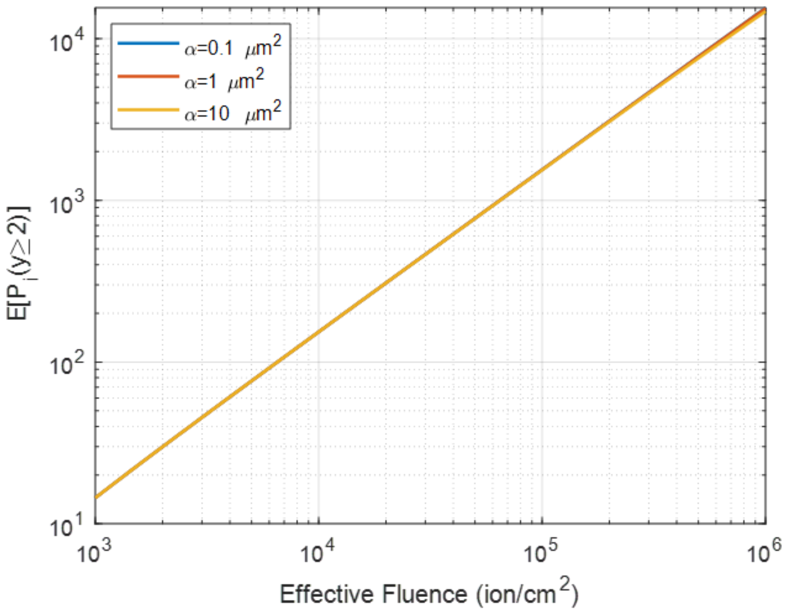

Figure 5.4: Expectation of at least 2 ion hits on ith cell as a function of effective fluence, with the area size S equal to 0.1 cm^2. Maximum effective fluence is 1×10^6 ion/cm^2. The fact that a smaller impact area has a larger total number of cells, causes the three curves to overlap. At 1×10^6 ion/cm^2, a significant amount of cells experienced at least one multiple-impact event.

until a breakdown event happened (V_{GS}=-14 V and V_{DS}=500 V). Fig. 5.5 shows an example of the heavy-ion-induced SBD observed in ultra-low LET irradiation experiments.

Corresponding TCAD simulations were carried out with the same bias conditions, in which a 4 MeV·cm^2/mg (Si) particle was injected at Loc4. Simulation results are shown in Fig. 5.6 and Fig. 5.7. Theoretically, based on the single-strike hypothesis (without precursor damage dependence), no dielectric breakdown event should be triggered as the maximum E_{peak} is below the dielectric breakdown field E_{BD} and the electric field transient time is too short, which is contrary to the experimental data. In other words, a significant amount of stress time is required to break down the dielectric when the applied electric field is below E_{BD}. Therefore, the radiation-induced SBD events observed in ultra-low LET irradiation experiments are due to precursor damage accumulation inside the dielectric, which leads to a reduction in the breakdown field, E_{BD}.

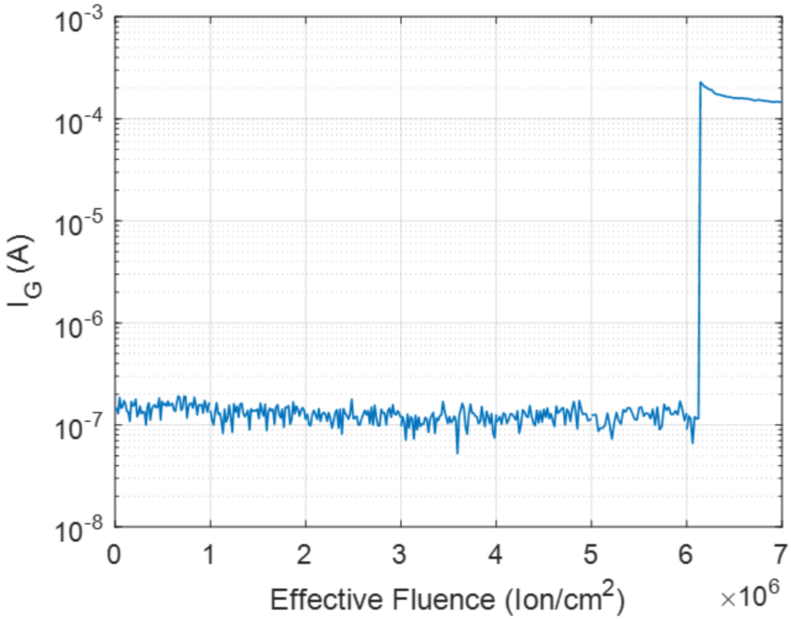

Figure 5.5: An example of the heavy-ion-induced SBD observed in ultra-low LET irradiation experiments. V_{GS}=-14 V (off-state), V_{DS}=500 V, flux=1×10^5 ion/cm^2·s, and LET=4 MeV·cm^2/mg (Si). A radiation-induced SBD happened around 6×10^6 ion/cm^2, which was related to precursor damage accumulation.

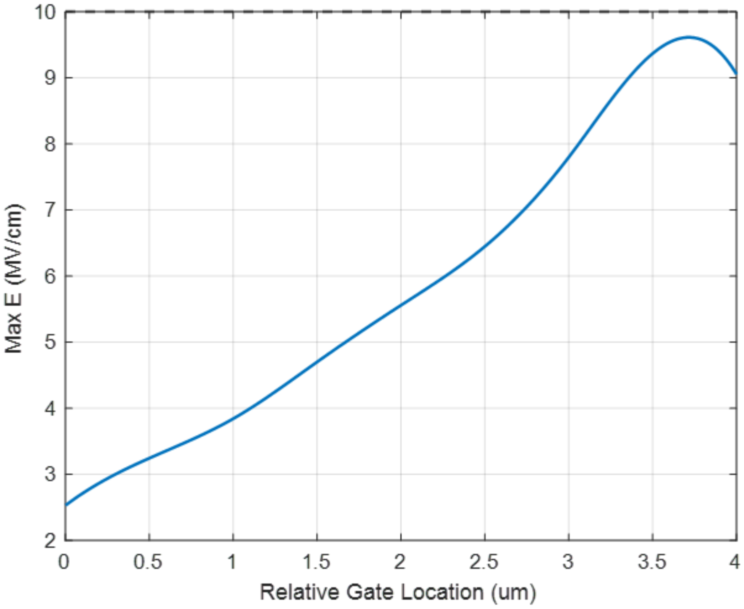

Figure 5.6: E_{peak} plotted as a function of position along the gate. The injection location is Loc4. V_{GS}=-14 V (off-state), V_{DS}=500 V, and LET=4 MeV·cm^2/mg (Si). The maximum E_{peak} is slightly below the breakdown field E_{BD}.

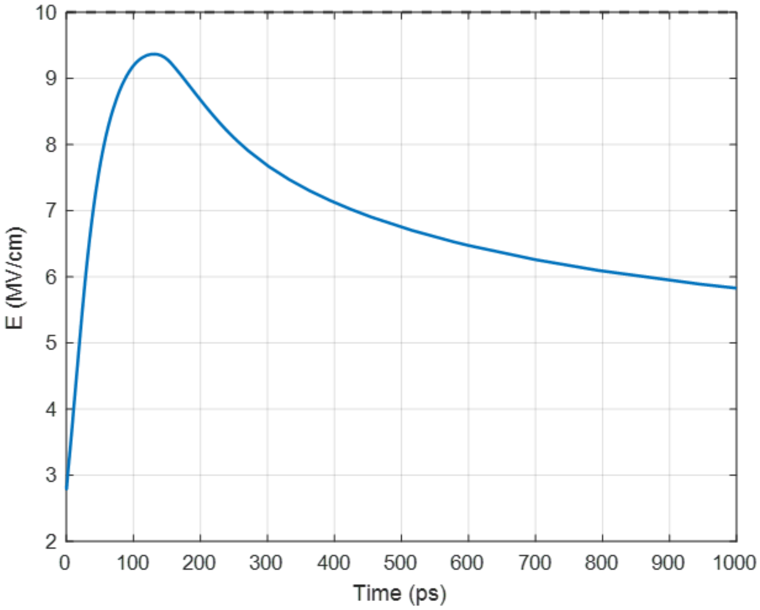

Figure 5.7: Electric field variation as a function of time for the 3.5 μm sensing probe of the ultra-low LET irradiation experiment. Total simulation time is 1000 ps. The injection location is Loc4. V_{GS}=-14 V (off-state), V_{DS}=500 V, and LET=4 MeV·cm^2/mg (Si). The strongest electric field transient induced by 4 MeV·cm^2/mg (Si) particles is below E_{BD}.

In fluence to failure experiments, DUTs were continuously irradiated with 599-MeV Ar (flux=1×10^5 ion/cm^2·s, LET=10 MeV·cm^2/mg (Si)) until the first breakdown event (radiation-induced SBD or HBD) happened with I_S=10 mA, V_G=-14 V, and V_{DS}=150 V. As discussed in Chapter 3, injection of 10 mA current through the 2DEG channel significantly attenuates heavy-ion-induced electric field transients (as shown in Fig. 3.31), which are unable to initiate any breakdown event in the dielectric based on the single-strike hypothesis. However, as shown in Fig. 5.8, radiation-induced SBD was observed, indicating the gate dielectric was gradually weakened by heavy-ion strikes.

In general, our experimental data and simulation results support the idea that both multiple impact effects and single event effects are closely related to radiation-induced gate dielectric breakdown (SBD and HBD).

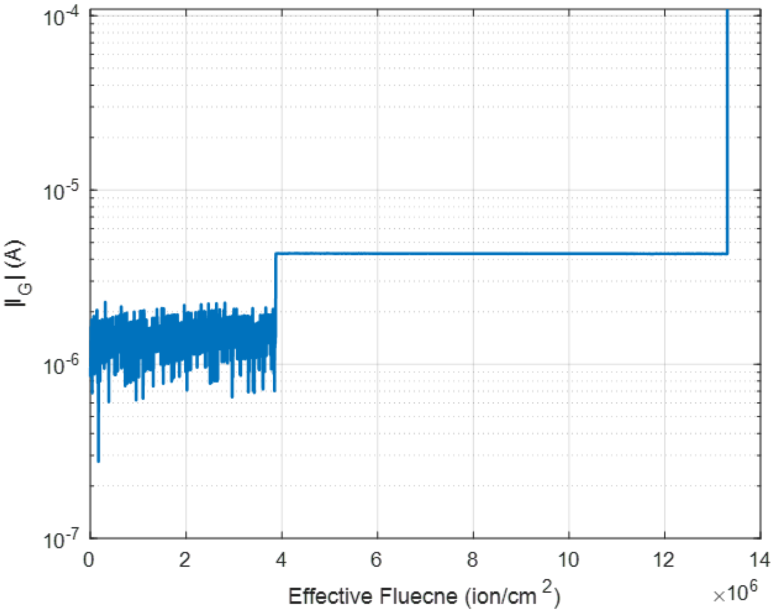

Figure 5.8: An example of radiation-induced SBD in fluence to failure experiments with a 10 mA current injection level. 599-MeV Ar (LET=10 MeV·cm^2/mg (Si)) is used with flux equal to 1×10^5 ion/cm^2·s. V_G=-14 V and V_{DS}=150 V. The soft breakdown that happened at the end of experiments is related to multiple impact effects.

5.2 Percolation theory-based gate dielectric degradation model

As previously discussed, neutron-induced gate dielectric breakdown and heavy-ion-induced gate dielectric breakdown share common failure mechanisms, which are closely related to particle-induced electron-hole pairs. To further investigate the physical mechanism behind the radiation-induced dielectric breakdown in GaN HEMTs, a universal framework to model the time-dependent dielectric breakdown (TDDB) process was adapted, given by equation 5.5, which characterized the influence of each component we studied such as E_{peak}, F_{BD} and t_{peak} [32], [53].

$$t_{BD} = \frac{N_{BD}}{P_{gen1} + P_{gen2} + P_{gen3}} \approx \frac{N_{BD}}{P_{gen1} + P_{gen2}} \tag{5.5}$$

where N_{BD} is the critical defect density, which is related to intrinsic defect density, dielectric area A_{diel}, or F_{BD} in our case, and dielectric thickness t_{diel}. P_{gen1} is the defect generation rate due to radiation-induced carrier injection inside the dielectric, which depends on the peak electric field E_{peak}, stressing area F_{BD}, temperature T, and t_{diel}. P_{gen2} is the defect generation rate due to injected particle direct interaction with the material, which is mainly related to particle LET. P_{gen3} is the defect generation rate due to electric stress, which is affected by V_{GS} and V_{DS}. Note that, P_{gen3} is far less than the other two mechanisms because the device voltage acceleration factor is low and the experiments only last several hours so there is insufficient time for significant degradation via this process. Thus, P_{gen3} can be ignored as shown in equation 5.5. Apparently, t_{peak} plays an important role in SEGR response, because without enough stressing time, dielectric degradation may not occur because of insufficient defect density. However, as previously discussed, particles that are unable to initiate a breakdown event in GaN HEMTs, also contribute to dielectric degradation by generating new defects, which may reduce the critical defect density N_{BD}. In general, it appears that defects generated either by carrier injection (electric field transient) or particle interactions (displacement damage) are responsible for radiation-induced dielectric breakdowns in GaN HEMTs. When an energetic particle generates enough defect density ($\geq N_{BD}$) inside the dielectric (including or excluding precursor damage), a breakdown event will be triggered. Compared with radiation-induced SBD, radiation-induced HBD has a higher critical defect density and a lower relative conduction path resistance.

Based on the breakdown framework, we further proposed a percolation theory-based gate dielectric degradation model, which is based on the simple percolation approaches proposed in [55], [68]. Both multiple impact effects and single event effects are involved with this defect-assisted breakdown model. As previously discussed, electrical stress and radiation particle interactions create defective cells. Particles with higher LET values can generate more defects along the injection track. When the spacing between defective cells becomes smaller, dielectric breakdown events will occur as current conduction paths are formed inside the dielectric. Conduction paths with higher defect densities have higher leakage current levels.

Fig. 5.9 shows a two-dimensional schematic of the model, which consists of $N \times M$ cells. N is the total number of columns, which is proportional to the device area. M is the total number of cells per column, representing the dielectric thickness. Fig. 5.9 (a) demonstrates the defect generation due to electrical stress and radiation effects. A radiation-induced SBD is shown in Fig. 5.9 (b), which is initiated only by one incident particle (single event effect). A radiation-induced HBD with precursor damage dependence (multiple impact effects) is shown in Fig. 5.9 (c). Radiation-induced HBD needs higher defect density to be triggered than SBD.

Monte Carlo simulations have been carried out to further illustrate this model. The failure probability of each cell is defined as $\lambda(E, \text{LET}, n_s)$, which is a function of the electric field strength E, incident particle LET, and the number of surrounding defects. Note that, we assume cells next to defects have higher failure probabilities when hit by incident particles compared to other cells. Then $\lambda(E, \text{LET}, n_s)$ can be calculated by the following equation:

$$\lambda(E, LET, n_s) = \eta(P_{Rad}(LET) + P_{Neigh}(n_s)) + P_{Elec}(E) \tag{5.6}$$

where P_{Rad} is the failure probability due to radiation, P_{Neigh} is the additional failure probability due to surrounding defects, and $P_{Elec}(E)$ is the failure probability related to electrical stress. η is an indicator parameter, equal to 1 when hit by an incoming particle, and equal to 0 otherwise. The seam finding algorithm is used to find the formed conduction paths [69], as shown in Fig. 5.10, which has two parameters: maximum conduction gap and searching width. Maximum conduction gap is the maximum cell gap number between two defective cells that allows charge conduction. Searching width is the number of neighboring cells that can form a conduction path. An example of the Monte Carlo simulation results is shown in Fig. 5.11. A 3000×100 matrix was defined, which represented a thin layer gate dielectric. A total of 3000 particles were randomly injected into the dielectric following a uniform distribution. Particle LET is 10 MeV·cm^2/mg (Si) and electric field strength is 1 MV/cm. Maximum conduction gap is 3 and searching width is 3. Two conduction paths were completely formed as shown in Fig. 5.11 (b). Different colors represent different defect densities of the conduction paths.

The quantum point contact (QPC) theory can be used to estimate the corresponding gate leakage current [55], [68]. The gate leakage current of a radiation-induced SBD can be

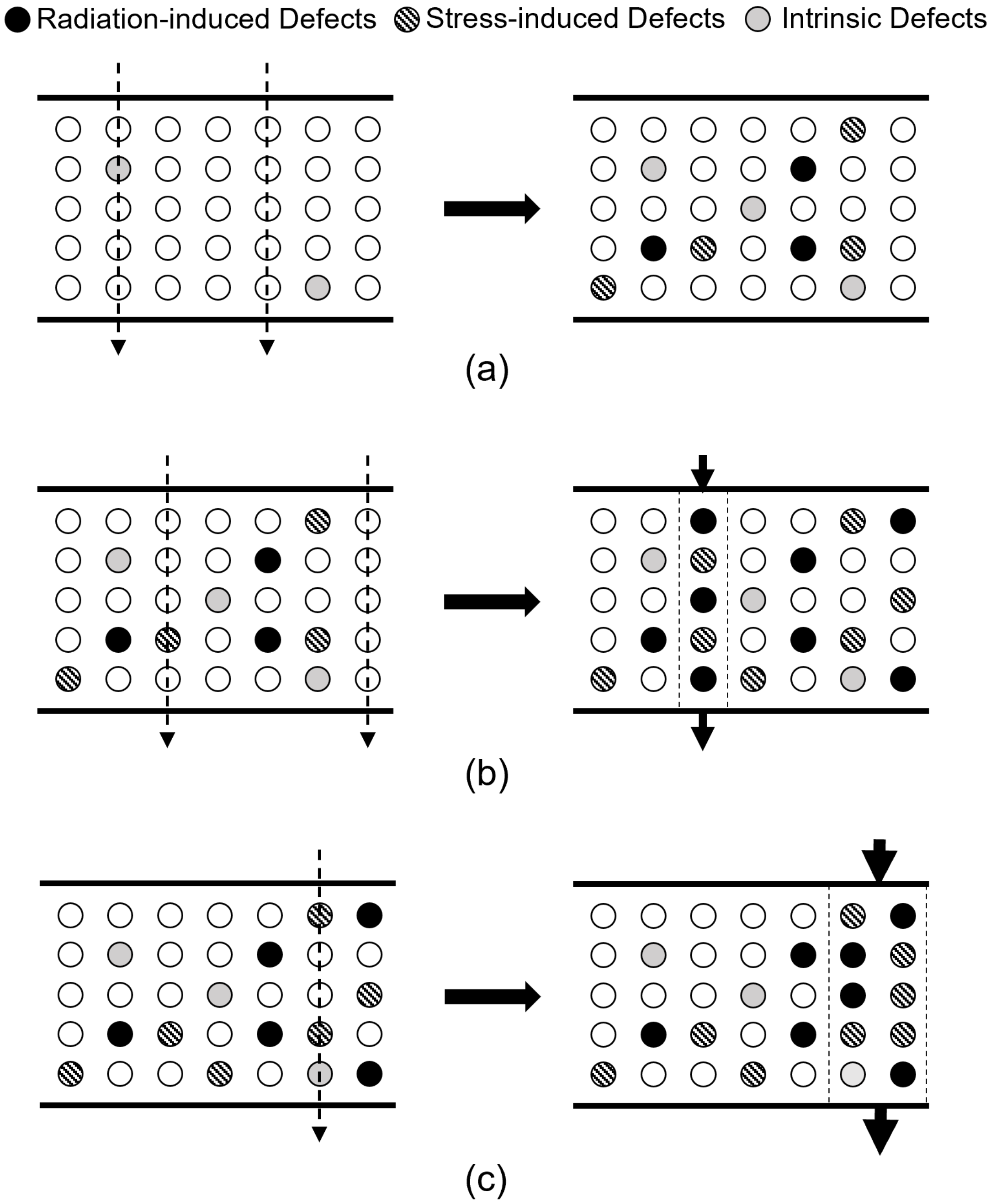

Figure 5.9: A two-dimensional schematic of the percolation theory-based gate dielectric degradation model, where the number of columns N is 7 and the number of cells per column M is 5. Dashed arrows represent radiation particle injection tracks. (a) shows gradually weakend dielectric due to radiation. (b) demonstrates radiation-induced SBD (single event effect), and (c) is an example of radiation-induced HBD with precursor damage dependence. Conduction paths are marked with black arrows.

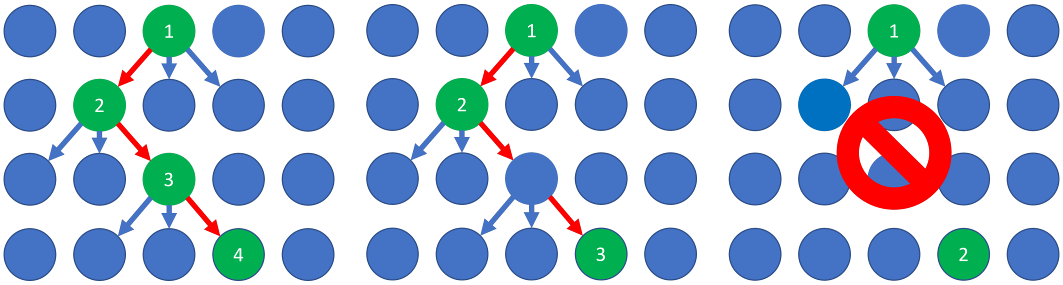

Figure 5.10: An illustration of the seam finding algorithm. Maximum conduction gap is 1 and searching width is 3. Red arrows mark the charge conduction path. No conduction path is formed in the third situation.

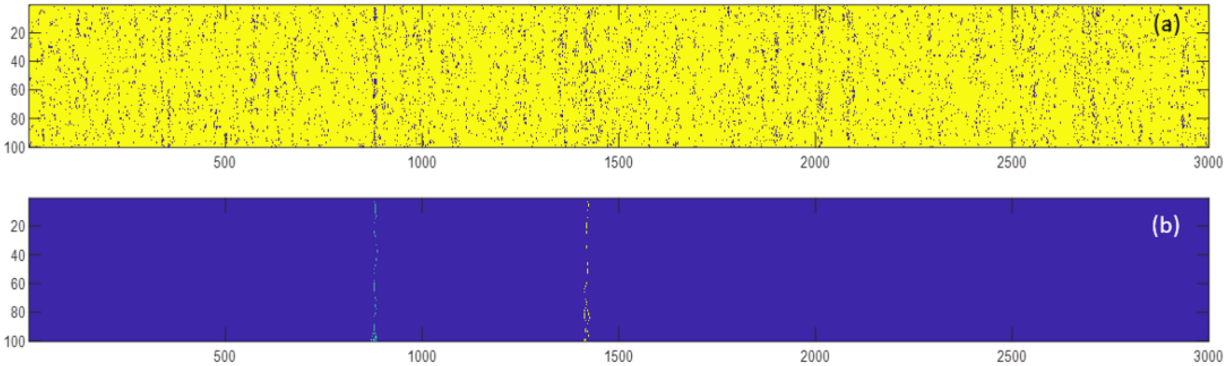

Figure 5.11: An example of Monte Carlo simulation results of the percolation theory-based gate dielectric degradation model. A 3000×100 matrix was irradiated with 3000 particles. Maximum conduction gap is 3 and searching width is 3. (a) shows the final simulation result. Small blue dots are defects generated by radiation and electrical stress. (b) shows the conduction paths found by the seam finding algorithm. Different colors represent different defect densities. In this case, the conduction path on the right has a lower defect density than the one on the left.

calculated by the following equation [55].

$$I = \frac{2e}{h\alpha} e^{-\alpha\phi} [(e^{\alpha\beta e(V-V_0)}) - e^{-\alpha(1-\beta)e(V-V_0)}] \tag{5.7}$$

where α is the transmission coefficient of the point defect, ϕ is the energy level of the trap states relative to the Fermi energy, e is the electron charge, h is Planck's constant, V is the voltage across the dielectric, V_0 is the voltage drop across the constriction and β is the fraction of V_0 which drops on the source side of the constriction [55]. Typically, $V \gg V_0$ and β=0.5. Then, we can simplify this equation as follows [55]:

$$I = \frac{4e}{h\alpha} e^{-\alpha\phi} sinh(\frac{\alpha e V}{2}) \tag{5.8}$$

For a radiation-induced HBD, the leakage current follows a theoretical expression of the form [55]:

$$I = \frac{2e^2}{h}(V - V_0) \tag{5.9}$$

which can be simplified as:

$$I = \frac{2e^2}{h} V \tag{5.10}$$

The total leakage current conducted through the dielectric is given by:

$$I_{Leakage} = \sum_{i=1}^{N_{SBD}} \frac{4e}{h\alpha} e^{-\alpha\phi} sinh(\frac{\alpha e V}{2}) + \sum_{i=1}^{N_{HBD}} \frac{2e^2}{h} V \tag{5.11}$$

where N_{SBD} is the total number of radiation-induced SBD conduction paths and N_{HBD} is the total number of radiation-induced HBD conduction paths. Based on 5.11, the corresponding leakage current of the Monte Carlo simulation result can be estimated. An example of the simulated leakage current vs. effective fluence is shown in Fig. 5.12. The simulated dielectric leakage current reproduced the multistage degradation process observed in heavy-ion irradiation experiments, as shown in Fig. 5.13. However, the simulated progression of breakdown points and the magnitude of current steps are mismatched with experimental data, as most of the parameters used in the simulations are picked based on simple assumptions. In other

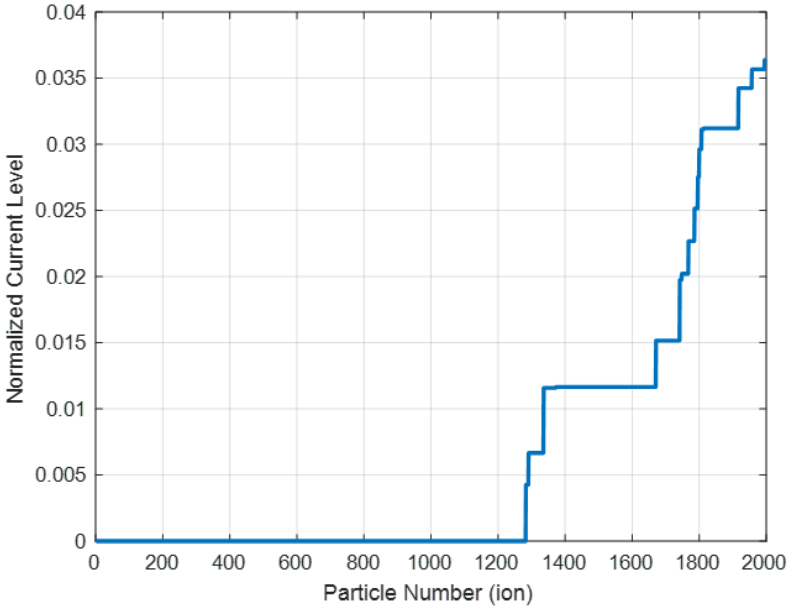

Figure 5.12: An example of simulated dielectric leakage current vs. effective fluence. A 3000×300 matrix was defined in the Monte Carlo simulation. Maximum conduction gap is 1 and searching width is 3. The leakage current of each conduction path is dynamically calculated by the QPC model. The simulation results reproduced the multistage degradation process observed in irradiation experiments.

words, the presented simulation results are a qualitative match of the experimental data and more work is necessary to improve the physical match with reality.

In this chapter, we have demonstrated that both multiple impact effects and single event effects are the key factors dominating radiation-induced dielectric breakdown events based on experimental data and simulation results. For low-energy particles, the gate dielectric is gradually weakened by multiple impact effects, which reduces the breakdown field E_{BD} and eventually leads to breakdown events. Particles with high LETs will induce strong electric field transients inside the device, which can generate a sufficient amount of defects to trigger a breakdown event. Further, we proposed a defect-assisted dielectric breakdown model, which is based on the percolation theory. In this model, radiation-induced electric field transients and electrical stress generate defects inside the dielectric. As the spacing between defects becomes smaller, current conduction paths will form and trigger breakdown events. The

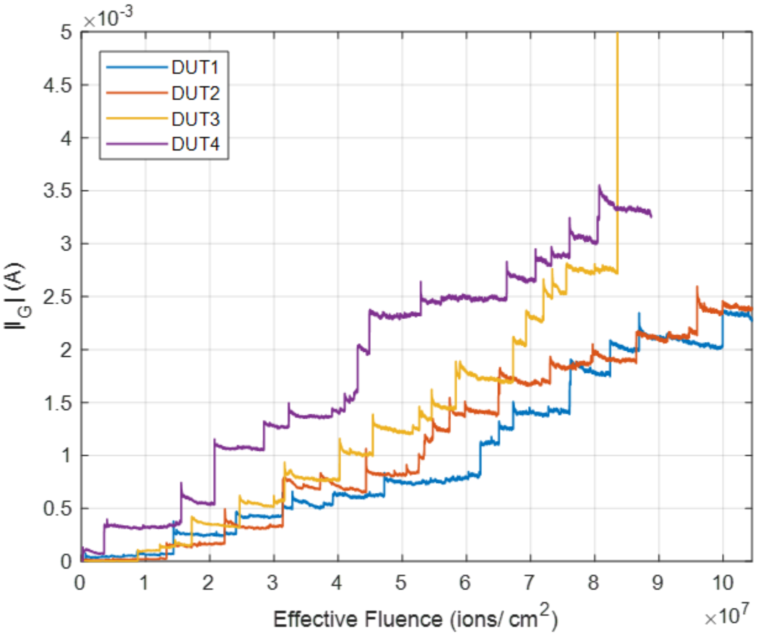

Figure 5.13: Examples of multistage degradation process observed in heavy-ion irradiation experiments. DUT3 experienced a radiation-induced HBD at the end of the experiment. V_{DS}=75 V (DUT1 to DUT3), V_{DS}=100 V (DUT4), V_{GS}=-14 V, LET=12 MeV·cm^2/mg (Si), and flux=1×10^5 ion/cm^2·s.

QPC model has been used to estimate the leakage current of each conduction path. Monte Carlo simulation results reproduced the multistage breakdown process observed in heavy-ion irradiation experiments. Future work is necessary to improve the physical match to produce a real quantitative model.

Chapter 6

Conclusion

In this dissertation, the radiation effects of a commercial D-mode GaN HEMT technology for power applications, including X-ray-induced total ionizing dose effects, Heavy-ion-induced single event effects, and neutron-induced single event effects have been studied. Based on the experimental data, D-mode GaN HEMT is relatively insensitive to X-ray and the main TID effect is threshold voltage V_{th} shift due to charge trapping inside the dielectric. Two different trapping mechanisms including hole trapping and electron trapping were observed. No gate dielectric degradation was observed in X-ray irradiation experiments.

Heavy-ion effects on D-mode GaN HEMTs have been studied as a function of bias voltages (V_{GS} and V_{DS}), incident ion LET, and radiation flux. The irradiated devices showed heavy-ion-induced gate dielectric degradation, which is consistent with SEGR. A multistage degradation process has been observed in most experiments, which consists of radiation-induced SBD to HBD. This indicates both radiation-induced SBD and HBD share a common statistical and physical origin and are associated with defect-related conduction paths across the dielectric. The experimental data under different conditions imply that bias condition, incident ion LET, and radiation flux are the key factors that determine the defect generation rate. The zero-drain-bias experiment and critical injection level experiments indicate that electron-hole pair generation is closely related to defect and trapped charge generation inside the dielectric and the interface. Generally, enhanced charge collection efficiency observed at higher LET values, higher V_{DS}, lower channel conduction current, and higher flux results in larger gate leakage current. Post-radiation electrical characterization measurements indicate charges trapped inside the dielectric and the dielectric/AlGaN interface.

A tuned 2D TCAD model of the GaN HEMTs was developed and used to look at the size and duration of electric field transients induced by secondary ions as a function of injection location in the device, ion LET, applied V_{DS} and applied V_{GS}. Particle injection location was found to have a large impact on the magnitude and duration of the resultant electric-field transient, with events injected near the drain edge having the most impact and injections near the source having almost no impact. Not surprisingly, particle LET was found to have a large impact on the magnitude and duration of the transient events. V_{GS} greatly affects the electric field transients by changing the 2DEG channel conductivity. The impact of different V_{DS} had the least influence on secondary particle-induced transients in GaN HEMTs.

Neutron irradiation experiments have been carried out to investigate the neutron tolerance of the D-mode AlGaN/GaN HEMT. A custom, highly-parallel characterization system was designed, built, and validated which enabled the testing of 360 power transistors, at seven different drain stresses in a single test campaign. Data from this experiment enabled extrapolation of AlGaN/GaN HEMT reliability under terrestrial neutrons as a function of drain voltage stress. The devices showed neutron-induced gate dielectric degradation, which caused increased leakage in many failed samples, and catastrophic breakdown in a few of the failed devices. Post-radiation characterization results indicate the failures are consistent with SEGR/SEB. Corresponding field failure rates have been estimated, indicating a sub 2 FIT extrapolated field failure rate for this GaN HEMT technology at 400 V.

Further, Geant4 nuclear reaction modeling and SRIM stopping power tools were used to define the terrestrial neutron-induced secondary LET spectrum in GaN HEMTs. We found that the LET range of neutron-generated secondary ions in GaN was monotonically decreasing (lower LET events are more common than higher LET events) from an LET of 12 to 0 MeV$\cdot$cm^2/mg (GaN), corresponding to a LET range of 22 to 0 MeV$\cdot$cm^2/mg (Si) equivalent. These simulation results were used to bind the range of particle LETs that were injected to generate transient device simulations. TCAD simulation results and accelerated neutron experimental results correlated in a number of ways and this study demonstrated, definitively, that even low LET events could generate electric fields capable of producing SEGR in GaN HEMTs by producing radiation-induced SBD and HBD in the gate dielectric.

Both heavy-ion and neutron irradiation experimental results indicate that both multiple impact effects and single event effects are responsible for radiation-induced dielectric breakdown events. Moreover, the percolation theory-based gate dielectric degradation model was proposed to explain radiation-induced SBD and HBD in GaN HEMTs. In this model, radiation-induced electric field transients and electrical stress generate defects inside the dielectric. When the spacing between defects becomes small, current conduction paths will form and trigger breakdown events. Monte Carlo simulations were carried out, which reproduced the multistage degradation process. Overall, our experimental data and simulation results provide a better understanding of the factors that affect depletion-mode AlGaN/GaN HEMT technologies reliability in different radiation environments.

APPENDIX A

The decapping procedure Chemicals required: Acid: 95% Sulfuric Acid, Potassium hydroxide

Instruments required: Hot plate, Fuming hood, Burette

1. Heat 95% sulfuric acid to 200°C with hot plate.
2. Put the sample on the hot plate.
3. Drop the heated sulfuric acid on the sample surface with a 6 ml/min flow rate.
4. Repeat step 3 till the die is fully exposed.
5. Clean the die with potassium hydroxide solution.
6. Clean the sample with deionized water.

APPENDIX B

How to setup Python based Geant4 on Linux machines Geant4Py is a Geant4-Python bridge, that provides a bridge for Geant4 classes. A docker container for the Python-based Geant4 application is available at https://github.com/rotiyan/Geant4-py, which includes basic Geant4 functions. To load the docker in the Linux machine, Singularity is required to load the docker file, which is a free and open-source computer program performing operating-system-level virtualization, also known as containerization. Here is an example code for downloading the docker file:

1. `module load singularity`
2. `singularity pull docker://rotiyan/geant4-10.7:10.7.1`

Once successfully downloaded the docker file, we can load it via Singularity:

1. `module load singularity`
2. `module load spack`
3. `module load python`
4. `singularity shell -B /hpc:/hpc geant4-10.7_10.7.1.sif`

After loading the docker file, three root files have to be sourced: (source these files via your own file path)

1. `source /share/Geant4-10.4.2/geant4make/geant4make.sh`
2. `source /app/root/root-6.18.04-build/bin/thisroot.sh`
3. `source /app/geant4/geant4-10.7.1-install/bin/geant4.sh`

Now you can run the G4py demo:

```
python demo.py
```

APPENDIX C

Python-based Geant4 graphical user interface (GUI) Based on the Geant4py, we further developed a Python-based graphical user interface for carrying out basic Geant4 simulations, which is available for downloading at https://github.com/rotiyan/Geant4-py. This Python-based GUI has integrated multiple functions including target define, particle source define, real-time simulation results visualization, and output data saving. Fig. 6.1 shows a block diagram of the Python-based Geant4 GUI. This Geant4 GUI can also run in batch mode without visualizations. Note that, the Python-based Geant4 GUI is compatible with external random seeds for simulations. Once you successfully load the G4py docker (more information in 6), use the following commands to run the GUI (non-batch mode and batch mode):

1. python Geant4-GUI-V2.py –Btach Off
2. python Geant4-GUI-V2.py –Btach Batch-Setupfile.txt –Seed RandomSeedInput

Fig. 6.2 is the starting page of the Geant4 GUI. The 'Help' option contains a basic guide to Geant4. The drop-down menu of the 'File' option includes:

1. Target geometry editor, as shown in Fig. 6.3. First, you have to define the world environment of the target, which can either be vacuum or air. Note that, this is a box target editor, which means you can only define box structures. Various preloaded materials are available, such as silicon, gallium nitride, boron, etc. During the structure definition, a real-time visualization of the target is available.
2. Mono energy particle source editor, as shown in Fig. 6.3. The first step is naming your particle source. Various preloaded particles are available, which cover most of the common radiation particles. As a mono-energy planner particle source editor, all

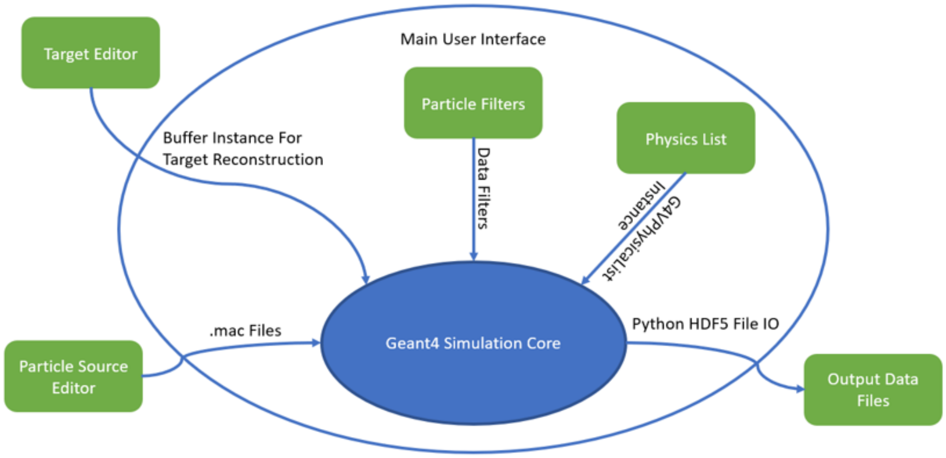

Figure 6.1: A block diagram of the Python-based Geant4 GUI. Software developed by Han Gao.

emitted particles have the same energy and the same injection direction (perpendicular to the particle source surface). You can load your own particle source file in the main program.

3. Batch mode setup file editor. Batch mode setup files contain the information including target file name, particle source name, output file name, physics list, number of events, and data saving conditions.

4. Geant4 particle simulator, as shown in Fig. 6.5. Firstly, you have to define how many particles you want to run for your simulations. How to pick a physic list is highly dependent on your use case. Most commonly used physics lists are available in the option. Enter the file names of the particle source and target previously defined in the mono-energy particle source editor and target geometry editor. You can choose the physics processes (elastic and inelastic) to be activated or not. Real-time visualizations of the simulations are available. Note that, the whole program is based on Python2, which is not compatible with Python3 environments.

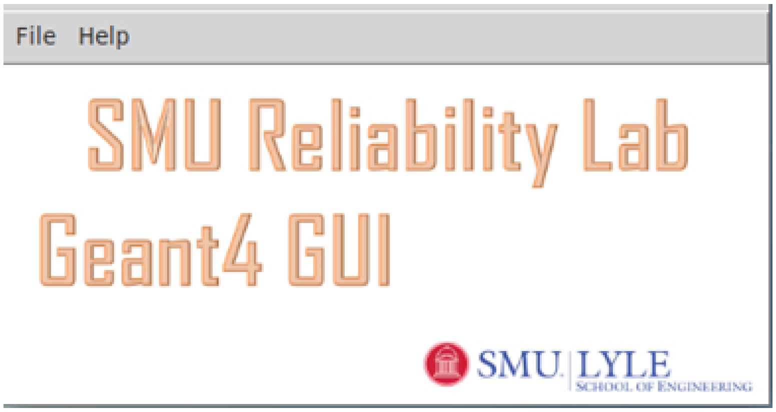

Figure 6.2: Starting page of the Geant4 GUI. A basic Geant4 guide is available in 'Help'. Click 'File' to choose the subprograms including target define, particle source define, run simulation, and batch mode setup file define.

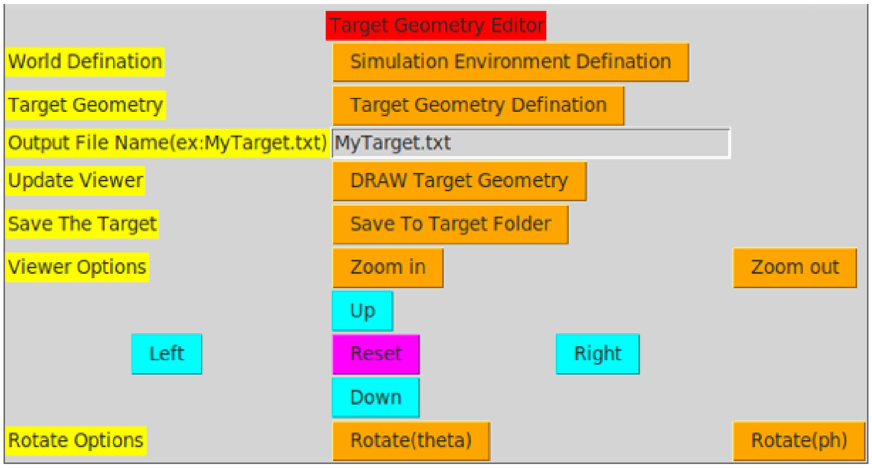

Output File Name(ex:MyTarget.txt) MyTarget.txt

Figure 6.3: Target geometry editor of the Geant4 GUI. A box target with multiple layers can be defined via this editor. Various preloaded materials are available, such as silicon, gallium nitride, boron, etc.

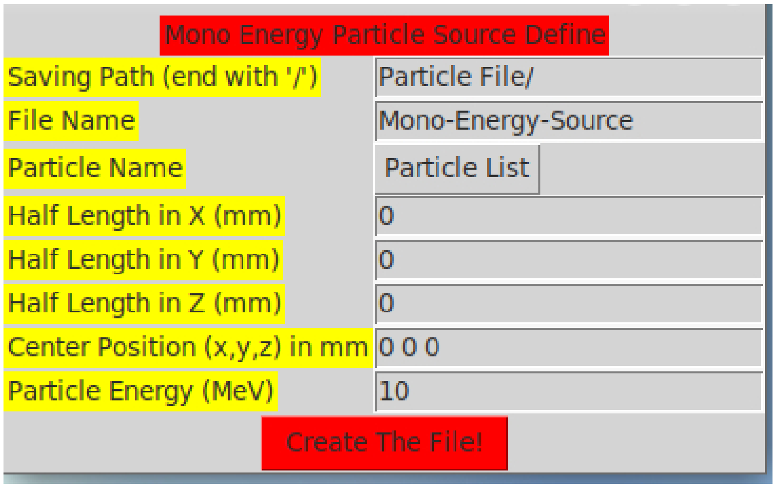

Mono Energy Particle Source Define

Saving Path (end with '/')	Particle File/
File Name	Mono-Energy-Source
Particle Name	Particle List
Half Length in X (mm)	0
Half Length in Y (mm)	0
Half Length in Z (mm)	0
Center Position (x,y,z) in mm	0 0 0
Particle Energy (MeV)	10

Figure 6.4: Mono energy particle source editor of the Geant4 GUI. Various preloaded particles are available, which cover most of the common radiation particles. This editor can only define mono-energy planner particle source.

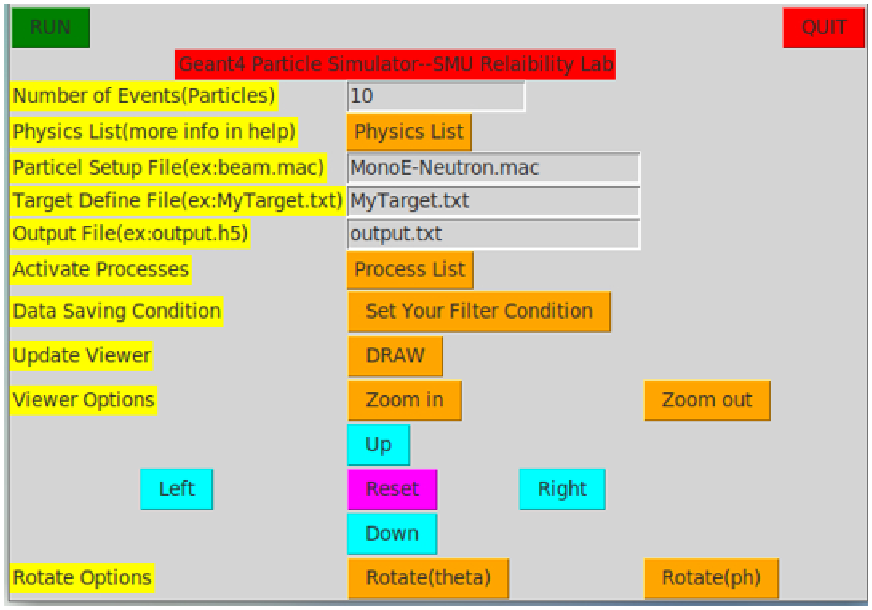

Geant4 Particle Simulator--SMU Relaibility Lab

Number of Events(Particles)	10
Physics List(more info in help)	Physics List
Particel Setup File(ex:beam.mac)	MonoE-Neutron.mac
Target Define File(ex:MyTarget.txt)	MyTarget.txt
Output File(ex:output.h5)	output.txt
Activate Processes	Process List
Data Saving Condition	Set Your Filter Condition
Update Viewer	DRAW
Viewer Options	Zoom in, Zoom out
Rotate Options	Rotate(theta), Rotate(ph)

Figure 6.5: Particle simulator of the Geant4 GUI. The main program carries out the simulations. The output file is in '.h5' format. Real-time visualizations of the simulations are available.

APPENDIX D

Two-dimensional transient simulations in Silvaco TCAD Altlas was used to create a simplified D-mode GaN HEMT structure, which has the same dimensions as the actual device. The polarization charge inside the 2DEG channel is calculated using the built-in models, as specified by the polarization parameter on the model statement. The threshold voltage of the simulated D-mode GaN HEMT is tuned to be -10 V. However, the conductivity of the 2DEG channel is different between the simulated device and the actual device.

The key syntax in single event transient simulation is the 'singleeventupset' statement, which is used to specify entry and exit points, radius, and density of the electron-hole pair distribution generated by the particle track. The density of the electron-hole pair N_{nh} generated by the injected particle can be calculated by the following equation:

$$N_{nh} = \frac{a \cdot LET_{Si} \cdot D_{Si} \cdot q}{E_{GaN}} \tag{6.1}$$

where a is the scaling factor for total ionizing energy deposited by incident particles in GaN, which equals 2.1 in this case based on the SRIM simulation results. LET_{Si} is the particle LET value in MeV·cm^2/mg (Si). $a \cdot LET_{Si} \cdot D_{Si}$ calculates the total energy of an incident particle deposited inside the GaN in MeV. D_{Si} is the silicon density and q is the elementary charge. E_{GaN} represents the energy required to generate an electron-hole pair in GaN. Thus we have:

$$N_{nh} = 0.0088 \cdot LET_{Si} \tag{6.2}$$

where the unit of N_{nh} is pC/μm

The model statement is used to select a set of physical models for this simulation. In this case, these models are concentration-dependent SRH recombination, field-dependent mobility model, and Auger recombination. The 'seu.integrate' parameter in the method statement ensures correct total charge integration in the SEU charge track.

APPENDIX E

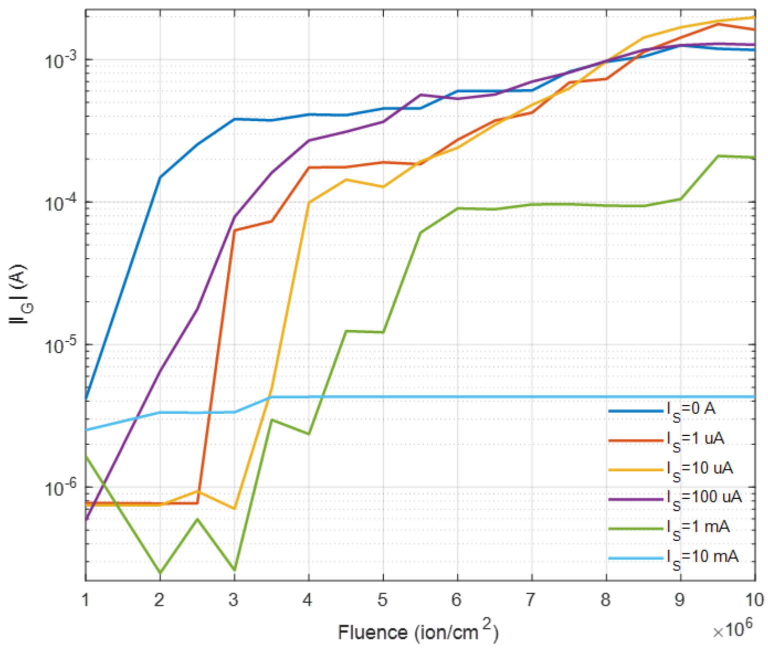

Figure 6.6: Effective fluence vs. gate current under off-state (V_{GS}=-14 V, V_{DS}=150 V) with different current injection levels. 599-MeV Ar (LET=10 MeV·cm^2/mg (Si)) is used with flux equal to 1×10^5 ion/cm^2·s. Total effective fluence is 1×10^7 ion/cm^2 for each run.

Critical injection level experimental data plot

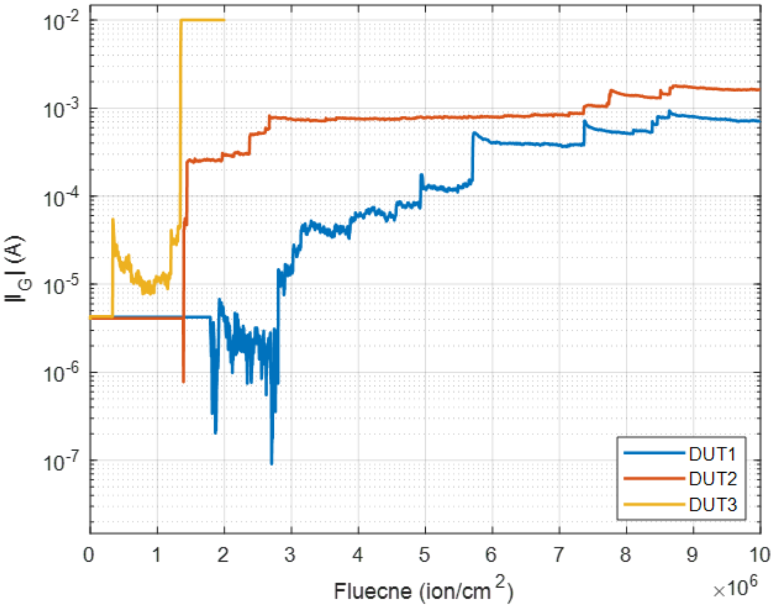

Figure 6.7: Results of critical injection level experiments with 0 A injection level. 599-MeV Ar (LET=10 MeV·cm^2/mg (Si)) is used with flux equal to 1×10^5 ion/cm^2·s. Total effective fluence is 1×10^7 ion/cm^2 for each run. V_G=-14 V and V_{DS}=150 V.

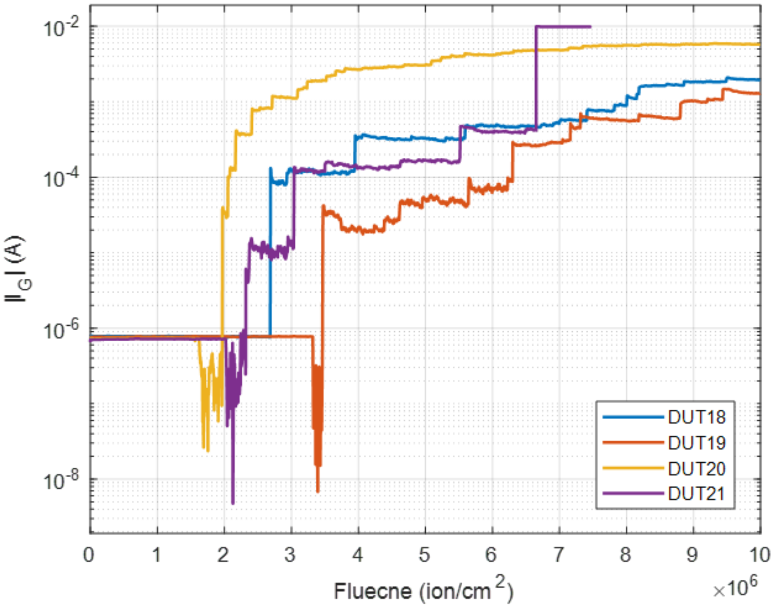

Figure 6.8: Results of critical injection level experiments with 1 μA injection level. 599-MeV Ar (LET=10 MeV·cm^2/mg (Si)) is used with flux equal to 1×10^5 ion/cm^2·s. Total effective fluence is 1×10^7 ion/cm^2 for each run. V_G=-14 V and V_{DS}=150 V.

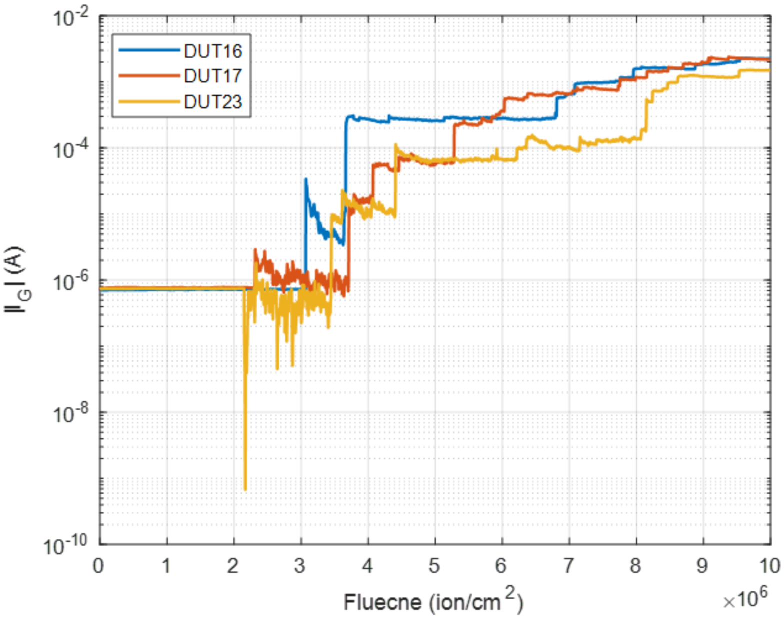

Figure 6.9: Results of critical injection level experiments with 10 μA injection level. 599-MeV Ar (LET=10 MeV·cm^2/mg (Si)) is used with flux equal to 1×10^5 ion/cm^2·s. Total effective fluence is 1×10^7 ion/cm^2 for each run. V_G=-14 V and V_{DS}=150 V.

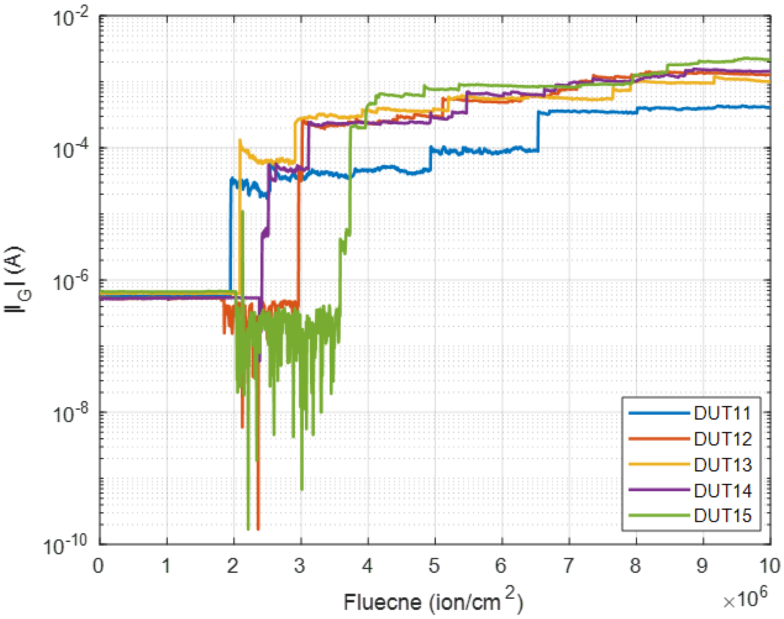

Figure 6.10: Results of critical injection level experiments with 100 μA injection level. 599-MeV Ar (LET=10 MeV·cm^2/mg (Si)) is used with flux equal to 1×10^5 ion/cm^2·s. Total effective fluence is 1×10^7 ion/cm^2 for each run. V_G=-14 V and V_{DS}=150 V.

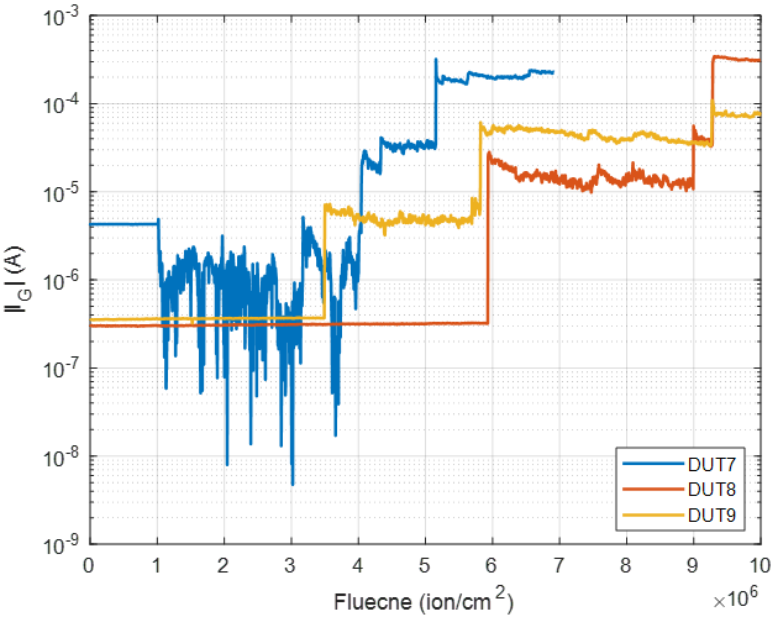

Figure 6.11: Results of critical injection level experiments with 1 mA injection level. 599-MeV Ar (LET=10 MeV·cm^2/mg (Si)) is used with flux equal to 1×10^5 ion/cm^2·s. Total effective fluence is 1×10^7 ion/cm^2 for each run. V_G=-14 V and V_{DS}=150 V.

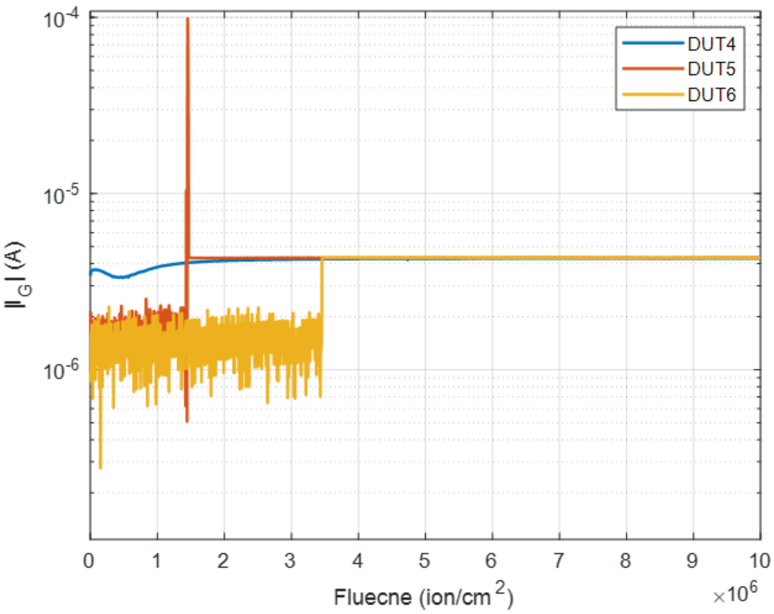

Figure 6.12: Results of critical injection level experiments with 10 mA injection level. 599-MeV Ar (LET=10 MeV·cm^2/mg (Si)) is used with flux equal to 1×10^5 ion/cm^2·s. Total effective fluence is 1×10^7 ion/cm^2 for each run. V_G=-14 V and V_{DS}=150 V.

BIBLIOGRAPHY

[1] B. J. Baliga, *Fundamentals of power semiconductor devices.* Springer Science & Business Media, 2010. 1, 2, 3

[2] J. Millan, P. Godignon, X. Perpiñà, A. Pérez-Tomás, and J. Rebollo, "A survey of wide bandgap power semiconductor devices," *IEEE transactions on Power Electronics*, vol. 29, no. 5, pp. 2155–2163, 2013. 1, 2

[3] B. J. Baliga, "Trends in power semiconductor devices," *IEEE Transactions on electron Devices*, vol. 43, no. 10, pp. 1717–1731, 1996. 1

[4] U. K. Mishra, P. Parikh, and Y.-F. Wu, "Algan/gan hemts-an overview of device operation and applications," *Proceedings of the IEEE*, vol. 90, no. 6, pp. 1022–1031, 2002. 2, 6

[5] A. Lidow, M. De Rooij, J. Strydom, D. Reusch, and J. Glaser, *GaN transistors for efficient power conversion.* John Wiley & Sons, 2019. 2, 3, 4, 5, 6, 8

[6] J. Scarpulla, "Guidelines for space qualification of gan hemts and mmics," in *2021 IEEE International Reliability Physics Symposium (IRPS).* IEEE, 2021, pp. 1–11. 5

[7] X. Hu, G. Simin, J. Yang, M. A. Khan, R. Gaska, and M. Shur, "Enhancement mode algan/gan hfet with selectively grown pn junction gate," *Electronics Letters*, vol. 36, no. 8, pp. 753–754, 2000. 8

[8] W. Schimmerling, "The space radiation environment: an introduction," *The Health Risks of Extraterrestrial Environments*, 2011. 10

[9] J. F. Ziegler, "Terrestrial cosmic rays," *IBM journal of research and development*, vol. 40, no. 1, pp. 19–39, 1996. 10, 12, 14, 87

[10] E. Stassinopoulos and J. P. Raymond, "The space radiation environment for electronics," *Proceedings of the IEEE*, vol. 76, no. 11, pp. 1423–1442, 1988. 10

[11] S. Wender and L. Dominik, "Los alamos high-energy neutron testing handbook," *SAE Technical Paper Series*, 2020. 10, 93, 96

[12] J. L. Barth, C. Dyer, and E. Stassinopoulos, "Space, atmospheric, and terrestrial radiation environments," *IEEE Transactions on nuclear science*, vol. 50, no. 3, pp. 466–482, 2003. 10, 12

[13] P. M. Thelen, "Introduction to the space radiation environment." Sandia National Lab.(SNL-NM), Albuquerque, NM (United States), Tech. Rep., 2018. 10

[14] H. Zell, "Radiation belts with satellites," 2017, last updated: Aug 7, 2017, credit: NASA. [Online]. Available: https://www.nasa.gov/mission_pages/sunearth/news/gallery/20130228-radiationbelts.html 10, 11

[15] J. JESD89A, "Measurement and reporting of alpha particle and terrestrial cosmic ray-induced soft errors in semiconductor devices," 2012. 12, 15

[16] E. Normand, J. L. Wert, D. L. Oberg, P. Majewski, P. Voss, and S. Wender, "Neutron-induced single event burnout in high voltage electronics," *IEEE Transactions on Nuclear Science*, vol. 44, no. 6, pp. 2358–2366, 1997. 12, 87

[17] T. Shoji, S. Nishida, T. Ohnishi, T. Fujikawa, N. Nose, M. Ishiko, and K. Hamada, "Neutron induced single-event burnout of igbt," in *The 2010 International Power Electronics Conference-ECCE ASIA-*. IEEE, 2010, pp. 142–148. 12, 87

[18] H. Asai, I. Nashiyama, K. Sugimoto, K. Shiba, Y. Sakaide, Y. Ishimaru, Y. Okazaki, K. Noguchi, and T. Morimura, "Tolerance against terrestrial neutron-induced single-event burnout in sic mosfets," *IEEE Transactions on Nuclear Science*, vol. 61, no. 6, pp. 3109–3114, 2014. 12, 87

[19] "Unknown caption," 1999, images reproduced from original 24x36mm slides - Digital Memory project. [Online]. Available: https://cds.cern.ch/record/2459167 14

[20] A. Javanainen and S. Moss, "See testing with broad and focused particle beams," *IEEE NSREC Short Course Notebook*, 2019. 16, 17, 19

[21] J. R. Schwank, M. R. Shaneyfelt, D. M. Fleetwood, J. A. Felix, P. E. Dodd, P. Paillet, and V. Ferlet-Cavrois, "Radiation effects in mos oxides," *IEEE Transactions on Nuclear Science*, vol. 55, no. 4, pp. 1833–1853, 2008. 18, 19

[22] T. R. Oldham, "Basic mechanisms of tid and ddd response in mos and bipolar microelectronics," *NSREC Short Course*, 2011. 18

[23] D. Kobayashi and S. Moss, "Basics of single event effect mechanisms and predictions," *IEEE NSREC Short Course Notebook*, 2019. 19, 21, 22, 23, 24, 25, 113

[24] S. Liu, M. Boden, D. A. Girdhar, and J. L. Titus, "Single-event burnout and avalanche characteristics of power dmosfets," *IEEE Transactions on Nuclear Science*, vol. 53, no. 6, pp. 3379–3385, 2006. 23

[25] J. Srour, C. J. Marshall, and P. W. Marshall, "Review of displacement damage effects in silicon devices," *IEEE transactions on nuclear science*, vol. 50, no. 3, pp. 653–670, 2003. 24, 25, 26, 27

[26] T. F. Wrobel, "On heavy ion induced hard-errors in dielectric structures," *IEEE Transactions on Nuclear Science*, vol. 34, no. 6, pp. 1262–1268, 1987. 28

[27] L. Massengill, B. Choi, D. Fleetwood, R. Schrimpf, K. Galloway, M. Shaneyfelt, T. Meisenheimer, P. Dodd, J. Schwank, Y. Lee *et al.*, “Heavy-ion-induced breakdown in ultra-thin gate oxides and high-k dielectrics,” *IEEE Transactions on Nuclear Science*, vol. 48, no. 6, pp. 1904–1912, 2001. 28

[28] J. Suñé, G. Mura, and E. Miranda, “Are soft breakdown and hard breakdown of ultrathin gate oxides actually different failure mechanisms?” *IEEE Electron Device Letters*, vol. 21, no. 4, pp. 167–169, 2000. 28, 85, 86, 102

[29] M. Beck, Y. Puzyrev, N. Sergueev, K. Varga, R. Schrimpf, D. Fleetwood, and S. Pantelides, “The role of atomic displacements in ion-induced dielectric breakdown,” *IEEE Transactions on Nuclear Science*, vol. 56, no. 6, pp. 3210–3217, 2009. 28, 85

[30] F. Sexton, D. Fleetwood, M. Shaneyfelt, P. Dodd, G. Hash, L. Schanwald, R. Loemker, K. Krisch, M. Green, B. Weir *et al.*, “Precursor ion damage and angular dependence of single event gate rupture in thin oxides,” *IEEE Transactions on Nuclear Science*, vol. 45, no. 6, pp. 2509–2518, 1998. 28

[31] S. Lombardo, J. H. Stathis, B. P. Linder, K. L. Pey, F. Palumbo, and C. H. Tung, “Dielectric breakdown mechanisms in gate oxides,” *Journal of applied physics*, vol. 98, no. 12, p. 12, 2005. 29, 33

[32] E. Y. Wu, “Facts and myths of dielectric breakdown processes—part i: Statistics, experimental, and physical acceleration models,” *IEEE Transactions on Electron Devices*, vol. 66, no. 11, pp. 4523–4534, 2019. 29, 30, 31, 32, 86, 119

[33] G. Barbottin and A. Vapaille, *Instabilities in silicon devices: silicon passivation and related instabilities*. North-Holland, 1986. 32

[34] K.-H. Allers, “Prediction of dielectric reliability from i–v characteristics: Poole–frenkel conduction mechanism leading to$\sqrt{}$ e model for silicon nitride mim capacitor,” *Microelectronics Reliability*, vol. 44, no. 3, pp. 411–423, 2004. 32

[35] N. Suzumura, S. Yamamoto, D. Kodama, K. Makabe, J. Komori, E. Murakami, S. Maegawa, and K. Kubota, “A new tddb degradation model based on cu ion drift in cu interconnect dielectrics,” in *2006 IEEE International Reliability Physics Symposium Proceedings*. IEEE, 2006, pp. 484–489. 32

[36] D. DiMaria, “Explanation for the polarity dependence of breakdown in ultrathin silicon dioxide films,” *Applied Physics Letters*, vol. 68, no. 21, pp. 3004–3006, 1996. 32, 54

[37] R. Degraeve, G. Groeseneken, I. De Wolf, and H. Maes, “Oxide and interface degradation and breakdown under medium and high field injection conditions: A correlation study,” *Microelectronic Engineering*, vol. 28, no. 1-4, pp. 313–316, 1995. 32

[38] S. Palit and M. A. Alam, “Theory of charging and charge transport in “intermediate” thickness dielectrics and its implications for characterization and reliability,” *Journal of Applied Physics*, vol. 111, no. 5, p. 054112, 2012. 32

[39] E. Y. Wu, A. Vayshenker, E. Nowak, J. Sune, R.-P. Vollertsen, W. Lai, and D. Harmon, “Experimental evidence of t/sub bd/power-law for voltage dependence of oxide breakdown in ultrathin gate oxides,” *IEEE Transactions on Electron Devices*, vol. 49, no. 12, pp. 2244–2253, 2002. 32

[40] B. L. Gregory and C. W. Gwyn, “Radiation effects on semiconductor devices,” *Proceedings of the IEEE*, vol. 62, no. 9, pp. 1264–1273, 1974. 33

[41] J. H. Hubbell and S. M. Seltzer, “Tables of x-ray mass attenuation coefficients and mass energy-absorption coefficients 1 kev to 20 mev for elements z= 1 to 92 and 48 additional substances of dosimetric interest,” National Inst. of Standards and Technology-PL, Gaithersburg, MD (United . . . , Tech. Rep., 1995. 38

[42] J. F. Ziegler, M. D. Ziegler, and J. P. Biersack, “Srim–the stopping and range of ions in matter (2010),” *Nuclear Instruments and Methods in Physics Research Section B: Beam Interactions with Materials and Atoms*, vol. 268, no. 11-12, pp. 1818–1823, 2010. 46

[43] D. Peyre, C. Binois, R. Mangeret, G. Salvaterra, M. Beaumel, F. Pontoni, T. Bouchet, L. Pater, F. Bezerra, R. Ecoffet *et al.*, “Segr study on power mosfets: Multiple impacts assumption,” in *2007 9th European Conference on Radiation and Its Effects on Components and Systems.* IEEE, 2007, pp. 1–8. 54, 113

[44] D. M. Fleetwood, E. X. Zhang, R. D. Schrimpf, and S. T. Pantelides, “Radiation effects in algan/gan hemts,” *IEEE Transactions on Nuclear Science*, vol. 69, no. 5, pp. 1105–1119, 2022. 60, 85, 86

[45] E. H. Nicollian and J. R. Brews, *MOS (metal oxide semiconductor) physics and technology.* John Wiley & Sons, 2002. 64

[46] P. Winokur, J. Schwank, P. McWhorter, P. Dressendorfer, and D. Turpin, “Correlating the radiation response of mos capacitors and transistors,” *IEEE Transactions on Nuclear Science*, vol. 31, no. 6, pp. 1453–1460, 1984. 64

[47] S. C. Witczak, P. S. Winokur, R. C. Lacoe, and D. C. Mayer, “Charge separation technique for metal–oxide–silicon capacitors in the presence of hydrogen deactivated dopants,” *Journal of Applied Physics*, vol. 87, no. 11, pp. 8206–8208, 2000. 64

[48] J. Felix, D. Fleetwood, R. Schrimpf, J. Hong, G. Lucovsky, J. Schwank, and M. Shaneyfelt, “Total-dose radiation response of hafnium-silicate capacitors,” *IEEE Transactions on Nuclear Science*, vol. 49, no. 6, pp. 3191–3196, 2002. 65

[49] M. Rostewitz, K. Hirche, J. Lätti, and E. Jutzi, “Single event effect analysis on dc and rf operated algan/gan hemts,” *IEEE Transactions on Nuclear Science*, vol. 60, no. 4, pp. 2525–2529, 2013. 65

[50] Y. Kamigaki, S.-i. Minami, and H. Kato, “A new portrayal of electron and hole traps in amorphous silicon nitride,” *Journal of applied physics*, vol. 68, no. 5, pp. 2211–2215, 1990. 66

[51] R. Vetury, N. Q. Zhang, S. Keller, and U. K. Mishra, “The impact of surface states on the dc and rf characteristics of algan/gan hfets,” *IEEE Transactions on Electron Devices*, vol. 48, no. 3, pp. 560–566, 2001. 66

[52] A. S. Lee, N. Rajagopalan, M. Le, B. H. Kim, and H. M’Saad, “Development and characterization of a pecvd silicon nitride for damascene applications,” *Journal of The Electrochemical Society*, vol. 151, no. 1, p. F7, 2003. 68

[53] A. Johnston, G. Swift, T. Miyahira, and L. Edmonds, “Breakdown of gate oxides during irradiation with heavy ions,” *IEEE Transactions on Nuclear Science*, vol. 45, no. 6, pp. 2500–2508, 1998. 68, 86, 111, 119

[54] E. Miranda and J. Suñé, “Analytic modeling of leakage current through multiple breakdown paths in sio/sub 2/films,” in *2001 IEEE International Reliability Physics Symposium Proceedings. 39th Annual (Cat. No. 00CH37167)*. IEEE, 2001, pp. 367–379. 85, 102

[55] J. Suñé, “New physics-based analytic approach to the thin-oxide breakdown statistics,” *IEEE Electron Device Letters*, vol. 22, no. 6, pp. 296–298, 2001. 85, 102, 120, 121, 124

[56] JESD89B, “Measurement and reporting of alpha particle and terrestrial cosmic ray induced soft errors in semiconductor devices,” *JEDEC*, 2021. 87

[57] S. Agostinelli, J. Allison, K. a. Amako, J. Apostolakis, H. Araujo, P. Arce, M. Asai, D. Axen, S. Banerjee, G. Barrand *et al.*, “Geant4—a simulation toolkit,” *Nuclear instruments and methods in physics research section A: Accelerators, Spectrometers, Detectors and Associated Equipment*, vol. 506, no. 3, pp. 250–303, 2003. 87

[58] J. Ziegler, “Stopping and range of ions in solids,” Tech. Rep., 1986. 87

[59] H. Quinn, A. Watkins, L. Dominik, and C. Slayman, “The effect of 1–10-mev neutrons on the jesd89 test standard,” *IEEE Transactions on Nuclear Science*, vol. 66, no. 1, pp. 140–147, 2018. 88

[60] F. Principato, G. Allegra, C. Cappello, O. Crepel, N. Nicosia, S. D′ Arrigo, V. Cantarella, A. Di Mauro, L. Abbene, M. Mirabello *et al.*, “Investigation of the impact of neutron irradiation on sic power mosfets lifetime by reliability tests,” *Sensors*, vol. 21, no. 16, p. 5627, 2021. 97, 98

[61] D. J. Lichtenwalner, A. Akturk, J. McGarrity, J. Richmond, T. Barbieri, B. Hull, D. Grider, S. Allen, and J. W. Palmour, “Reliability of sic power devices against cosmic ray neutron single-event burnout,” in *Materials Science Forum*, vol. 924. Trans Tech Publ, 2018, pp. 559–562. 100

[62] A. Akturk, R. Wilkins, J. McGarrity, and B. Gersey, “Single event effects in si and sic power mosfets due to terrestrial neutrons,” *IEEE Transactions on Nuclear Science*, vol. 64, no. 1, pp. 529–535, 2016. 100

[63] D. J. Lichtenwalner, S. Sabri, E. van Brunt, B. Hull, S.-H. Ryu, P. Steinmann, A. Romero, S. Ganguly, D. A. Gajewski, S. Allen *et al.*, "Accelerated testing of sic power devices," in *2020 IEEE International Integrated Reliability Workshop (IIRW)*. IEEE, 2020, pp. 1–6. 100

[64] C. Martinella, R. G. Alía, R. Stark, A. Coronetti, C. Cazzaniga, M. Kastriotou, Y. Kadi, R. Gaillard, U. Grossner, and A. Javanainen, "Impact of terrestrial neutrons on the reliability of sic vd-mosfet technologies," *IEEE Transactions on Nuclear Science*, vol. 68, no. 5, pp. 634–641, 2021. 100

[65] T. Mizutani, Y. Ohno, M. Akita, S. Kishimoto, and K. Maezawa, "A study on current collapse in algan/gan hemts induced by bias stress," *IEEE transactions on Electron Devices*, vol. 50, no. 10, pp. 2015–2020, 2003. 103

[66] R. T. Narayan and H. Gao, "Docker container for python based geant4 application," 2023. [Online]. Available: https://github.com/rotiyan/Geant4-py 104

[67] J. Han and G. Guo, "Characteristics of energy deposition from 1-1000 mev proton and neutron induced nuclear reactions in silicon," *AIP Advances*, vol. 7, no. 11, p. 115220, 2017. 105

[68] B. Choi, D. Fleetwood, R. Schrimpf, L. W. Massengill, K. Galloway, M. Shaneyfelt, T. Meisenfieimer, P. Dodd, J. Schwank, Y. Lee *et al.*, "Long-term reliability degradation of ultrathin dielectric films due to heavy-ion irradiation," *IEEE Transactions on Nuclear Science*, vol. 49, no. 6, pp. 3045–3050, 2002. 120, 121

[69] S. Avidan and A. Shamir, "Seam carving for content-aware image resizing," in *ACM SIGGRAPH 2007 papers*, 2007, pp. 10–es. 121

[70] J. Piprek, *Nitride semiconductor devices: principles and simulation*. John Wiley & Sons, 2007.

[71] S. Karmalkar and U. K. Mishra, "Enhancement of breakdown voltage in algan/gan high electron mobility transistors using a field plate," *IEEE transactions on electron devices*, vol. 48, no. 8, pp. 1515–1521, 2001.

[72] J. Joh and J. A. Del Alamo, "Critical voltage for electrical degradation of gan high-electron mobility transistors," *IEEE Electron Device Letters*, vol. 29, no. 4, pp. 287–289, 2008.

[73] J. Jep151, "Test procedure for the measurement of terrestrial cosmic ray induced destructive effects in power semiconductor devices," 2015.

[74] R. C. Baumann, "Radiation-induced soft errors in advanced semiconductor technologies," *IEEE Transactions on Device and materials reliability*, vol. 5, no. 3, pp. 305–316, 2005.

[75] M. Gordon, P. Goldhagen, K. Rodbell, T. Zabel, H. Tang, J. Clem, and P. Bailey, "Measurement of the flux and energy spectrum of cosmic-ray induced neutrons on the ground," *IEEE Transactions on Nuclear Science*, vol. 51, no. 6, pp. 3427–3434, 2004.

[76] J. Dirk, M. E. Nelson, J. F. Ziegler, A. Thompson, and T. H. Zabel, "Terrestrial thermal neutrons," *IEEE Transactions on Nuclear Science*, vol. 50, no. 6, pp. 2060–2064, 2003.

[77] P. Adell and L. Scheick, "Radiation effects in power systems: A review," *IEEE Transactions on Nuclear Science*, vol. 60, no. 3, pp. 1929–1952, 2013.

[78] M. Guziewicz, E. Kaminska, A. Piotrowska, K. Golaszewska, J. Domagala, M. Poisson, H. Lahreche, R. Langer, and P. Bove, "Comparative study on stress in algan/gan hemt structures grown on 6h-sic, si and on composite substrates of the 6h-sic/poly-sic and si/poly-sic," in *Journal of Physics: Conference Series*, vol. 100, no. 4. IOP Publishing, 2008, p. 042035.

[79] J. Yaita, K. Fukuda, A. Yamada, T. Iwasaki, S. Nakaharai, and J. Kotani, "Improved channel electron mobility through electric field reduction in gan quantum-well double-heterostructures," *IEEE Electron Device Letters*, vol. 42, no. 11, pp. 1592–1595, 2021.

[80] Y. Cai, C. Zhu, L. Jiu, Y. Gong, X. Yu, J. Bai, V. Esendag, and T. Wang, "Strain analysis of gan hemts on (111) silicon with two transitional alxga1- xn layers," *Materials*, vol. 11, no. 10, p. 1968, 2018.

[81] J. Schwank, M. Shaneyfelt, J. Baggio, P. Dodd, J. Felix, V. Ferlet-Cavrois, P. Paillet, D. Lambert, F. Sexton, G. Hash *et al.*, "Effects of particle energy on proton-induced single-event latchup," *IEEE Transactions on Nuclear Science*, vol. 52, no. 6, pp. 2622–2629, 2005.

[82] J. L. Titus, "An updated perspective of single event gate rupture and single event burnout in power mosfets," *IEEE Transactions on nuclear science*, vol. 60, no. 3, pp. 1912–1928, 2013.

[83] G. C. Messenger, "A summary review of displacement damage from high energy radiation in silicon semiconductors and semiconductor devices," *IEEE Transactions on nuclear Science*, vol. 39, no. 3, pp. 468–473, 1992.

[84] K. F. Schuegraf and C. Hu, "Hole injection oxide breakdown model for very low voltage lifetime extrapolation," in *31st Annual Proceedings Reliability Physics 1993.* IEEE, 1993, pp. 7–12.

[85] D. Bude, B. Weir, and P. Silverman, "Explanation of stress-induced damage in thin oxides," in *International Electron Devices Meeting 1998. Technical Digest (Cat. No. 98CH36217).* IEEE, 1998, pp. 179–182.

[86] J. H. Stathis and D. DiMaria, "Reliability projection for ultra-thin oxides at low voltage," in *International Electron Devices Meeting 1998. Technical Digest (Cat. No. 98CH36217).* IEEE, 1998, pp. 167–170.

[87] J. Stathis, D. DiMaria, H. Massoud, I. Baumvol, M. Hirose, and E. Poindexter, "Defect generation and reliability of ultra-thin sio 2 at low voltage," in *The Physics and Chemistry of SiO2 and the Si-SiO2 Interface- 4.* The Electrochemical Society, 2000, vol. 2000, pp. 33–44.

[88] J. McPherson and H. Mogul, "Underlying physics of the thermochemical e model in describing low-field time-dependent dielectric breakdown in sio 2 thin films," *Journal of Applied Physics*, vol. 84, no. 3, pp. 1513–1523, 1998.

[89] J. C. Lee, C. Ih-Chin, and H. Chenming, "Modeling and characterization of gate oxide reliability," *IEEE Transactions on Electron Devices*, vol. 35, no. 12, pp. 2268–2278, 1988.

[90] M. A. Alam, J. Bude, and A. Ghetti, "Field acceleration for oxide breakdown-can an accurate anode hole injection model resolve the e vs. 1/e controversy?" in *2000 IEEE International Reliability Physics Symposium Proceedings. 38th Annual (Cat. No. 00CH37059).* IEEE, 2000, pp. 21–26.

[91] P. E. Nicollian, "Physics of trap generation and electrical breakdown in ultra-thin sio2 and sion gate dielectric materials," *University of Twente, PhD thesis*, 2007.

[92] D. DiMaria, E. Cartier, and D. Arnold, "Impact ionization, trap creation, degradation, and breakdown in silicon dioxide films on silicon," *Journal of Applied Physics*, vol. 73, no. 7, pp. 3367–3384, 1993.

[93] H. Gao, D. Ahsanullah, R. Baumann, and B. Gnade, "A study of neutron induced single-event damage in algan/gan hemts," in *2022 IEEE Radiation Effects Data Workshop (REDW)(in conjunction with 2022 NSREC).* IEEE, 2022, pp. 1–6.

[94] C. Leroy and P.-G. Rancoita, *Principles of radiation interaction in matter and detection.* World Scientific, 2011.

[95] G. Messenger, "Collection of charge on junction nodes from ion tracks," *IEEE Transactions on nuclear science*, vol. 29, no. 6, pp. 2024–2031, 1982.

[96] J. Wirth and S. Rogers, "The transient response of transistors and diodes to ionizing radiation," *IEEE Transactions on Nuclear Science*, vol. 11, no. 5, pp. 24–38, 1964.

[97] H. J. Queisser and E. E. Haller, "Defects in semiconductors: some fatal, some vital," *Science*, vol. 281, no. 5379, pp. 945–950, 1998.

[98] J. Ziegler, "The stopping of energetic light ions in elemental matter hzetrn: Description of a free-space ion and nucleon transport and shielding computer program," *NASA TP-3495*, 1995.

[99] J. Sune and E. Miranda, “Post soft breakdown conduction in sio/sub 2/gate oxides,” in *International Electron Devices Meeting 2000. Technical Digest. IEDM (Cat. No. 00CH37138).* IEEE, 2000, pp. 533–536.

[100] T. Shoji, S. Nishida, K. Hamada, and H. Tadano, “Analysis of neutron-induced single-event burnout in sic power mosfets,” *Microelectronics Reliability*, vol. 55, no. 9-10, pp. 1517–1521, 2015.

[101] Y. Iwamoto, M. Fukuda, Y. Sakamoto, A. Tamii, K. Hatanaka, K. Takahisa, K. Nagayama, H. Asai, K. Sugimoto, and I. Nashiyama, “Evaluation of the white neutron beam spectrum for single-event effects testing at the rcnp cyclotron facility,” *Nuclear Technology*, vol. 173, no. 2, pp. 210–217, 2011.

[102] L. Lü, J.-C. Zhang, J.-S. Xue, X.-H. Ma, W. Zhang, Z.-W. Bi, Y. Zhang, and Y. Hao, “Neutron irradiation effects on algan/gan high electron mobility transistors,” *Chinese physics B*, vol. 21, no. 3, p. 037104, 2012.

[103] A. Hands, P. Morris, K. Ryden, C. Dyer, P. Truscott, A. Chugg, and S. Parker, “Single event effects in power mosfets due to atmospheric and thermal neutrons,” *IEEE Transactions on Nuclear Science*, vol. 58, no. 6, pp. 2687–2694, 2011.

[104] P. A. Butler, M. J. Uren, B. Lambert, and M. Kuball, “Neutron irradiation impact on algan/gan hemt switching transients,” *IEEE Transactions on Nuclear Science*, vol. 65, no. 12, pp. 2862–2869, 2018.

[105] M. Ahmed, B. Kucukgok, A. Yanguas-Gil, J. Hryn, and S. Wender, “Neutron radiation hardness testing of 650v/7.5 a gan power hemt,” *Radiation Physics and Chemistry*, vol. 166, p. 108456, 2020.

[106] D. Ball, B. Sierawski, K. Galloway, R. Johnson, M. Alles, A. Sternberg, A. Witulski, R. Reed, R. Schrimpf, A. Javanainen *et al.*, “Estimating terrestrial neutron-induced seb cross sections and fit rates for high-voltage sic power mosfets,” *IEEE Transactions on Nuclear Science*, vol. 66, no. 1, pp. 337–343, 2018.

[107] F. Berthet, S. Petitdidier, Y. Guhel, J. L. Trolet, P. Mary, C. Gaquière, and B. Boudart, “Influence of neutron irradiation on electron traps existing in gan-based transistors,” *IEEE Transactions on Nuclear Science*, vol. 63, no. 3, pp. 1918–1926, 2016.

[108] N. Islam, M. F. P. Mohamed, M. F. A. J. Khan, S. Falina, H. Kawarada, and M. Syamsul, “Reliability, applications and challenges of gan hemt technology for modern power devices: A review,” *Crystals*, vol. 12, no. 11, p. 1581, 2022.

[109] C. A. Klein, “Bandgap dependence and related features of radiation ionization energies in semiconductors,” *Journal of Applied Physics*, vol. 39, no. 4, pp. 2029–2038, 1968.

[110] M. Zerarka, P. Austin, A. Bensoussan, F. Morancho, and A. Durier, "Tcad simulation of the single event effects in normally-off gan transistors after heavy ion radiation," *IEEE Transactions on Nuclear Science*, vol. 64, no. 8, pp. 2242–2249, 2017.

[111] A. Luu, F. Miller, P. Poirot, R. Gaillard, N. Buard, T. Carriere, P. Austin, M. Bafleur, and G. Sarrabayrouse, "Seb characterization of commercial power mosfets with backside laser and heavy ions of different ranges," *IEEE Transactions on Nuclear Science*, vol. 55, no. 4, pp. 2166–2173, 2008.

[112] G. Johnson, J. Palau, C. Dachs, K. Galloway, and R. Schrimpf, "A review of the techniques used for modeling single-event effects in power mosfets," *IEEE Transactions on Nuclear Science*, vol. 43, no. 2, pp. 546–560, 1996.

[113] S. Liu, R. Marec, P. Sherman, J. L. Titus, F. Bezerra, V. Ferlet-Cavois, M. Marin, N. Sukhaseum, F. Widmer, M. Muschitiello *et al.*, "Evaluation on protective single event burnout test method for power dmosfets," *IEEE Transactions on Nuclear Science*, vol. 59, no. 4, pp. 1125–1129, 2012.

[114] J. H. Hohl and K. F. Galloway, "Analytical model for single event burnout of power mosfets," *IEEE Transactions on Nuclear Science*, vol. 34, no. 6, pp. 1275–1280, 1987.

[115] M. Allenspach, C. Dachs, G. Johnson, R. Schrimpf, E. Lorfevre, J. Palau, J. Brews, K. Galloway, J. Titus, and C. Wheatley, "Segr and seb in n-channel power mosfets," *IEEE Transactions on Nuclear Science*, vol. 43, no. 6, pp. 2927–2931, 1996.

[116] D. Kobayashi, "Scaling trends of digital single-event effects: A survey of seu and set parameters and comparison with transistor performance," *IEEE Transactions on Nuclear Science*, vol. 68, no. 2, pp. 124–148, 2020.

[117] T. T. Mnatsakanov, M. E. Levinshtein, L. I. Pomortseva, S. N. Yurkov, G. S. Simin, and M. A. Khan, "Carrier mobility model for gan," *Solid-State Electronics*, vol. 47, no. 1, pp. 111–115, 2003.

[118] S. Tiwari, *Compound semiconductor device physics.* Academic press, 2013.

[119] D. J. Roulston, N. D. Arora, and S. G. Chamberlain, "Modeling and measurement of minority-carrier lifetime versus doping in diffused layers of n+-p silicon diodes," *IEEE Transactions on Electron Devices*, vol. 29, no. 2, pp. 284–291, 1982.

[120] A. Rockett, *The materials science of semiconductors.* Springer Science & Business Media, 2007.

[121] B. H. Bransden and C. J. Joachain, "Introduction to quantum mechanics," 1989.

[122] G. Sabui, P. J. Parbrook, M. Arredondo-Arechavala, and Z. Shen, "Modeling and simulation of bulk gallium nitride power semiconductor devices," *AIP Advances*, vol. 6, no. 5, p. 055006, 2016.

[123] J. A. McPherson, P. J. Kowal, G. K. Pandey, T. P. Chow, W. Ji, and A. A. Woodworth, "Heavy ion transport modeling for single-event burnout in sic-based power devices," *IEEE Transactions on Nuclear Science*, vol. 66, no. 1, pp. 474–481, 2018.

[124] J. P. Spratt, E. A. Burke, J. C. Pickel, and R. E. Leadon, "Modeling high-energy heavy-ion damage in silicon," *IEEE Transactions on Nuclear Science*, vol. 48, no. 6, pp. 2136–2139, 2001.

[125] M. Raine, G. Hubert, P. Paillet, M. Gaillardin, and A. Bournel, "Implementing realistic heavy ion tracks in a see prediction tool: Comparison between different approaches," in *2011 12th European Conference on Radiation and Its Effects on Components and Systems*. IEEE, 2011, pp. 363–370.

[126] J. Zoutendyk, H. Schwartz, and L. Nevill, "Lateral charge transport from heavy-ion tracks in integrated circuit chips," *IEEE Transactions on Nuclear Science*, vol. 35, no. 6, pp. 1644–1647, 1988.

[127] J. Barak and A. Akkerman, "Straggling and extreme cases in the energy deposition by ions in submicron silicon volumes," *IEEE transactions on nuclear science*, vol. 52, no. 6, pp. 2175–2181, 2005.

[128] D. K. Schroder, *Semiconductor material and device characterization.* John Wiley & Sons, 2015.

[129] J. H. Stathis, "Percolation models for gate oxide breakdown," *Journal of applied physics*, vol. 86, no. 10, pp. 5757–5766, 1999.